Semiconductor Fiber Laser

Design and Applications of a Tunable Multi-wavelength SFL

Véronique Pagé

Department of Electrical and Computer Engineering
McGill University Montréal, Québec, Canada
January 2006

A thesis submitted to the Faculty of Graduate Studies and Research in partial fulfillment of the requirements of the degree of Master of Engineering

Your file Votre référence
ISBN: 978-0-494-25003-7
Our file Notre référence
ISBN: 978-0-494-25003-7

Abstract

Multi-wavelength laser sources have attracted much interest in the last decade as new photonic technologies have enabled the realization of such sources with much improved characteristics. Tunable continuous-wave multi-wavelength fiber lasers may now offer, for example, the ability to tune the wavelength spacing between the lasing lines and, also at times, the possibility to control the individual output peak powers. The more flexible and low-cost solutions benefiting from higher optical spectrum bandwidths also attract the most interest for future applications. These lasers find clients in so many fields such as optical test and measurement, optical communications, sensing, and processing like microwave photonic filtering. The search for such a flexible, stable and affordable laser source has fueled the investigation presented in this thesis. We first analyze the different approaches taken in the past for the implementation of tunable continuous-wave multi-wavelength lasers and follow with the development of a novel, relatively low-cost, tunable multi-wavelength semiconductor fiber laser (SFL). All the design steps are clearly explained and characterized. The final SFL is then used for the demonstration of two applications: chromatic dispersion measurements in long fiber spools, and the new design of a photonic microwave filter.

Sommaire

Les lasers à multiples longueurs d'onde ont fait l'objet de plusieurs recherches au cours des dernières années. Les nouvelles avancées en matière de composants photoniques ont permis une grande amélioration de ce type de laser. Ces lasers permettent maintenant de contrôler, par exemple, l'espacement entre les longueurs d'onde des différents modes du laser, et parfois même, de varier individuellement la puissance de chaque ligne. Les solutions les moins coûteuses et les plus polyvalentes, permettant le plus grand nombre de modes, suscitent le plus d'intérêt pour des applications futures. En effet, ces lasers multilongueur d'onde, continus et accordables, peuvent être employés autant dans le domaine des communications optiques que dans l'élaboration de capteurs optiques polyvalents et de filtre passe-bande à hyperfréquence. Ceux-ci sont aussi très utiles afin de compléter des tests et mesures optiques. La quête pour ce type de laser multifonctionnel stable et peu coûteux a donc été l'élément déclencheur de tout le travail présenté dans cette thèse. Nous analysons en premier lieu les différentes approches proposées par le passé afin de mieux élaborer par la suite un nouveau laser multilongueur d'onde à fibre semiconducteur continu et accordable. Toutes les étapes nécessaires au développement du laser y sont clairement expliquées et expérimentées. Le laser final est ensuite utilisé pour deux applications: la mesure de la dispersion chromatique accumulée dans de longues distances de fibres optiques et le développement d'un filtre photonique à hyperfréquence.

Acknowledgements

First and foremost, I would like to thank Prof. Lawrence R. Chen for his constant encouragements, help and inspiring cues which have given me the keys towards the realization of this thesis. Special thanks to Prof. Marin as well, who always believed in me, and to Prof. Kirk for his inspiring undergraduate teaching.

Un grand merci à tous ceux qui m'ont aidée, supportée ou côtoyée, de proche ou de loin, tout au long de mes études et de ma vie. A ma famille, et tout particulièrement à mes parents et à ma grand-mère; vous m'avez permis de réaliser l'un de mes plus grands rêves d'enfance, celui de pouvoir accéder au monde du savoir, celui d'être toujours aussi épanouie devant tant de beauté qu'est cet univers, et de pouvoir enfin comprendre un peu plus les mystères de la vie. Vos encouragements et votre amour inconditionnel ont toujours été pour moi source de confiance, d'ambition et de persévérance. Aux grands rêves, les grands efforts et compromis. Cela dit, mes années passées à l'université m'ont vraiment prouvé que ce qui ne nous anéantit pas nous rend bien plus fort. Puisse la vie nous permettre de continuer d'évoluer vers de nouveaux horizons, toujours aussi excitants et remplis de défis.

Many thanks to the entire Computer and Electrical Engineering department, and to all the members of the Photonics Research Group. Additional thanks to several undergraduate students for their help with some Labview programs. Merci aussi à Julien pour son soutien technique, et à Nicolas pour son aide et ses « initiations » aux différents instruments de laboratoire.

Thank you to all my friends: Lidija, Polo, Christina, to you also, Reuven; things would have never been the same without your "Cheers" at the end of the day! And to Alan as well, who has given me my engineer ring and who has persuaded me to continue my studies! Et enfin, un dernier merci à Johann pour nos longues discussions variées et divertissantes!

The research work presented in this thesis has been supported by an NSERC-eMPOWR scholarship and by Anritsu Electronics, Ltd.

Table of Contents

List of Figures

List of Tables

I. Introduction

The recent interest for developing efficient, yet economical CW multi-wavelength sources (MWS) is due to their incredible potential in applications such as fiber optic sensing, optical communications, passive and active component characterization, WDM systems, and photonic microwave filtering. They replace the use of an equivalent number of discrete or tunable laser sources, each possibly independently controlled in terms of wavelength and power, to reduce the cost, size and complexity of the final application. For example, MWS are ideal in the characterization of optical amplifiers where the gain profiles must be entirely saturated, or for polarization-mode dispersion, chromatic dispersion and polarization-dependent measurements usually carried out with a single or multiple tunable sources [1.1]. Many applications thus benefit from a relatively large number of lasing wavelengths or modes and sometimes require the ability to tune the wavelength spacing as well as the individual peak powers. Also, the more versatile the source is, the more adaptable to any kind of situation.

1.1 Motivation

Many different MWS implementations have been proposed and each offer their own advantages and disadvantages. Generally speaking, practicality, reliability and precision are of capital importance. This means both stability in terms of peak powers and emission wavelengths, but also simplicity in terms of implementation or design. Finally, as these sources are usually intended to be commercially available, a lowest-cost solution is preferred.

Past implementations explored both incoherent spectrum sliced broadband sources, such as light emitting diodes (LEDs) and amplified spontaneous emissions (ASE), as well as coherent Raman lasers, Erbium-doped fiber (EDF) lasers, and semiconductor fiber lasers (SFL). EDF amplifiers are appealing since they are low cost, but their limitations in terms of multi-wavelength lasing when used as a gain medium in a fiber laser for example, can become a problem [1.2]. Many articles report the difficulties encountered with the homogeneous broadening of the EDF gain medium which inhibits or renders more difficult multi-wavelength lasing [1.3-1.5]. Raman and semiconductor

optical amplifiers (SOA), on the other hand, are interesting gain mediums due to their larger bandwidths, and also because they are not constrained to emitting in either C- or L-bands [1.2, 1.6]. Semiconductor amplifiers have the advantage of being not only more compact in size, but may be directly modulated, and like Raman amplifiers, their inhomogeneous broadened gain spectrum permits many wavelengths to emit simultaneously inside a laser cavity at room temperature [1.2-1.5] Unfortunately, SOAs are a little more prone to power fluctuations. This is why the use of linear optical amplifiers (LOAs) for dynamic WDM systems has been proposed and may lead the way to future developments [1.3].

Whether a coherent laser or an incoherent source implementation is chosen, a way to obtain the multiple wavelength peaks is needed. Broadband sources may be spectrum sliced using a variety of techniques, while gain mediums such as amplifiers placed inside a fiber ring configuration, for example, may coherently laze at multiple wavelengths if a multi-wavelength comb filter is inserted inside the ring cavity. A wild variety of spectrum slicing methods and comb filters have previously been proposed, all of which work similarly, based on either fiber Fabry-Perot filters [1.1, 1.3, 1.5, 1.7], Michelson [1.8] and delayed interferometers [1.4], arrayed waveguide gratings [1.12, 1.13], fiber Bragg gratings (FBG) [1.11-1.14], and high Birefringence fiber loop mirrors (HiBi-FLM) [1.2, 1.15]. Whatever method chosen, the resulting source must provide for high contrasts and output powers, a flat or nicely apodized emission spectrum if desired, be as insensitive as possible to environmental perturbations [1.16], and offer the most number of peak wavelengths in order for the MWS to be of interest for future applications.

Several techniques have also been proposed to dynamically change the output spectrum of the source. This includes the change of the individual wavelengths or their corresponding powers, together with the ability to uniformly control the wavelength separation between the peaks. Tunability can be made continuous or discrete, but a uniform, equispaced change in wavelength spacing is a desirable asset, as well as low complexity and ease of use. For interferometer-based filtering, for example, a means of varying the induced phase shift in one arm can change the phase difference, and hence vary the wavelength spacing of the generated comb filter [1.4]. As such, each filtering implementation may be made tunable in some way. Generally, the more tunable the

source is, the more interesting the technique becomes for future applications that require different sets of output spectra.

1.2 Thesis Outline

This research thesis first explores what has been achieved in the recent past regarding tunable multi-wavelength continuous-wave sources, both coherent and incoherent, proposes the design of coherent fiber ring laser using a semiconductor optical amplifier, experimentally verifies its operation, and demonstrates its reliability and flexibility under two different applications. Chapter 2 first gives a comprehensive review of the fundamentals, past and recent progress, and current state of the art of tunable CW multi-wavelength sources. Chapter 3 introduces the prototype design of the experimentally developed tunable multi-wavelength semiconductor fiber laser (SFL), with step by step implementation changes made throughout the development stage. Each laser setup is then evaluated and the final design is chosen in terms of the desired requirements. The demonstration of the two applications is then carried out using the proposed tunable multi-wavelength SFL: chapter 4 experimentally investigates time-of-flight chromatic dispersion measurements in long fiber spools, and chapter 5 presents a new implementation of a tunable photonic microwave filter.

The novel contributions made in this thesis include:

- The use of a new tunable CW multi-wavelength SFL for time-of-flight chromatic dispersion measurements in long fiber spools. This work was presented at Photonics North 2005 conference in Toronto, September 12-14, 2005. For publication, refer to Appendix C: V. Pagé, L.R. Chen, "Chromatic dispersion measurements of optical fiber based on time-of-flight using a tunable multi-wavelength semiconductor fiber laser," *Photonic applications in devices and communication systems, Proc. of SPIE,* vol.5970, *79501X,* 2005.

- The new design of a tunable and reconfigurable photonic microwave filter using a tunable CW multi-wavelength SFL and fiber delay lines. For publication, refer to Appendix C: V. Pagé, L.R. Chen, "Tunable photonic microwave filter using a semiconductor fiber laser" *IEE Electronics Letters*, vol. 41, no.21, October 13, 2005.

1.3 References

1.1 N. Pleros, C. Bintjas, M. Kalyvas, G. Theophilopoulos, K. Yiannopoulos, S. Sygletos, and H. Avramopoulos. "Multiwavelength and power equalized SOA laser sources," *IEEE Photonics Technology Letters*, vol. 14, no.5, pp. 693-695, May 2002.

1.2 L. R. Chen. "Tunable multiwavelength fiber ring lasers using a programmable high-birefringence fiber loop mirror," *IEEE Photonics Technology Letters*, vol. 16, no.2, pp. 410-412, February 2004.

1.3 K. K. Qureshi, H.Y.Tam, W.H. Chung, and P.K.A. Wai. "Multiwavelength laser source using linear Optical Amplifier," *IEEE Photonics Technology Letters*, vol. 17, no. 8, pp. 1611-1613, August 2005.

1.4 H.Dong, G.Zhu, Q.Wang, H. Sun, N.K.Dutta, J. Jaques, and A.B. Piccirilli. "Multiwavelength fiber ring laser source based on a delayed interferometer," *IEEE Photonics Technology Letters*, vol. 17, no.2, pp. 303-305, February 2005.

1.5 H. Chen. "Multiwavelength fiber ring lasing by use of a semiconductor optical amplifier," *Optics Letters*, vol. 30, no. 6, pp. 619-621, March 15, 2005.

1.6 G.Keiser, *Optical Fiber Communications*, 3rd Edition. Boston: McGraw-Hill (2000)

1.7 J. Capmany, D. Pastor and B. Ortega. "Fibre optic microwave and millimeter-wave filter with high density sampling and very high sidelobe suppression using subnanometre optical spectrum slicing," *Electronic Letters*, vol. 35, no. 6, pp. 494-496, March 1999.

1.8 A.P. Foord, P.A. Greenhalgh. "Synthesis of microwave and millimeter-wave filters using optical spectrum-slicing," *Electronics Letters*, vol. 32, No. 4, pp. 390-391, February 1996.

1.9 J. Capmany, J. Mora, B.Ortega and D. Pastor. "Microwave photonic filters using low-cost sources featuring tunability, reconfigurability and negative coefficients," *Optics Express*, vol.13, no.5, pp. 1412-1414, March 2005.

1.10 P.M. Lane and K. Kitayama. "Optical generation of mm-waves using spectrum-sliced ASE for low-cost WDM based fibre radio systems," *Electronics Letters*, vol. 34, no. 10, pp. 1010-1011, May 1998.

1.11 M. Delgado-Pinar, J.Mora, A. Diaz, and M.V.Andres. "Tunable and reconfigurable microwave filter by use of a Bragg-grating-based acoustico-optic superlattice modulator," *Optics Letters*, vol.30, no.1, pp. 8-10, January 2005.

1.12 J. Mora, B. Ortega, J.L. Cruz, J. Capmàny, D. Pastor, M.V. Andres. "White light sources filtered with fiber Bragg gratins for RF-photonics applications," *Optics Communications*, vol. 8878, pp. 1-5, May 2003.

1.13 J. Mora, M.V. Andres J. Cruz, B. Ortega, J. Capmany, D. Pastor, S. Sales. "Automatic tunable and reconfigurable fiber-optic microwave filters based

on a broadband optical source sliced by uniform fiber Bragg gratings," pp. 1291-1298, July 2003.

1.14 D. Pastor, J. Capmany, B. Ortega. "Broadband tunable microwave transversal notch filter based on tunable uniform fiber Bragg gratings as slicing filters," *IEEE Photonics Technology Letters,* vol. 13, no.7, pp. 726-728, July 2001.

1.15 Y. Shiquan, L. Zhaohui, D. Xiaoyi, Y. Shuzhong, K. Guiyun, and Z. Qida. "Generation of wavelength-switched optical pulse from a fiber ring laser with F-P semiconductor modulator and a HiBi fiber loop mirror," *IEEE Photonics Technology Letters*, vol. 14, no.6, pp. 774-776, June 2002.

1.16 R.Ramaswani and K.N.Sivarajan, *Optical Networks: A Practical Perspective*. San Fransisco: Morgan Kayfmann Publishers, Inc. (1998), Chapter 3.

Other Readings:

- B-A. Yu, J. Kwon, S. Chung, S-W. Seo and B. Lee. "Multiwavelength-switchable SOA-fibre ring laser sampled Hi-Bi fibre grating," *Elecronics Letters*, vol. 39, no.8, pp. 649-650, April 2003.
- V. Polo, F. Ramos, J. Marti, D. Moodie, and D. Wake. "Synthesis of photonic microwave filters based on external optical modulators and wide-band chirped fiber gratings," *Journal of Lightwave Technology*, vol. 18, no.2, pp. pp. 213-120, February 2000.
- J. Marti, V. Polo, F. Ramos, and D. Moodie. "Photonic tunable microwave filters employing electroabsorption modulators and wideband chirped fibre gratings," Electronics *Letters*, Vol. 35, no. 4, pp. 305-306, February 1999.
- J. Marti, F. Ramos and R.I. Laming. "Photonics microwave filter employing multimode optical sources and wideband chirped fibre gratings," *Electronic Letters*, vol.34, no. 18, pp. 1760-1761, September 1998.

II. Tunable Multi-wavelength Sources

2.1 Multi-wavelength Sources

Great progress has been made within the last decade concerning the development of MWS. Their applications have also gained much from the possibility of using one single source instead of multiple, individually controlled, single-mode sources. They are now less complex, and thus less costly and more prone to being commercially exploitable. They are even often more reliable, as the limit imposed on the number of modes starts to disappear. This is the case, for example, with photonic microwave filtering and time-of-flight chromatic dispersion measurements; the two applications being demonstrated in this thesis. Any other application involving optical test and measurement, sensing, and WDM communications also greatly benefit from the new advances performed in the world of multi-wavelength sources.

As such, the control over wavelength spacing between each mode, or of the peak powers emitted by the source is a feature that attracts even more interest. The ability to tune the output spectrum of the source would, for example, permit tunability and reconfiguration of photonic microwave filters, and offer double precision in test and measurement applications; two different input source settings giving two distinct sets of output data for the same component under test.

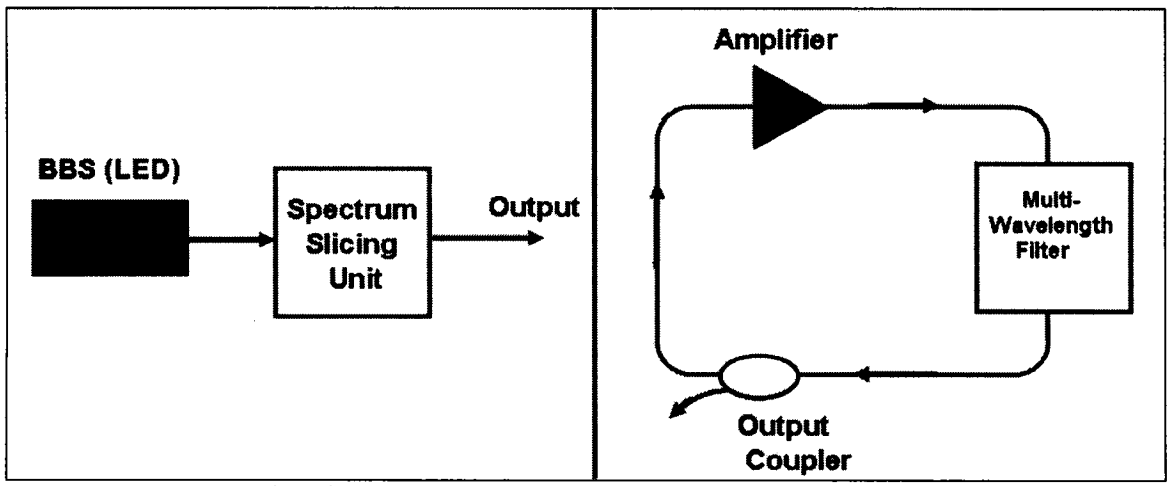

Figure 2- 1: General implementation of multi-wavelength sources (fiber ring lasers to the right, or a spectrum sliced broadband LED source to the left).

Many types of MWSs have been demonstrated, each offering their own advantages and limitations, as later detailed in the next subsection. Figure 2-1 shows two different families of MWS configurations. A BBS may be spectrally sliced to generate incoherent wavelength peaks, or coherent lasing can be obtained from a laser configuration such as the one shown, where an amplifier or gain medium with a comb filtering device ensures multi-wavelength lasing through the cavity feedback mechanism. The possibility to tune the spectrum slicing device or the comb filter characteristics offers, in turn, the ability to vary the peak wavelengths, wavelength spacing, and sometimes the individual peak powers.

Other means of creating multi-wavelength lasers are also possible, such as using several independent single-mode lasers. For example, distributed feedback lasers (DFBs) and distributed Fabry-Pertor fiber lasers (DFPs) have been readily demonstrated in the past. These offer advantages such as very narrow linewidths and even single longitudinal and polarization mode operation in the case of DFPs [2.1-2]. Figure 2-2 shows a five wavelength DFB fiber laser implementation. The laser is essentially based on five independent cascaded DFB lasers built from a uniform Bragg grating photoinduced on a length of erbium doped fiber, and pumped with a single semiconductor diode. The lasing wavelengths are spaced by approximately 1nm, and each lasing DFB offers a tuning range of about 5nm using a stress-induced center wavelength shift. The splicing between each laser may not be fully optimized, however, and this may lead to larger variations in lasing peak powers. The ASE of each piece of erbium doped fiber may also decrease the signal to noise ratio [2.1]. An improved but similar configuration makes use of spatially DFPs instead, where each laser is made of two superimposed chirped fiber Bragg gratings [2.2]. In this manner, the peak powers generated from each laser cavity are coupled by pump depletion, cross-gain saturation and Brag grating structure mechanisms. The spectrum flatness here is limited by the grating uniformity and possible thermal effects. Large spectrums are also difficult to achieve, since increasing the grating chirps require higher photo-induction, while a higher chirp may also lead to more important overlaps between consecutive laser cavities; an issue for small channel spacings. The authors consequently suggest achieving greater bandwidth by increasing the erbium fiber length of each device; although this may increase ASE and cause further pump depletion. In

other words, this implementation has interesting advantages, but also represents greater design complexity and higher costs.

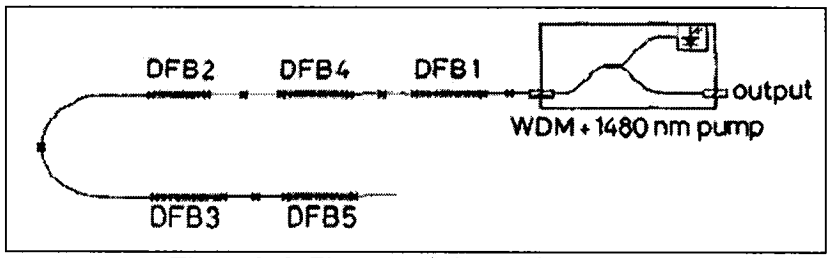

Figure 2- 2: Five cascaded DFBs lasers [2.1].

The following sections give a deeper review of the past implementations making use of the two families of configurations shown in figure 2-1, and elaborate on the possible BBS and spectrum slicing techniques, as well as on the various gain media and comb filters available, while investigating the different methods to provide for wavelength tunability.

2.1.1 Broadband Sources and Gain Media

For incoherent MWS based on the spectrum slicing of BBS, the choice of the specific type of source, ASE of amplifiers or LEDs, does not have a major impact. The BBS only needs to provide enough power and a relatively flat spectrum over a large enough bandwidth and desired wavelength range such that the source's output spectrum offers the desired characteristics.

In the case of coherent fiber ring laser configurations, however, the choice of the type of gain medium may alter the final laser characteristics. The past ten years has mainly seen the development of multi-wavelength fiber ring lasers using either EDF amplifiers (EDFA) or SOAs, as they are readily available and low-cost.

All optical amplifiers increase the power level of incident light within their operating wavelength range through a stimulated emission process. The device absorbs energy supplied from an external source called a pump, which in turns raises the electrons inside the active medium to higher energy levels to produce a population inversion. An incoming photon or carrier can then make the excited electrons drop to lower energy levels, thereby producing an amplified signal.

EDFAs are today's most widely used amplifiers. They are created by lightly doping usually ten to thirty meters of silica fiber core with Erbium ions. They generally operate within the 1530-1630nm range, or the C-band, with optical pumping at 1480nm or 980nm [2.3]. A pump signal with a wavelength shorter than the input signal is necessary to raise the dopant electrons to excited states higher than the desired lasing level. Once this is achieved, input signal photons trigger the electrons into stimulated emission, thereby releasing the remaining energy in the form of a new photon with a wavelength, phase and polarization identical to that of the signal photon. From the energy level characteristics of erbium ions, however, pumping the ions to excited states can generate stimulated as well as spontaneous emission, giving rise to added amplifier noise, or ASE, as long as excited electrons are available. The ASE may thus be used as a BBS in spectrally sliced configurations. For fiber amplifier laser designs, their advantages include low coupling losses with fibers in the laser cavity for example, low polarization dependency and low sensitivity to input signal format (or modulation rates) since their gain dynamics are slow; their carrier lifetimes are in the order of 0.1-10ms. The gain response thus remains constant for modulation rates higher than a few kilohertz, making them also immune to any kind of interference or crosstalk effects [2.3]. Fiber lasers implemented using EDFAs can however produce only a limited number of lasing wavelengths, since their homogeneous linewidth is approximated to several nanometers at room temperature [2.4]; generally around ten nanometers. This explains why simultaneous lasing modes closer than 1nm are quite impossible to achieve with EDF lasers at room temperature. The large homogeneous linewidth of EDFA's gives a much broadened Lorentzian lineshape, such that the output energy is more largely spread amongst all the possible frequencies present within the amplifier bandwidth. In this case, complex techniques such as cooling the fiber at 77K by immersion in liquid nitrogen, using specially designed twin-core Er^{3+} doped fiber [2.5] or frequency-shifted feedback, becomes necessary to reduce the linewdith of the amplifier and thus permit stable multi-wavelength emissions [2.6].

SOAs, on the other hand, offer stable multi-wavelength emission at room temperature, and over a larger bandwidth not constrained to either C- or L-bands [2.6]. In comparison, the homogeneous broadening linewidth of an SOA was deduced to be

around 0.6nm at 1550nm wavelength at room temperature, much smaller than EDFA's at the same temperature. This fact indicates that SOA-based multi-wavelength oscillations with WDM ITU standard wavelength spacing is possible [2.4], and thus makes SOAs very interesting candidates. Unlike EDFAs, the stimulated emission is created from carrier recombination in the active gain junction layer, and occurs only when a current flows through the active region of the device. Hence, it is a planar device which may be directly modulated using the bias current. Figure 2-3 shows a schematic of an SOA, the relationship between the gain and the output power, with the refractive index profile and carrier flow within the amplifier. Refer to this figure for the equations and definitions given below.

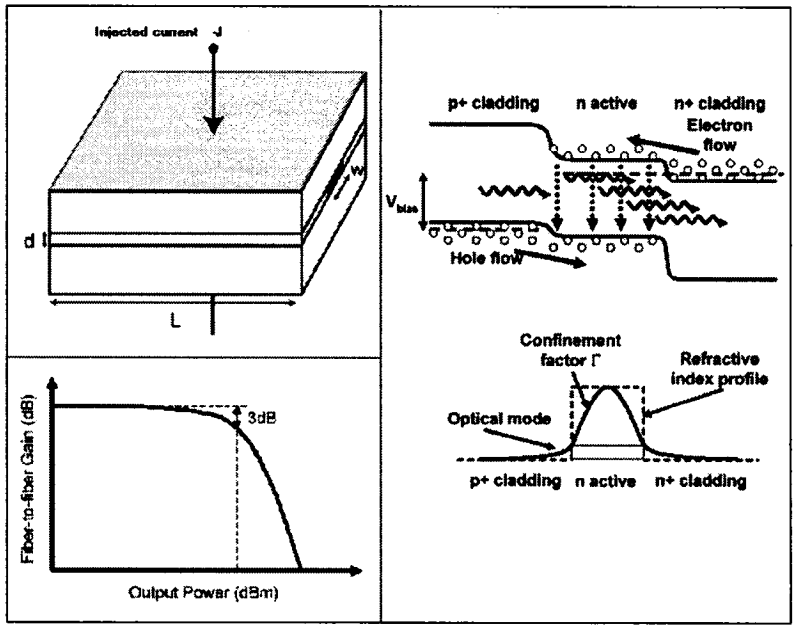

Figure 2- 3: Top left: Schematic of an SOA; bottom left: relationship between Pout and Gain (Pout/Pin); right side: schematic of amplification process, and refractive index profile of amplifier.

Most SOAs used in optical communications are non-resonant traveling-wave amplifiers (TWA) as they provide larger bandwidths, higher saturation powers, and lower polarization sensitivity. TWA have their end facets either antireflection-coated or cleaved at an angle since the input light gets amplified only once.

Similarly to laser diodes, the sum of the injection current, stimulated emission and spontaneous recombination rates gives the rate equation modeling the carrier density n(t) in the excited state:

$$\delta n(t)/\delta t = J(t)/qd - R_{st}(t) - n(t)/\tau_r \qquad (1)$$

where $R_{st}(t) = \Gamma a v_g(n-n_{th})N_{ph}$ (2)

is the net stimulated emission rate, and

$$N_{ph} = P_s/(v_g(h\nu)(wd)) \quad (3)$$

is the photon density.

J(t) is the injection bias current density, d is the thickness of the active region, w is the active region width, τ_r is the combined time constant coming from spontaneous emission and carrier-recombination mechanisms. v_g is the group velocity of the incident light, $h\nu$ is the photon energy, Γ is the optical confinement factor of the active region, a is the gain constant, n_{th} is the threshold carrier density, and P_s is the input optical signal power.

Rearranging all the equations, one can define small-signal gain per unit length as:

$$g_0 = \Gamma a \tau_r(J/qd-n_{th}/\tau_r) \quad (4)$$

Then, amplifier gain, defined as the ratio of the output signal power to the input signal power, follows the relation:

$$G = \exp[(g(z)L] \quad (5)$$

where L is the amplifier length, and g(z) is the overall gain per unit length, which can be defined as:

$$g(z) = g_0/(1+ P_s(z)/P_{ampsat}) \quad (6)$$

where $P_s(z)$ is the internal signal power at point z, and P_{ampsat} is the amplifier saturation power, defined as the power level at which the gain power per unit length is half its highest value. Note that if the gain is z-dependent, then the amplifier gain is written as:

$$G = \exp[\int g(z)dz] \quad (7)$$

The above equations tell us that gain increases with active region length, but is limited by gain saturation. This is because as the input signal level is increased, excited carriers are depleted from the active region, and further increases in the input level will thus no longer give any change in output levels since there are not enough excited carriers left to provide the required amount of stimulated emission [2.3].

Their principle of operation being established, it is worthwhile to note that SOAs may easily be integrated with other components on monolithic substrates. They also

consume less power and are more compact. However, their quicker gain responses (in the order of 1ps-0.1ns) may cause the gain at a specific wavelength to fluctuate with signal rate for high bit rates, and thus affect the overall gain. The gain at other wavelengths will fluctuate as well since they depend on the overall gain. In other words, such rapid gain responses may cause crosstalk effects when a large number of wavelength modes are amplified simultaneously, such as in a multi-wavelength fiber ring laser configuration [2.3]. Intra-laser cavity light reflections may also occur and give rise to further power fluctuations or noise. That being said, linear optical amplifiers (LOAs), typically described as an SOA with a vertical-cavity surface emitting laser integrated perpendicularly along the entire length of the amplifier, permit yet even more stable multi-wavelength lasing, as previously reported [2.5]. The design difference in a LOA, as compared to a regular SOA, helps to provide a constant gain to the amplifier and thus reduces gain competition inside the laser cavity. Finally, SOAs are also slightly more sensitive to polarization than EDFAs. Overall, their ability to emit simultaneous wavelengths in laser configurations, under room temperature conditions, represents their main advantage over EDFAs, as their minor imperfections may be controlled or accounted for.

2.1.2 Multi-Wavelength Filtering Techniques

Once a broadband source or a gain medium is chosen, a method for isolating the desired peaks must be developed. Either using spectrum slicing of comb filtering within a fiber laser cavity, past and recent multi-wavelength filtering techniques involve the use of fiber Bragg gratings (FBG), interferometers such as fiber Fabry-Perot filters (FPF) or thin film etalons filters, Michelson, Mach-Zehnder (MZI) or delayed interferometers (DI), array waveguide gratings (AWG), and Sagnac loops. Every method has its own specific advantages and limitations, and is sometimes more flexible than others. It is important, however, that the filter have periodic passbands over the widest possible bandwidth within the 1530-1570nm region, with high extinction ratios (> 30dB). The full width half maximum should at least be about half the spacing between passbands. Each technique is first fully described, and specific spectrum sliced sources and laser implementation

examples are given afterwards, together with some alternative ways of controlling wavelength spacing and weighing of the peaks.

Fiber Bragg Gratings:

FBGs are very commonly used nowadays in WDM systems, as they permit the isolation and processing of chosen wavelength carriers. The technology is so advanced that these can be made with extremely low insertion losses on the order of 0.1dB. They are very accurate and provide for high crosstalk suppression and flat passband tops. They are also specially packaged to be less temperature-dependant. The periodic refractive index perturbation along the length of the propagation medium induces the reflection of a narrow spectral band of frequencies centered on the Bragg wavelength of the grating, which satisfies the following equation:

$$\lambda_B=2n_{eff}\Lambda \qquad (8)$$

where n_{eff} is the effective index of the propagating mode and Λ is the grating period. The refractive index modulation n(z) may also be apodized to suppress the sidelobes of the main passband [2.9].

Another approach is to use sampled FBGs (SFBGs). These are gratings with a super-imposed refractive index amplitude and phase modulation within their fiber core. The reflected wavelengths will thus be equally distributed around the Bragg wavelength, and spaced by a fixed amount satisfying the following equation:

$$\Delta\lambda =\lambda_B^2/2n_{eff}p \qquad (9)$$

where p is the sampling period [2.4].

Finally, if only uniform gratings are utilized, inducing a periodic strain perturbation can in turn modulate the period and the refractive index of the FBG, thus obtaining specific wavelength spacings. This method is called a Bragg-grating-based acoustico-optic superlattice modulation (AOSLM). Essentially, a longitudinal acoustic wave of frequency f_s is sent along a FBG, thereby changing its properties and creating spectrally equispaced bands of reflection on both sides of the FBG's Bragg wavelength, as an SFBG would produce. The difference here is that the induced change is reversible

and may be tailored to provide for the desired wavelength spacing according to the following equation:

$$\Delta\lambda = \lambda_B^2 f_s / 2n v_s \quad (10)$$

where n is the average modal index and v_s is the acoustic-wave phase velocity. Mora et al. demonstrated AOSLM in 2005 [2.8]. The limitations are related to the transducer, tapered adapter, and other auxiliary components that are necessary to provide for the frequency f_s of the acoustic wave. The non-linear relation between the acoustic-wave frequency and the tunability mechanism diminishes the ease of use and reliability.

Fiber Bragg Gratings implementation examples:

FBG's may be used to create either coherent lasing or incoherent multi-wavelength sources. The principle of operation typically remains the same.

For example, in 2001, Pastor and al. proposed an incoherent broadband source spectrally sliced with two uniform fiber Bragg gratings [2.9]. The source is fed to a 3dB coupler, where both exiting arms connect to two different FBGS. Two different wavelengths are thus reflected and combined at the output port of the coupler. The wavelength spacing could be tuned by imposing a strain on only one of the gratings: 2, 1.5, 1, and 0.5nm spacings were thus realized. The irregularities in reflection coefficients of the uniform FBGs were not a problem for a wavelength spacing made large enough compared with the grating bandwidths. This slicing technique nevertheless imposed a lower limit on the wavelength spacing. In 2002, Mora, Pastor et al. continued their work and developed yet another improved alternative [2.10]. This time, the broadband source was fed to a circulator, where the second port led to a series of gratings. The gratings were also stretched to tune their reflection bandwidths initially centered at λ_{init}. As a brief description, and referring to figure 2-4, when the grating is stretched by ΔL over a fiber length L_N, the λ_{init} of the grating N shifts by:

$$\Delta\lambda_N = \lambda_{initN}(1-p_e)\,\Delta L / L_N \quad (11)$$

where p_e is the photoelastic coefficient of the optical fiber. The beauty of the design is that any stretching will keep Bragg wavelengths of all gratings spectrally

equispaced, an important feature for many applications such as the one they intended to develop: a microwave filter with high noise rejection levels.

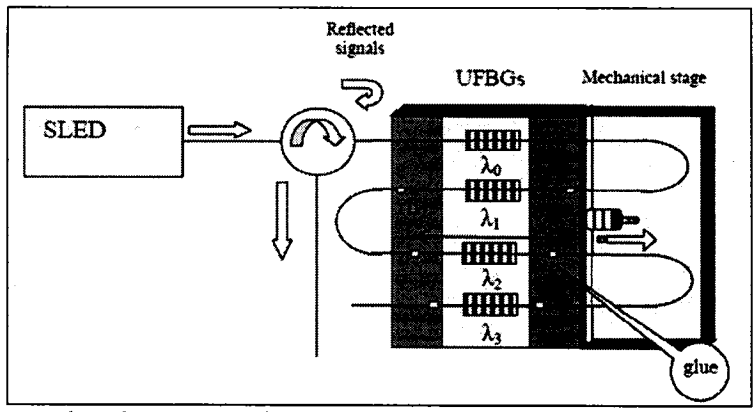

Figure 2- 4: Multi-wavelength source employing FBG spectrum slicing technique developed by Mora et al. in 2002 for Microwave photonic filtering purposes [2.10].

A similar configuration using the gratings in parallel, as opposed to being in series as shown, is also proposed by the authors as a means for tunable tap of peak power weighing, or peaks [2.10]. In this case, the broadband source must enter a NxN coupler, where the N exiting ports are attached to variable attenuators, followed by an FBG. All the FBGS are mounted on the same strain table, and thus also provide for a uniform tuning of the wavelength spacing. The peak weighing is performed via variable attenuators. As the researchers point out, this implementation is somewhat limited both in the number of peaks generated and the wavelength spacing, as the FBGs can only be stretched until the fiber breakdown limit.

The above technique can also be used for the implementation of coherent lasers as well, as suggested by Yao et al. in 2002. This research group proposed an erbium-doped fiber ring laser in which a similar FBG stage is incorporated using couplers, and the tuning is also performed via tensile or compressive grating strain [2.11]. Another interesting example using sampled FBGs this time was proposed in 2003, where a sampled HiBi fiber grating, or a super-periodic grating with a HiBi fiber core, was employed to create a switchable multi-wavelength source [2.4]. In this way, only unpolarized waves in two wavebands, each centered at their Bragg wavelength and separated by a fixed amount, are reflected. The polarization of each reflected waveband can be aligned along the fast or the slow axis of the HiBi fiber. Thus, two different reflection responses can be used and the laser thus offers the possibility to change the

lasing wavelengths by a small amount determined by the birefringence of the fiber core. The wavelength spacing of each state could however only be varied via a change in the grating period induced by some kind of strain as previously shown by Pastor et al.

Fabry-Perot and Thin Film Etalon Filters:

Fabry-Perot interferometers are formed by enclosing a cavity within two highly reflective mirrors (Fabry-Perot filters—FPFs), or by multiple reflective dielectric thin film layers (thin film etalon filters), both placed parallel to each other such that the light may reflect back and forth inside the cavity. Each facet partly passes and partly reflects the light. If the wavelength of the light entering the cavity is an integral multiple of half the length of the cavity, all the light waves are transmitted through the end facet and add in phase. Those resonant wavelengths create the periodic transfer function of the filter [2.7].

These types of mutli-wavelength filters offer the advantages of generating subnanometer wavelength spacings, and thus more wavelength transmission peaks, but may only offer a very limited wavelength spacing tunability via angle and temperature controls.

Fabry-Perot and Thin Film Etalon Filter implementation examples:

FPF have been used in the past for both spectrum slicing and lasing configurations. For example, Capmany and al. [2.12] have used such a filter to spectrally slice 34 peak wavelengths from a BBS. This same technique may also be employed towards multi-wavelength lasing, as later demonstrated by Pleros and al. [2.13]. More recently, in 2005, Chen demonstrated a multi-wavelength fiber ring laser using an SOA and a 50GHz spacing FPF [2.14]. In 2005 as well, Qureshi et al. [2.5] also employed a thin film etalon filter with a LOA in a similar fiber ring laser configuration. These three laser examples did not offer tunability, however.

Michelson, Mach-Zehnder (MZI) and Delayed Interferometers (DI):

The basic principle behind an interferometer is, as its name implies, the interference between waves that have different phases. The Michelson interferometer is one of the oldest versions. It is formed by a 3dB coupler and a pair of lens and mirror combination, one pair placed at each end of the two exit ports of the coupler. Once split into two waves, the input light propagates in the two arms. If the path length of one arm is made different than the other, once the waves are reflected back and recombined at the coupler, they will either interfere constructively of de-constructively, providing for the periodic filter response with respect to wavelength [2.7].

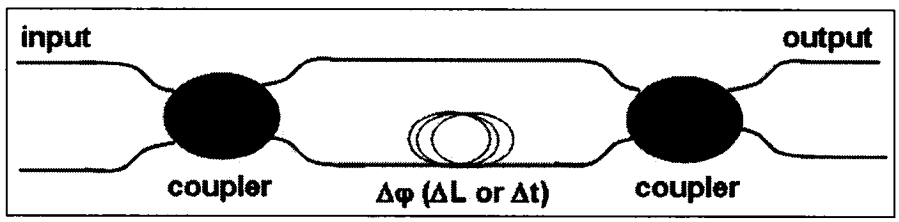

Figure 2- 5: MZI example.

A MZI is a simple extension of the above principle, where instead of using mirrors to reflect the light back into the input coupler, a second coupler is used, as shown in figure 2-5. In this case, the phase difference is induced by one arm having a path length difference, and may be tuned by changing the arms refractive index via a temperature variation for example. MZI hence suffer from being very sensitive to environmental changes and are thus mostly left for sensing purposes. Narrow passbands can also usually only be obtained by cascading many MZIs, thereby generating high insertion losses, not to mention that these may suffer from increased crosstalk with aging [2.7]. Recent Si-SiO_2 waveguide technology advancements have, however, rendered MZI more reliable by carefully packaging them with temperature controllers [2.15].

Specially packaged, and thus less prone to environmental perturbations, DIs function in the same way as MZIs. The time delay between both interferometer arms induces a phase difference. The output intensity is thus a periodic function with respect to wavelength and the wavelength spacing is directly related to the time delay by:

$$\Delta\lambda = \lambda_o^2/c\tau \qquad (12)$$

where λ_o is 1550nm, c is the speed of light in vacuum and τ is the time delay [2.15]. This multi-wavelength filtering technique is only limited by the time delay that is realizable using the available technology, but once the DI is created, it may not be altered and wavelength spacing may not be varied.

Michelson and Delayed Interferometers (DI) implementation examples:

The use of Michelson interferometers may be also used for either spectrum slicing of a BBS or comb filtering in a laser configuration.

For example, a Michelson interferometer setup was proposed in 1996 for the implementation of an incoherent spectrum sliced source towards the synthesis of a microwave filter [2.16]. The wavelength spacing could be tuned by mounting one mirror on a micropositionner and thus vary the path length of one arm. This free-space technique produces filters with low finesse and is not very practical in nature since undesired free-space reflections and problems with keeping the mirrors in-line can arise.

As mentioned, this type of filter could also be employed towards multi-wavelength lasing if inserted directly inside the ring laser cavity itself. As such, a novel all-fiber version of a Michelson interferometer, a Michelson-Gires-Tournois Structure, was recently developed and could represent another alternative to multi-wavelength filtering [2.17]. The all-fiber multipassband filter was realized for both 100 and 50GHz channel spacings. The solution is thus fully compatible to fiber systems, presents low insertion losses, and is also relatively low-cost. The model essentially makes use of a chirped FBG in one arm of the interferometer, and a distributed Gires-Tournoise etalon (DGTE) in the other, to obtain a path length difference. While this type of filter presents higher isolation and the advantage of flattop passbands with better square-like shapes, its tunability is limited, and its low stability and higher dispersion characteristics must be improved upon.

Finally, one example of a DI used for the implementation of a multi-wavelength fiber laser was proposed by Dong et al. in 2005 [2.15].

Arrayed Waveguide Gratings:

AWGs are a generalization of the MZI in the sense that the same principle of path difference interference occurs. Two multiport couplers are interconnected by an array of waveguides. Figure 2-6 shows a 1xN AWG as an example.

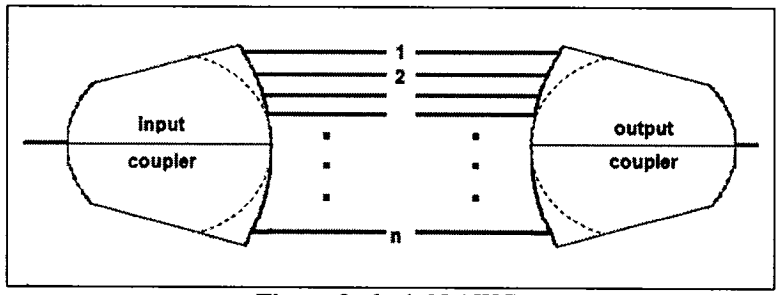

Figure 2- 6: 1xN AWG.

For one input signal, many copies of the same source are shifted in phase by different amounts and are added together at the output coupler. A 1xN/Nx1 AWG will thus only transmit the wavelengths satisfying the following relation:

$$n_1\delta_i^{in} + n_2\Delta L + n_1\delta_j^{out} = p\lambda_j \quad \text{for any integer p} \qquad (13)$$

where δ_i^{in} and δ_j^{out} are the relative phase changes at each 1xN and Nx1 couplers (proportional to the distances traveled inside the respective input or output couplers), n_1 is the refractive index of the couplers and n_2 is the refractive index of the arrayed waveguides. This relation indicates a periodic nature with respect to wavelength [2.7].

AWGs were originally designed for dense WDM multiplexing and demuliplexing applications. They are easy to realize in integrated-optic substrates and have lower loss than chained MZIs. They sometimes require some sort of temperature control but they may generate wavelength spacings as small as 0.8nm, the WDM ITU standard. As such, AWGs with 50 or 25GHz spacings are readily available nowadays on the market.

Arrayed Waveguide Gratings implementation examples:

Similarly to al the previous filtering approaches, arrayed waveguide gratings may also be used for both spectrum slicing and multi-wavelength fiber laser configurations.

One incoherent spectrum slicing example dates back to 1998, where a broadband EDFA ASE was fed to an AWG for the realization of a photonic filter [2.18]. AWGs

offer much flexibility and have recently generated much interest. In 2003, Capmany et al. proposed a way to generate a tunable multiwavelength incoherent source with 1x40 AWGs where switches and variable attenuators were inserted between both input and output AWGs. This is a reliable method of controlling wavelength spacing—by turning the switches off or on—and peak powers via individual variable attenuators. The tuning is restricted to the number of channels (multiples of 0.8nm) and the wavelength position cannot be changed easily however. The number of switches and attenuators follows the number of desired output wavelengths, and the implementation can thus become quite complex and expensive [2.19].

This filtering technique is undoubtedly very precise and could also be employed to implement coherent multi-wavelength lasers. Takahashi et al. [2.20] had indeed already proposed such a technique in 1994. In this case, an erbium-doped fiber ring laser simultaneously emited four wavelengths with stable spacing through the use of an intra-cavity arrayed waveguide N x N wavelength multiplexer, as shown in figure 2-7. Four different half rings with each an EDFA were connected through the AWG to a common half ring. Only wavelengths 5, 7, 9 and 11 survive, and the wavelength spacing is double the multiplexer channel spacing. A bandpass filter must however be inserted in the ring cavity as well, if the FSR of the AWG is smaller than the gain medium bandwidth, in order to eliminate the extra multiple-pass, or the higher order of the AWG's wavelengths occurring for each fiber loop. The disadvantages of this method include the fact that several individual EDFAs are required for each lasing mode, and the wavelength spacing between each mode cannot be easily varied.

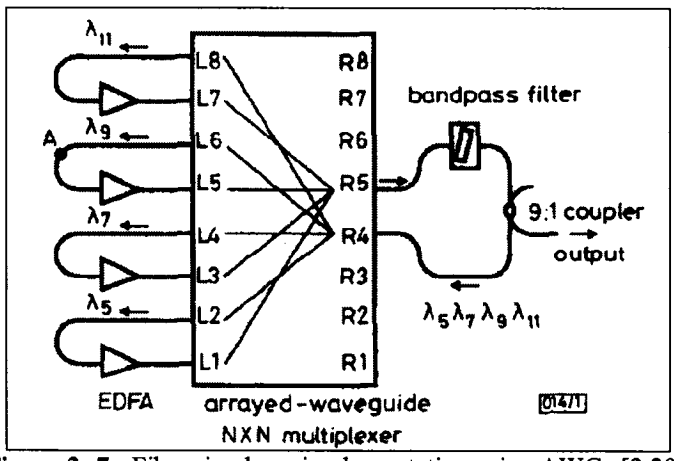

Figure 2- 7: Fiber ring laser implementation using AWGs [2.20].

Sagnac Loops:

A final comb filter implementation approach which has recently generated much investigation is the Sagnac loop. The principle of operation is similar to any kind of interferometer. The insertion of either a fiber grating or a length of HiBi polarization maintaining (PM) fiber inside a fiber loop has been previously demonstrated [2.6, 2.21-24]. Fiber loop mirror mechanisms are fully explained in Appendix A.

To generate a periodic transmission or reflection response, such loops may employ, for example, an asymmetrically-located uniform fiber Bragg grating inside the loop [2.22]. In this manner, the length difference between both fiber lengths that are separated by the grating inside the loop generates a filter with a sinusoidal response, and the reflection spectrum of the grating experiences multiple passbands. A way to change the position of the grating inside the loop may in turn vary the wavelength spacing of the filter passbands. This is, however, not an easy task, although this type of filter design is low cost and simple.

The other approach of incorporating a length of HiBi PM fiber inside the loop could provide for an easier way to implement filter tunability. In these HiBi fiber loop mirrors (HiBi-FLMs), the amount of birefringence in the loop will vary the phase difference between the counter-propagating waves inside the loop mirror according to the relation:

$$\Delta\varphi(\lambda) = 2\pi BL/\lambda \qquad (14)$$

where B is the amount of birefringence and L is the length of HiBi fiber [2.6, 2.23].

The transmission and reflection intensity profiles will in turn be a periodic function of wavelength. Tunability can be obtained by changing the length of HiBi fiber itself. The state of polarization between the two counter-propagating waves will also influence the overall characteristics. Please note that HiBi-FLMs are further discussed in section 3.2.

Sagnac Loop implementation examples:

Sagnac loops have generally been mostly used for the development of coherent laser configurations. These provide for simple, low cost and tunable solutions. Several past implementations have been proposed. The following gives a few examples.

In 2002, Shiquan et al. used such a filter to create a wavelength-switched optical pulse from a fiber ring laser [2.21]. They provided a limited wavelength spacing tunability by making use of piezoelectric ceramics that slightly adjusted the HiBi fiber length in the FLM. In 2004, Shu et al. proposed a way to shift the comb-like transmission response of the HiBi-FLM by using an optical control signal and an SOA inside the filter's fiber loop, as shown in figure 2-8 [2.23]. This technique does not alter the wavelength spacing, however, as this is mainly governed by the amount of HiBi fiber in the loop. The added SOA birefringence, which is determined by the amount of bias current sent to the amplifier, the sate of polarization of the control light and the increase in control beam power, translates into an added phase difference in the interferometer, thereby wavelength shifting the overall transmission filter characteristics. The shifting behavior reaches a saturation level, however, because of the induced electrical carrier depletion in the SOA at large control powers.

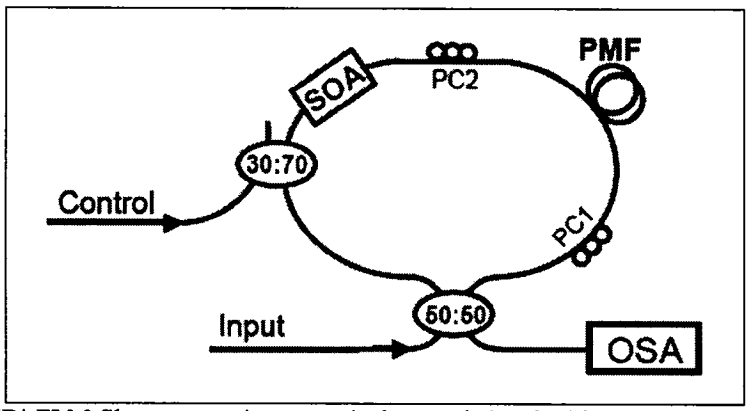

Figure 2- 8: HiBi-FLM filter setup using an optical control signal with an integrated SOA to shift the comb-like transmission characteristics of the filter [2.23].

This filter wavelength shift can also be done by simply using an electro-optic phase modulator inside the FLM of the filter, as demonstrated by Shu et al. in 2005 [2.24]. The applied dc bias, RF power and modulation frequency will control the extent of the shift.

A better way to provide for filter passband spacing tunability was proposed by Chen in 2004, where 2x2 switches were inserted inside the FLM to add or subtract a fixed length of HiBi fiber at each switch stage, as shown in figure 2-9. The digital tunability is much more reliable in this manner and is only restricted to the amount of 2x2-HiBi fiber blocks. Polarization controllers placed inside the FLM adjusted the contrast of the filter response [2.6].

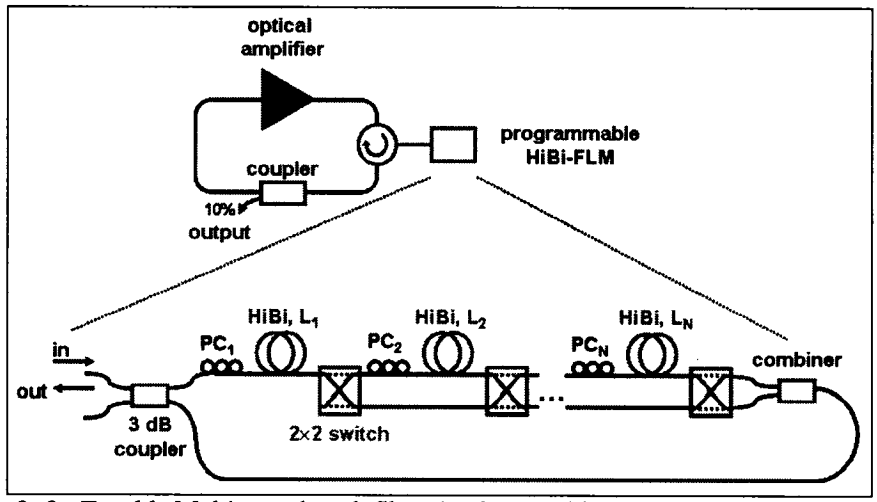

Figure 2- 9: Tunable Multi-wavelength fiber ring lasers with programmable HiBi-FLM [2.6].

Table 2-1 now summarizes all the possible multi-wavelength emission approaches, either employing multiple lasers such as DFBs, BBSs, or amplifier gain mediums, as well as the available filtering techniques necessary for BBS and amplifier implementations; all of which were discussed in the above sections. Their respective advantages and disadvantages are given, and one may readily conclude that more investigation could be undertaken using multi-wavelength semiconductor fiber lasers with one of the above filtering techniques.

After comparing all the possible MWSs offered in the past, a closer look at the past and recent work concerning only the development of CW multi-wavelength SOA-based fiber lasers (SFL) will provide for a deeper understanding of such laser configurations.

Implementations:	Advantages	Disadvantages	References
Source/amplifier: **Multiple DFB and DFP lasers (coherent)**	Narrow linewidths: single-longitudinal and polarization mode operation possible	Complexity increases with bandwidth and smaller wavelength spacing	2.1-2
Spectrally sliced BBSs (incoherent)	Any choice of source possible.	Need a flat spectrum source, larger linewidths.	2.10, 2.19
EDFAs with multi-wavelength filter (coherent)	Inexpensive, immune to cross-talk and interference, polarization insensitive.	Difficult to produce stable, closely spaced multi-wavelength emission at room temperature.	2.3, 2.11, 2.20
SOAs with multi-wavelength filter (coherent)	Inexpensive, permits stable multi-wavelength lasing at room temperature, larger bandwidth. Easily integrated, compact planar device, consumes less power than EDFA.	Polarization sensitive, gain competition between modes may create instabilities. Limited in output powers.	2.3-4, 2.6, 2.13-15, 2.24
Multi-wavelength Filtering using: **FBGs**	Isolation of chosen wavelengths, low insertion loss, accurate, high extinction ratios, flat passband tops	Irregularities in FBG reflection coefficients, limited tunability prone to reliability and complexity issues.	2.4, 2.7-11
FPFs	Subnanometer wavelength spacing, very precise, large bandwidths.	Very limited tunability via angle or temperature control. More expensive realization.	2.5, 2.7, 2.12-14
MZIs	Narrow passbands realizable with many cascaded MZIs (larger insertion losses and increased crosstalk with aging however)	More sensitive, unless specially packaged (expensive), limited tunability.	2.7, 2.15-17
AWGs	Easily integrated, low insertion loss, subnanometer spacings, precise.	Usually requires temperature control, (more expensive).	2.7, 2.18-20
Sagnac Loops	Easily tunable via birefringence, simple, thus less expensive.	More polarization-sensitive.	2.6, 2.21-24

Table 2- 1: A summary of MWSs: the possible implementations with their advantages and disadvantages.

2.2 Multi-wavelength Semiconductor Fiber Lasers

Multi-wavelength SFLs have recently attracted a considerable amount of interest since, as previously mentioned, SOAs permit stable multiple wavelength lasing at room temperature.

In 2002, Pleros et al. showed that multi-wavelength power equalized SOA laser sources with an extended bandwidth of 52 lines spaced at 50GHz was achievable. Their fiber ring laser used a FPF and two SOAs within the cavity. A single-pass optical feedback loop broadened the spectrum from 38 to 52 wavelength lines [2.13]. It is also reported that the use of a second SOA in the ring can further increase the bandwidth if this second amplifier has a peak gain spectrum slightly offset. Thus, according to the article, optimizing cavity loss, and adjusting the drive currents of the two SOA's can result in a wide uniform multi-wavelength spectrum.

More recently, in 2004, Chen demonstrated multi-wavelength lasing using one SOA with a HiBi-FLM as a comb filter inside a fiber ring [2.6]. This laser was previously shown in figure 2-8 of section 2.1. It is digitally tunable by using 2x2 switches inside the filter. Optimizing the polarization controllers and the SOA bias current is also said to reduce the peak power excursion between the lasing wavelengths at the expense of oscillation bandwidth.

More research has also been recently generated, in 2005. In February, a new design employing a DI with a variable attenuator showed a stable 75-wavelength oscillation spaced at 40GHz with a very good extinction ratio of 40dB [2.15]. In March of this same year, Chen demonstrated 50 simultaneous wavelength lasing oscillations at 1.3μm, spaced at 50GHz, with a 30dB signal to noise ratio (SNR) [2.14]. He employed a FPF as a filtering method, as shown in figure 2-10. In August 2005, a similar configuration employing a thin film etalon filter this time was also investigated in terms of lasing stability. It is reported that LOAs may be of increased interest since they are much more stable than SOAs [2.5]. All these past implementations included a directional isolator to ensure one-way light propagation in the fiber ring, a set of polarization controllers (PCs), and sometimes, the use of a variable optical attenuator (VOA) was needed as well inside the fiber loop to control intra-cavity losses.

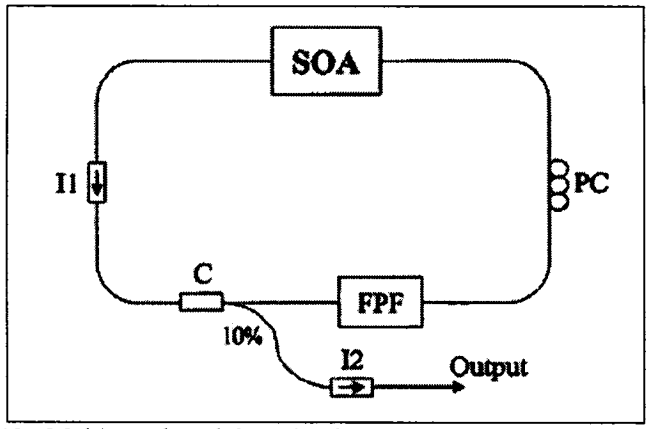

Figure 2- 10: Multiwavelength laser implementation proposed by H.Chen [2.14].

Another SOA fiber ring laser setup was proposed by Shu et al. in July 2005 [2.24]. This time, the multi-wavelength filter consisted of a phase modulator (PM) loop mirror, or a Sagnac loop with a phase modulator, as shown in figure 2-11. The overall waveband created by the laser could be switched by controlling either the applied PM's dc bias, and RF modulation power or frequency. The polarization controllers inside the loop are first adjusted to optimize the comb filter position and peak to notch contrast ratio of the transmission spectra. Once theses are kept fixed, it is seen that the filter is relatively insensitive to input light polarization and its insertion loss is calculated to be around 5.5dB. With a bias current of 190mA sent to the SOA, the overall laser output spectra emits 21 lines spaced out by 0.8nm, from 1570 to 1587nm, with a SNR above 40dB. Figure 2-9 demonstrates the various switched wavebands obtained from such a laser configuration. The switching itself does not vary much the 3dB bandwidth of the laser spectra, and the peak linewidths were calculated to be around 0.07nm. Stability measures indicate 1.5dB power variation over one hour. The Sagnac loop can also be used in reflection mode with the addition of a circulator, which gives different kinds of wavelength peaks as well. This method is quite interesting, but the wavelength spacing itself may not be varied. Phase modulators are also still quite expensive elements, although future improvements might reduce the costs of such devices.

One can make a few conclusions from all the previous work done on semiconductor based multi-wavelength fiber ring lasers. First, it is known that the ripple and the polarization-dependent gain of the SOA will affect the spectrum flatness and bandwidth. The state of polarization of the light in the laser cavity must be carefully

adjusted via intra-cavity PCs in order to obtain the flattest possible laser spectrum, with optimized SNR [2.5, 2.14-15]. Previous experimentations also demonstrated that increasing the SOA bias current usually increases the width of the laser spectrum, and shifts the center wavelength upwards (to longer wavelengths) [2.14]. The cavity loss may however be controlled with a VOA, and can shift the emitting multi-wavelength comb as well [2.5, 2.14]. When the cavity loss is increased, the gain of the amplifier is also increased, and the carrier density of the SOA thus increases as well. The center of the waveband will thus shift toward shorter wavelength since the photon energy at which the maximum gain occurs also shifts to a higher energy with increasing carrier density. The right combination of bias current(s), polarization state, and intra-cavity losses, is thus the key to obtaining the best output spectrum possible, with the most number of peaks, the least peak excursion and the largest SNR.

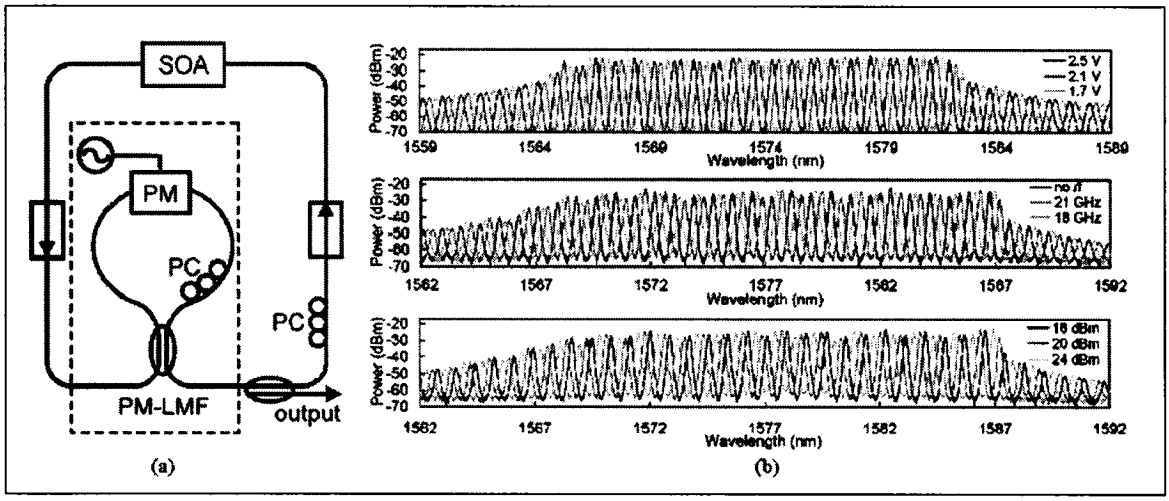

Figure 2- 11: Waveband-switchable SOA-based fiber ring laser with a phase modulator lop mirror filter proposed by C.Shu et al. in July 2005. Graph to the right (from top to bottom): laser spectra obtained with (1) different dc biases, (2) RF modulation frequencies at 24dBm RF power, and (3) RF powers at 26GHz modulation frequency [2.24].

2.3 Conclusion

After considering all the examples provided in the above sections, it is readily understood that SOAs have the advantage of permitting stable multi-wavelength emissions at room temperature, unlike EDFAs, and could thus be an interesting solution towards designing a low-cost, simple, tunable CW multi-wavelength fiber laser. The use of a filter device that is easily tunable and simple, like some kind of Sagnac loop could also represent an advantageous alternative. The only issues with the use of an SOA as a gain medium inside a fiber laser are the low output powers and the possible polarization sensitivities. Both depend on the exact components, and the filter insertion loss. The future applications may permit lower output powers, but these may always be increased using a second amplifier if necessary. Finally, the polarization sensitivity of SOAs may actually be of some and permit a flatter lasing spectrum, as was the case in past implementations.

2.3 References

2.1 J.Hubner, P.Varning and M.Kristensen. "Five wavelength DFB fibre laser source for WDM systems," *Electronics Letters*, vol. 33, no.2, pp. 139-140, January 16th, 1997.

2.2 G.Brochu, S. Larochelle, R.Slavik. "Modeling and experimental demonstration of ultracompact multiwavelength distributed Fabry-Perot fiber lasers," *J. of Lightwave Technology*, vol.23, no.1, pp. 44-53, January 2005.

2.3 G. Keiser, *Optical Fiber Communications*, 3rd Edition. Boston: McGraw-Hill (2000)

2.4 B-A. Yu, J. kwon, S. Chung, S-W. Seo and B. Lee. "Multiwavelength-switchable SOA-fibre ring laser sampled Hi-Bi fibre grating," *Electronics Letters*, vol. 39, no.8, pp. 649-650, April 17th, 2003.

2.5 K. K. Qureshi, H.Y.Tam, W.H. Chung, and P. K. A. Wai. "Multiwavelength laser source using linear optical amplifier," *IEEE Photonics Technology Letters*, vol. 17, no. 8, pp. 1611-1613, August 2005.

2.6 L. R. Chen. "Tunable multiwavelength fiber ring lasers using a programmable high-birefringence fiber loop mirror," *IEEE Photonics Technology Letters*, vol. 16, no.2, pp. 410-412, February 2004.

2.7 R. Ramaswani and K. N. Sivarajan, *Optical Networks: A Practical Perspective*. San Fransisco: Morgan Kayfmann Publishers, Inc. (1998), Chapter 3.

2.8 M. Delgado-Pinar, J. Mora, A. Diaz, and M.V.Andres. "Tunable and reconfigurable microwave filter by use of a Bragg-grating-based acoustico-optic superlattice modulator," *Optics Letters*, vol.30, no.1, pp. 8-10, January 2005.

2.9 D. Pastor, J. Capmany, B. Ortega. "Broadband tunable microwave transversal notch filter based on tunable uniform fiber Bragg gratings as slicing filters," *IEEE Photonics Technology Letters*, vol. 13, no.7, pp. 726-728, July 2001.

2.10 J. Mora, B. Ortega, J. Capmany, J.L. Cruz, M.V. Andres, D. Pastor, S. Sales. "Automatic tunable and reconfigurable fiber-optic microwave filters based on a broadband optical source sliced by uniform fiber Bragg gratings," *Optic Express*, vol.10, no.22, pp. 1291-1298, November 2002.

2.11 J. Yang, J. Yao, K. Zhou, Y. Liu, "Wideband wavelength tunable fiber ring laser with flattened output power spectrum," *Optics Communications*, vol. 210, no.3-6, pp. 313-318, September 15 2002.

2.12 J. Capmany, D. Pastor, B. Ortega. "Fibre optic microwave and millimeter-wave filter with high density sampling and very high sidelobe suppression using subnanomter optical spectrum slicing," *Electronics Letters*, vol.35, no.6, pp. 494-496, March 1999.

2.13 N. Pleros, C. Bintjas, M. Kalyvas, G. Theophilopoulos, K. Yiannopoulos, S. Sygletos, and H. Avramopoulos. "Multiwavelength and power equalized

SOA laser sources," *IEEE Photonics Technology Letters*, vol. 14, no.5, pp. 693-695, May 2002.

2.14 H. Chen. "Multiwavelength fiber ring lasing by use of a semiconductor optical amplifier," *Optics Letters*, vol. 30, no. 6, pp. 619-621, March 15, 2005.

2.15 H. Dong, G. Zhu, Q. Wang, H. Sun, N.K. Dutta, J. Jaques, and A.B. Piccirilli. "Multiwavelength fiber ring laser source based on a delayed interferometer," *IEEE Photonics Technology Letters*, vol. 17, no.2, pp. 303-305, February 2005.

2.16 A.P. Foord, P. Davies and P.A. Greenhalgh. "Synthesis of microwave and millimeter wave filters using optical spectrum-slicing," *Electronics Letters*, vol.32, no.4, pp. 390-391, February 1996.

2.17 X. Shu, K. Sugden, I. Bennion, "Novel Multipassband optical filter using all-fiber Michelson-Gires-Tournois Structure," *IEEE Photonics Technology Letters*, vol. 17, no. 2, pp. 384-386, February 2005.

2.18 P.M. Lane and K. Kitiyama. "Optical generation of mm-waves using spectrum-sliced ASE for low-cost WD based fibre radio systems," *Electronic Letter*s, vol. 34, no.10, pp. 1010-1011, May 1998.

2.19 D. Pastor, B. Ortega, J. Capmany, S. Sales, A. Martinez and P. Munoz. "Optical microwave filter based on spectral slicing by use of arrayed waveguide gratings," *Optics Letters*, vol.28, no. 19, pp. 1802-1804, October 2003.

2.20 H.Takahashi, H.Toba, Y.Inoue, "Multiwavelength ring laser composed of EDFAs and arrayed-waveguide wavelength multiplexer," *Electronics Letters*, vol. 30, no.1, pp. 44-45, January 1994.

2.21 Y. Shiquan, L. Zhaohui, D. Xiaoyi, Y. Shuzhong, K. Guiyun, and Z. Qida. "Generation of wavelength-switched optical pulse from a fiber ring laser with F-P semiconductor modulator and a HiBi fiber loop mirror," *IEEE Photonics Technology Letters*, vol. 14, no.6, pp. 774-776, June 2002.

2.22 X. Shu, S. Jiang, D. Huang. "Fiber grating Sagnac loop and its multiwavelength-laser application," *IEEE Photonics Technology Letters*, vol.12, no.8, pp. 980-981, August 2000.

2.23 K.L. Lee, M.P. Fok, S.M. Wan, C. Shu, "Optically controlled Sagnac loop comb filter," *Optics Express*, vol.12, no.25, pp. 6335-6337, December 2004.

2.24 C. Shu, K.L. Lee, M.P. Fok, "Waveband-switchable SOA ring laser constructed with a phase modulator loop mirror filter," *IEEE Photonics technology Letters*, vol.17, no.7, pp. 1393-1395, July 2005.

III. Tunable Multi-wavelength SFL Design and Characteristics

From the review of all the different approaches that have been previously proposed for developing a tunable CW multi-wavelength laser source, it was concluded that semiconductor optical amplifiers offer many advantages over other existing gain mediums, and thus semiconductor fiber ring laser prototype designs are of interest. A suitable tunable multi-wavelength filtering technique is necessary, however, and the laser design must meet several requirements in order to be reliable for its applications later demonstrated in chapters 4 and 5.

Table 3-1 summarizes the essential attributes of the final laser design. The laser should be stable over time in terms of lasing wavelengths and peak powers. Good filter characteristics should allow for the smallest possible maximum peak excursion as spectrum flatness is usually desirable in many applications. The signal-to-noise ratio of the laser (SNR) must be acceptable; greater than 30dB is preferable. The number of peaks must be as high as possible, keeping in mind that the wavelength spacing must usually be within 1-4nm in order to be able to measure chromatic dispersion in long fiber spools using the time-of-flight technique, as proposed in chapter 4. The linewidth of each lasing peak must also be small enough (under 0.3nm at least) so as not to impose a big limitation on the amount of chromatic dispersion that will be measurable with the time-of-flight technique proposed. Finally, the ability to tune the wavelength spacing of the laser is desired for both future applications. In this way, the design of a tunable photonic microwave filter will be made possible in chapter 5, and the chromatic dispersion measurement tool will thus offer the capability of performing two dispersion measurements with one single source, thereby increasing its overall precision and flexibility.

The next section 3.1 presents the prototype laser design, while section 3.2 makes full characterization of the multi-wavelength filter and wavelength tunability technique employed. Once this is accomplished, section 3.3 presents the experimental performances of the different laser implementations and compares them in terms of the desired requirements. The final laser design is then fully characterized in section 3.4.

	Minimum Laser Requirements
Peak powers (dBm)	Highest possible, at least -25dBm for each peak
SNR (dB)	> 30dB
Maximum peak power excursion (dB)	Around 3dB if possible, no greater than 6dB
Wavelength spacing	1 to 4nm, possibly tunable
Bandwidth (nm)	> 16nm (within the 1540-1570nm range)
Number of peaks	> 5 peaks, depending on the wavelength spacing
Peak linewidths (nm)	< 0.3nm

Table 3- 1: Summary of minimum laser requirements

3.1 Prototype Design

A general schematic of the multi-wavelength laser to be characterized and improved upon is presented in figure 3-1. The sections surrounded by a dotted square are components that will either be kept or removed after experimental investigation. The two different arrows emerging from the High Birefringence fiber loop mirror (HiBi-FLM) indicate that the filter will either be used in transmission or in reflection mode, the latter requiring the use of a circulator.

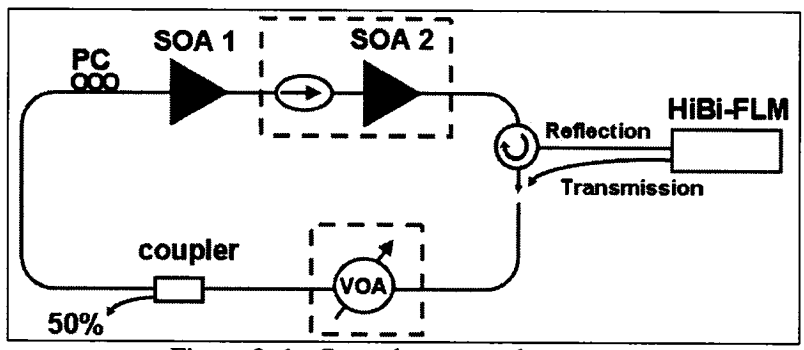

Figure 3- 1: General prototype laser setup.

The gain is provided by either one or two SOAs. Later design characterizations will determine whether or not the second SOA is necessary. When two SOAs are used, however, an isolator is inserted between them to ensure unidirectional propagation inside the second SOA. The lasing wavelengths are selected by the comb filter, or HiBi-FLM, (see Figure 3-2) connected to the laser cavity by a circulator that also ensures

unidirectional propagation. Two 2x2 switches inside the filter itself provide for laser tunability by offering two possible wavelength spacings. In the case where the filter is employed in transmission mode, only two ports of the circulator are used for isolation purposes. A variable optical attenuator is also included in the cavity for later use in possible power weighing of the lasing modes, gain flatness and center wavelength control. The use of this component is also questionable. The polarization controllers are necessary to optimize the laser's output spectrum. Finally, a 3dB output coupler is employed in order to have more output power, as the relatively low intra-cavity loss of the SFL did not require more feedback power. Collecting 90% and returning only 10% power into the loop was found, however, to be too small to create any feedback. The cavity loss is the summation of the variable attenuation, the loss of the circulator or isolator, and the insertion loss of the HiBi-FLM. Once the filter losses are experimentally determined in section 3.2.2, the total cavity loss can be found.

The two SOAs employed in the experimental setup of the laser are both Alcatel 1901 MSA compatible 1550nm WDM products. SOA 1 (ASWD020078) has a peak small-signal gain of 20.14dB for input signal power of –25.8dBm and current of 200mA at 1550nm. Saturation output power is 10.2 dBm and polarization sensitivity is 0.4 dB. SOA 2 (ASWD020077) has a peak small-signal gain of 18.58dB for input signal power of –25.79dBm and current of 200mA at 1550nm. Saturation output power is 10.7dBm and polarization sensitivity is 0.3 dB. SOA 1 is placed first in order to exploit its greater polarization dependence using the polarization controllers placed in front.

3.2 HiBi-FLM

The multi-wavelength filter design must allow for the most number of lasing lines with as much peak power as possible. Hence, its insertion loss must be minimized, and its comb filter characteristic should be as constant as possible over the relevant wavelength range; that is between 1530 and 1580nm at least. High contrasts, or signal to noise ratio, are necessary to provide for good peak isolation, as well as narrow linewidths. Wavelength spacing should be small, uniform and should be made tunable for increased flexibility.

3.2.1 Operation

A schematic of the HiBi-FLM filter design used in the prototype laser is presented in figure 3-2. The operation of the HiBi-FLM is briefly described as follows (refer to Appendix A for theory on fiber loop mirrors). The 3dB coupler in the HiBi-FLM splits the input signal in two counter-propagating waves. These travel through the loop and are then recombined by the same coupler. The interference of the waves will either be constructive or destructive, depending on the birefringence of the loop. In this way, the FLM's reflection and transmission spectra will be a periodic function of wavelength. Since both waves travel through the same optical path, the filter will be less sensitive to environmental changes. But as previous work indicates, such a filter is a little more prone to fluctuations when more birefringence is present in the fiber loop, and wavelength spacing is reduced.

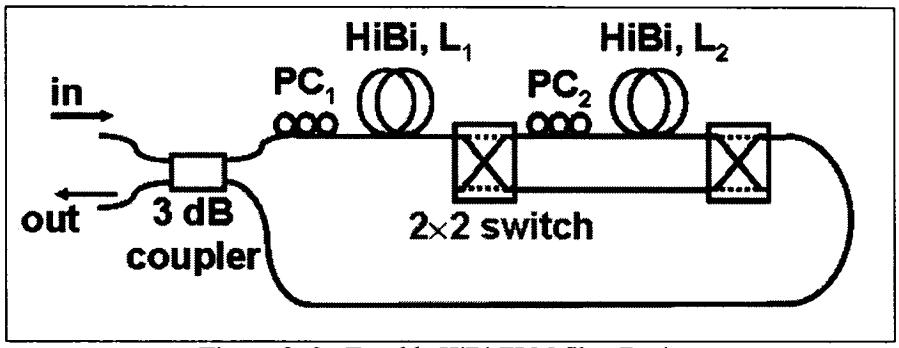

Figure 3- 2: Tunable HiBi-FLM filter Design.

Theoretically, assuming no insertion loss in the coupler and identical attenuation constant α for the HiBi fiber and SMF fiber, the reflected intensity is:

$$R(\lambda) = \exp(-2\alpha\,(l+L))\cos^2(\delta\phi/2) \qquad (15)$$

where $\delta\phi = 2\pi\Delta nL/\lambda$ is the phase difference between fast and slow propagating waves in the HiBi fiber, λ is the wavelength, L is the length of HiBi fiber, Δn is the fiber birefringence, α is the attenuation constant of the fiber, and l is the length of SMF fiber. In the same way, the transmission response is given by:

$$T(\lambda) = 1 - R(\lambda) = (1/2)[1-\cos(\delta\phi)] \qquad (16)$$

In each case, the wavelength spacing between reflected or transmitted peaks is given by [3.1-2]:

$$\Delta\lambda = \lambda^2/\Delta nL \qquad (17)$$

Varying the length of HiBi fiber L will in turn vary the wavelength spacing. In this way, adding 2x2 switches provides for this variability without the need for changing the actual length of HiBi fiber segments in the loop. In the experimental setup, two 2x2 switches are employed in order to provide for two possible wavelength spacings, the last switch also performing the task of a combiner in order to suppress the loss that would otherwise have been induced by such a component.

The HiBi fiber used was a PANDA PM fiber, with a measured birefringence of 3.8×10^{-4} at 1550nm. L has been set to roughly 1.99m. Hence, if the first 2x2 switch is in cross state, the wavelength spacing will be ≈3.2nm. If the switch is in bar state, the length doubles to ≈3.98m and the spacing is thus reduced to ≈1.6nm. Note that the polarization controllers in the FLM are there to adjust the contrast in the filter responses [3.1-2]. The insertion loss of the filter will be the summation of the 3dB coupler loss, the losses induced by each HiBi fiber length (switch-state dependent as well), the loss from the switches themselves, and from the splices between the HiBi and SMF fibers. Also, the final laser cavity length will thus be the addition of the filter lengths with the ring fiber length: approximately ten's of meters in total, rendering a laser with a longitudinal mode spacing in the order of a few megahertz.

3.2.2 Experimental Characteristics

In order to characterize the filter, an EDFA pumped at 50% power is connected to port one of the circulator to obtain both the filter's reflection and transmission responses. For the reflection response, the output is collected at port number three of the circulator, and for the transmission response, directly at the output of the filter. It was found that the initial circulator exhibits around 1.01dB loss from ports 1 to 3, more precisely, 0.65dB from ports 1-2, and 0.36dB from ports 2-3. From these measurements, insertion loss versus wavelength of the filter alone could be obtained for each switch mode (cross and bar states). Figures 3-3 and 3-4 show the transmission and reflection responses of the filter in both switch states, without the circulator or isolator losses, and power normalized to the relative broadband source EDFA spectral shape. Note that all measurements were done using an Optical Spectrum Analyzer (OSA) with a sensitivity of –70dBm and

resolution of 0.06nm. The PCs were optimized separately for each filter and wavelength spacing configurations.

The characteristics of the HiBi-FLM set in cross state, or at approximately 3.2nm wavelength spacing, show the following results: transmission mode exhibits an average of 4.01dB insertion loss, and 23.94dB average contrast; reflection mode has an average of 4.79dB insertion loss, and 21.08dB average contrast. Transmission mode thus exhibits less loss in this state.

In bar state, on the other hand, we find that in transmission mode, there is an average of about 7.62dB insertion loss at the peaks, and 22.58dB contrast between peaks and valleys. In reflection mode, the peak insertion loss is averaged at 7.87dB and the averaged contrast is measured to be 15.55dB. From this comparison, it is clear that the transmission mode offers generally less losses and better peak isolation. The differences in insertion loss between the reflection and transmission modes, however, may be explained by the fact that the coupler employed in the filter exhibits higher losses in cross state, or under the reflection more operation. One also notices more variations in insertion loss across the wavelength range, or between each passbands, in reflection mode. From this, it may be speculated that the polarization was not exactly optimum in reflection mode, and thus that the contrasts may be comparable for both states.

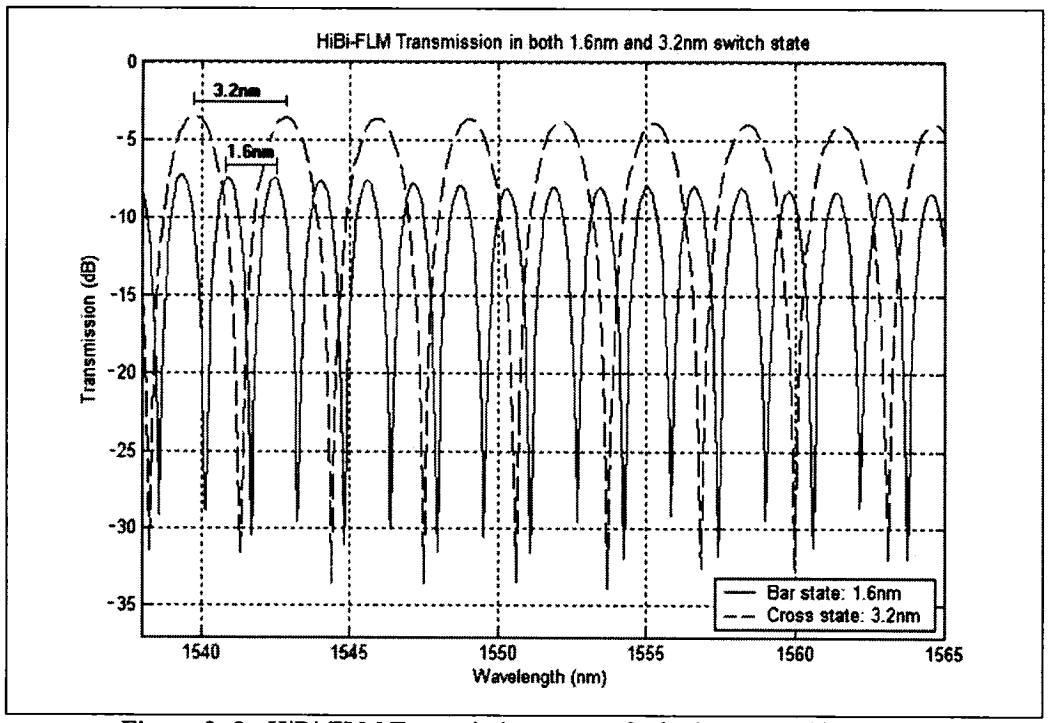

Figure 3- 3: HiBi-FLM Transmission spectra for both cross and bar states.

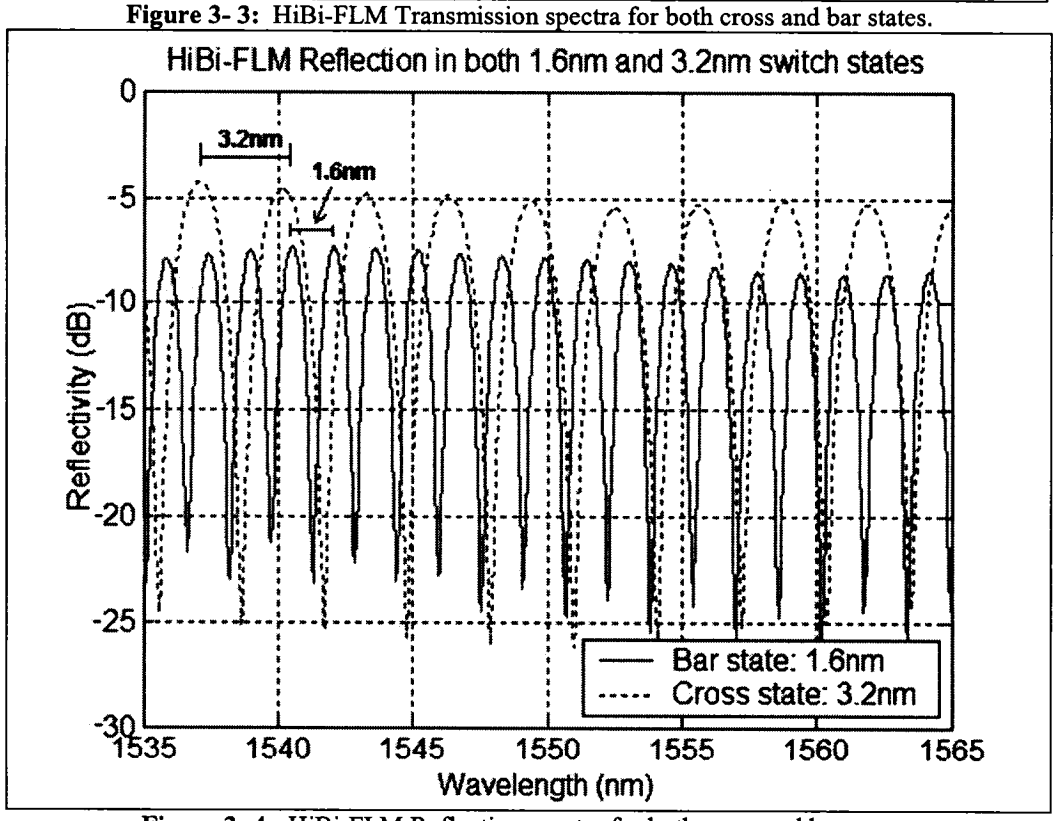

Figure 3- 4: HiBi-FLM Reflection spectra for both cross and bar states.

With the above insertion losses of the filter (without the circulator in reflection mode, or the isolator in transmission mode), the total cavity loss can be found by adding

the circulator loss (1.01dB) in reflection mode, or the isolator loss (0.36dB since ports 2-3 are used as an isolator) when employed in transmission mode. Hence, the losses are 5.37dB and 5.80dB in cross state, and 7.98dB and 8.88dB in bar state for transmission and reflection modes respectively.

It is also interesting to investigate what are the transmission and reflection responses in the case where the polarization controllers (PC) are left unchanged after toggling the switches, or changing the wavelength spacing of the laser. A compromise point must be found, where a relatively acceptable comb filter exists for both wavelength spacings. This is necessary because most applications will require a source that is easily tunable, where only a few switches must be turned, and nothing else adjusted.

Figure 3-5 shows the response of the filter in transmission mode with an optimum PC setting for both switch-states. The cross state has an average peak insertion loss of 4.54dB with an average contrast of 28.58dB, while the bar state has an average peak insertion loss of 8.64dB and average contrast of 18.76dB. These again do not include isolator or circulator losses.

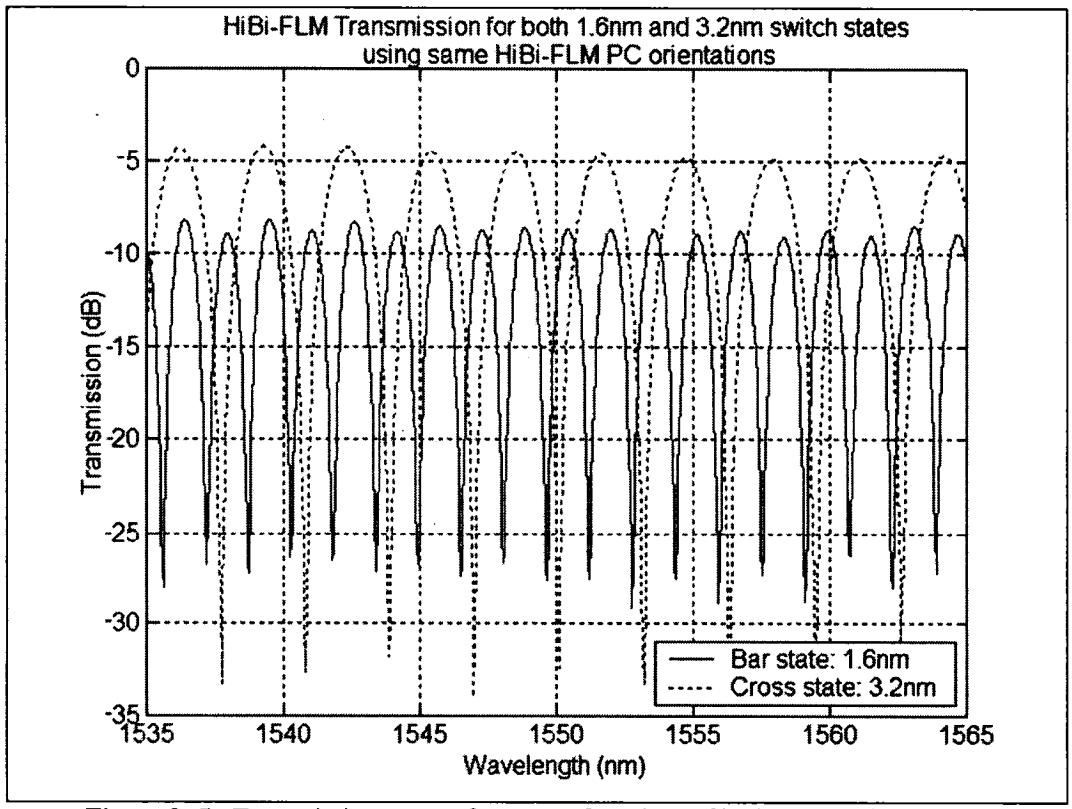

Figure 3- 5: Transmission spectra for same PC settings of both cross and bar states.

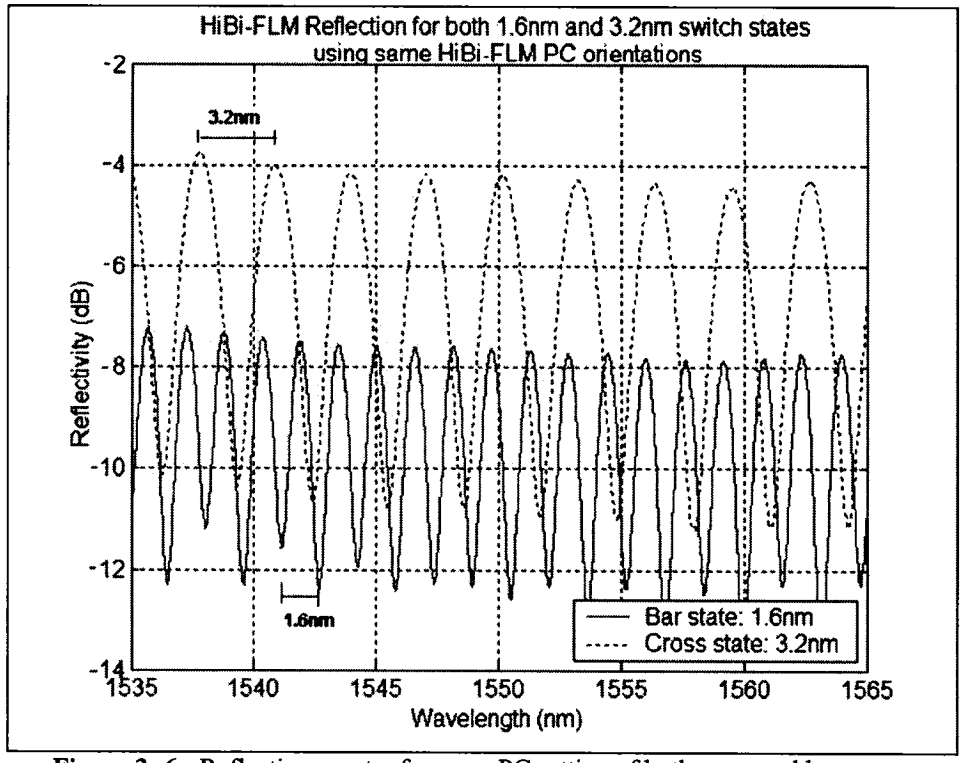

Figure 3- 6: Reflection spectra for same PC setting of both cross and bar states.

Figure 3-6 shows the responses in reflection mode for the same PC orientations than in transmission mode. It is clear that these are not optimum, however, as the bar state offers poor contrast. The cross state has an average peak insertion loss of 4.05dB and average contrast of 6.43dB, while the bar state has an average peak insertion loss of 7.59dB with an average contrast of 4.72dB, without isolator or circulator losses.

The next section will explore how the optimum filter responses affect the overall laser outputs, and if one mode is better than the other, apart from the differences in insertion loss and contrast they produce.

3.3 Possible SFL Implementations

This section presents different SFL implementations, all carefully characterized using either the transmission or reflection mode of the HiBi-FLM filter. The measurements are analyzed in terms of average peak power (APP), number of peaks, maximum peak excursion (MPE) or flatness, signal-to-noise ratio (SNR), peak linewidth range, and stability (variations of peak lasing wavelength and powers in real-time) for later comparison. It is important to note that the states of polarizations were always

optimized independently for each laser and wavelength spacing configurations. The number of selected peaks also followed a careful analysis of the overall output spectrum, and were chosen such that the maximum difference in the peak powers, from the highest to the lowest, remained lower than 6.5dB. In other words, if adding another consecutive peak made the MPE larger than 6.5dB, then it this peak was removed and the lasing wavelength bandwidth was thus reduced.

The first design presented in section 3.3.1 includes a variable optical attenuator (VOA) in the cavity together with one SOA. From theory, a VOA would allow center wavelength tuning, as well as peak power control. However, an increase in intra-cavity loss could in turn decrease output powers, as the nominal insertion loss of the VOA is measured to be approximately 1.90dB, at a 0.0dB setting. To compensate for this, a second SOA is added in section 3.3.2 to offer more gain and to overcome such losses, thereby possibly increasing the lasing output powers or the number of lasing peaks. As explained in section 2.2, this is possible only if the gain spectrum of the second SOA is slightly different than that of the first. Since both available SOAs are relatively similar, it is unlikely that such an addition will give any improvements, but it is nevertheless investigated by using different bias current combinations, PC orientations, and VOA settings. The same two laser implementations but without any VOA are characterized in sections 3.3.3 and 3.3.4 for comparison purposes. Since the HiBi-FLM can either be used in transmission or in reflection mode, each implementation is fully characterized using both modes. Section 3.3.5 compares all the design ideas and chooses the most suitable one.

3.3.1 First Experimental SFL Setup: One SOA and intra-cavity VOA

This section measures the outputs from the SFL implemented using one SOA, SOA 1, and one intra-cavity VOA. All measurements presented in this section, and in all the next ones, were taken with an OSA with -70dBm sensitivity and 0.06nm bandwidth resolution, without any averaging. All stability measures are also obtained over a period of one hour with the same OSA, using a *Labview* algorithm as a recording tool.

HiBi-FLM in Reflection Mode:

We begin by considering the performance of the laser using the HiBi-FLM operating in reflection mode as shown in Figure 3-7.

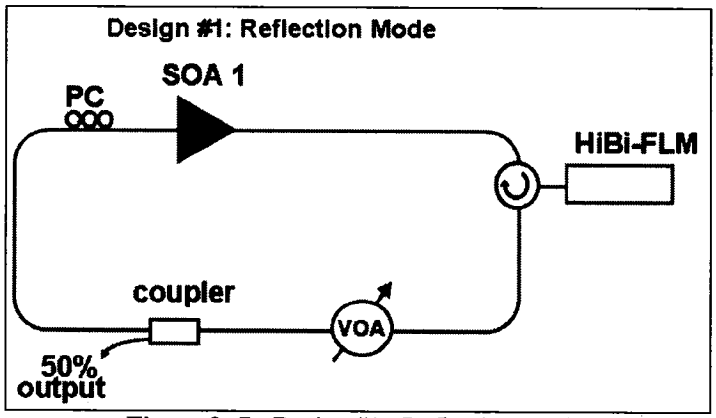

Figure 3- 7: Design #1: Reflection Mode.

a. 3.2nm spacing:

Figure 3-8 presents the output spectra for $\Delta\lambda$ = 3.2nm, with the SOA bias current set at 180mA, and the VOA set at either 0.0, 0.5, and 1.0dB loss respectively. One may also notice the blue-shift effect of increasing intra-cavity loss.

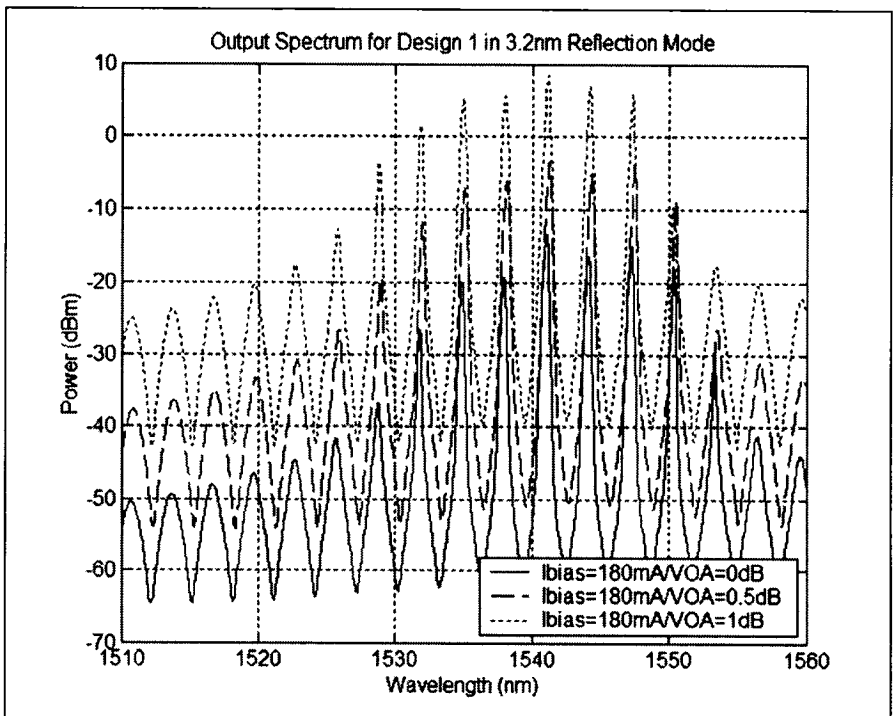

Figure 3- 8: Output spectra for Design #1, 3.2nm spacing in Reflection Mode. Note that 2nd and 3rd spectra (dashed and dotted lines) were offset by +12 and +24dB respectively for clarity purposes.

Table 3-2 presents the characteristics of the corresponding output spectra shown in Figure 3-8. The characteristics for the VOA set at 0.0dB loss, and the bias current set at 140mA, are also presented to give an idea of how the output differs under lower bias currents.

	Characteristics for 3.2nm Reflection Mode			
VOA Settings (dB)	0.0		0.5	1.0
SOA Bias Current (mA)	140	180	180	180
APP (dBm)	-17.15	-16.38	-17.07	-17.64
MPE (dB)	6.44	6.02	3.64	3.28
SNR (dB)	41.33	41.56	44.32	44.60
Linewidth range (nm)	0.17-0.29	0.17-0.28	0.16-0.29	0.18-0.29
Number of Peaks	5	5	5	5

Table 3- 2: Characteristics of SFL Design #1 Output spectra in 3.2nm Reflection Mode.

Stability tests performed over one hour with a bias current of 180mA and a VOA at 0.0dB demonstrate a maximum lasing wavelength deviation of +/- 0.09nm and a maximum power deviation of +/-0.55dB, as shown in figure 3-9.

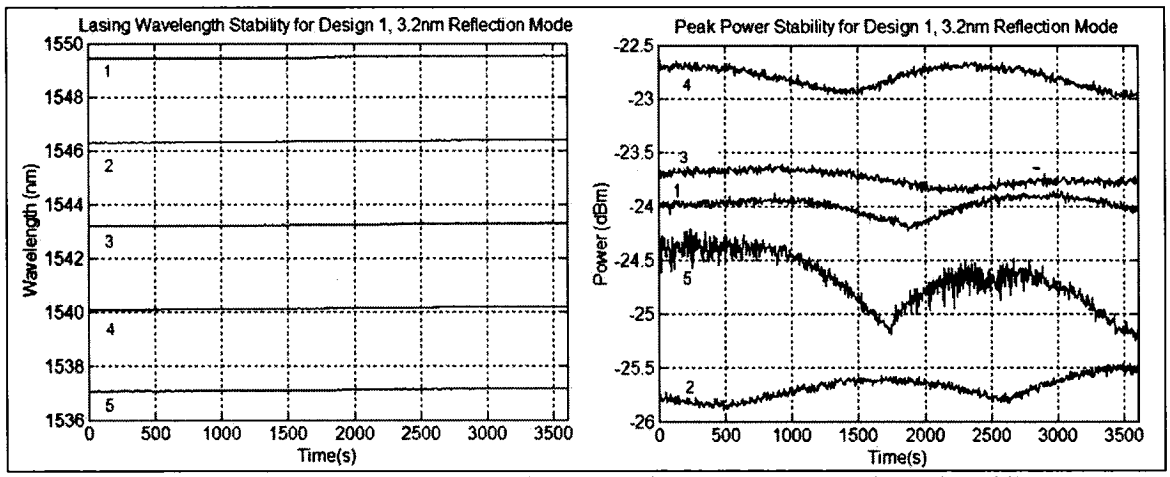

Figure 3- 9: Stability test results for 3.2nm Reflection Mode of Design #1. Each numbered line represents one lasing peak wavelength.

b. 1.6nm spacing:

Figure 3-10 presents the output spectra for $\Delta\lambda$ = 1.6nm, with the SOA bias current set at 180mA, and the VOA set at 0.0, 0.5 and 1.0dB loss respectively.

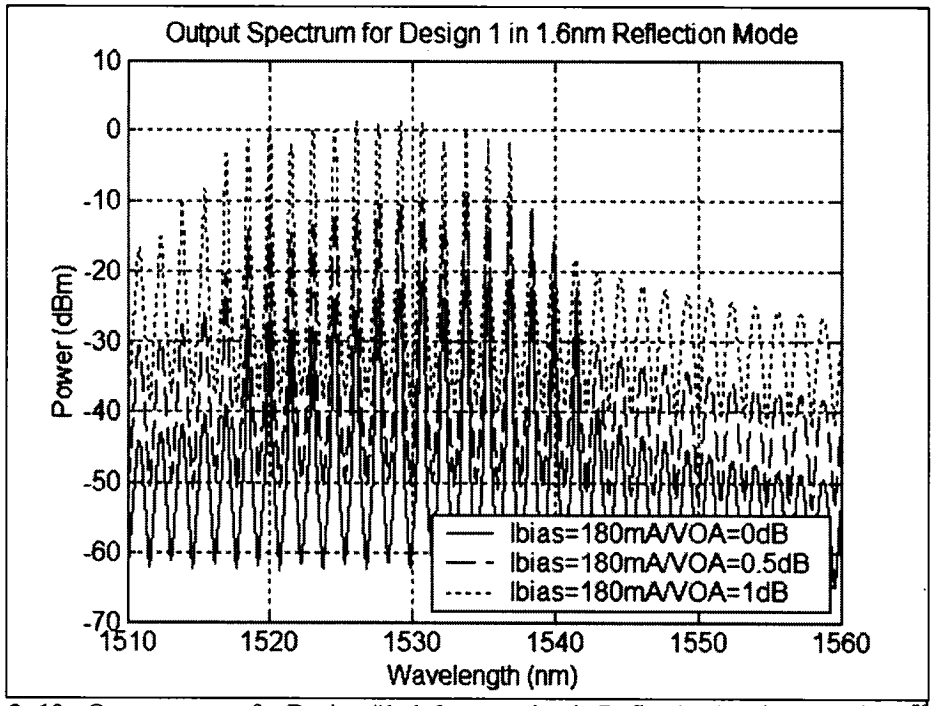

Figure 3- 10: Output spectra for Design #1, 1.6nm spacing in Reflection Mode. Note that 2nd and 3rd spectra (dashed and dotted lines) were offset by +12 and +24dB respectively for clarity purposes.

Table 3-3 compares the characteristics of the corresponding output spectra. The characteristics for the VOA set at 0.0dB, with a bias current set at 140mA, are also presented to give an idea of how the lasing differs under lower bias current.

	Characteristics for 1.6nm Reflection Mode			
VOA Settings (dB)	0.0		0.5	1.0
SOA Bias Current (mA)	140	180	180	180
APP (dBm)	-23.98	-22.67	-23.68	-24.47
MPE (dB)	5.01	4.89	5.44	4.72
SNR (dB)	36.11	36.09	35.16	35.64
Linewidth range (nm)	0.11-0.2	0.12-0.2	0.1-0.2	0.13-0.2
Number of Peaks	12	12	14	14

Table 3- 3: Characteristics of SFL Design #1 Output spectra in 1.6nm Reflection Mode.

Stability tests performed under the same conditions as in the cross state demonstrate a maximum wavelength deviation of +/-0.15nm and a maximum power deviation of +/- 4.16dB. Figure 3-11 shows the measures taken. One notices that the

laser with the HiBi-FLM filter set in bar state experiences more power fluctuations than when it is in cross state. It may be speculated that this instability is due to the increased amount of birefringence in the loop mirror, and especially the narrower wavelength spacing, as indicated in section 3.2, since there is a greater amount of gain competition from the homogeneous broadening effect of the SOA.

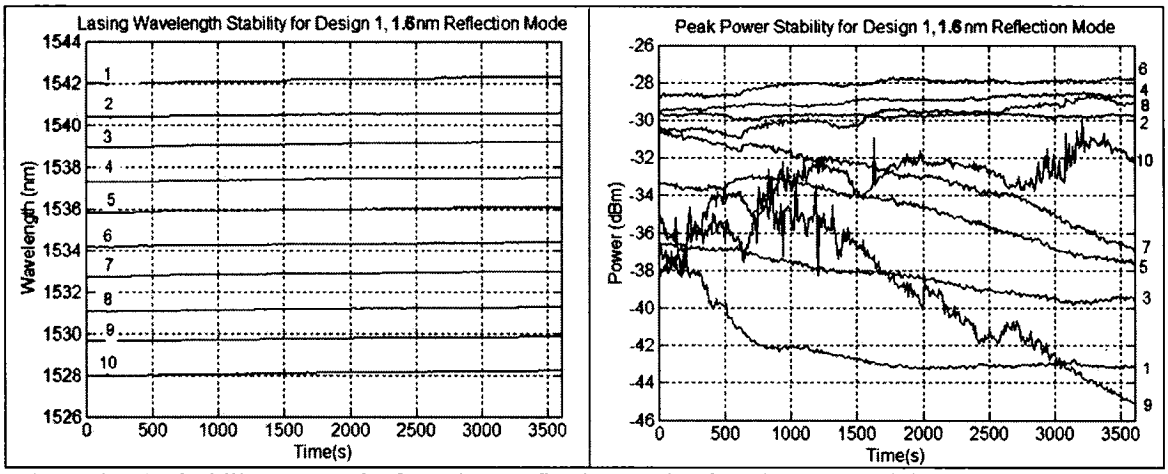

Figure 3- 11: Stability test results for 1.6nm Reflection Mode of Design #1. Each line represents a lasing peak.

HiBi-FLM in Transmission Mode:

Next, we consider the performance of the laser using the HiBi-FLM operating in transmission mode as shown in Figure 3-12.

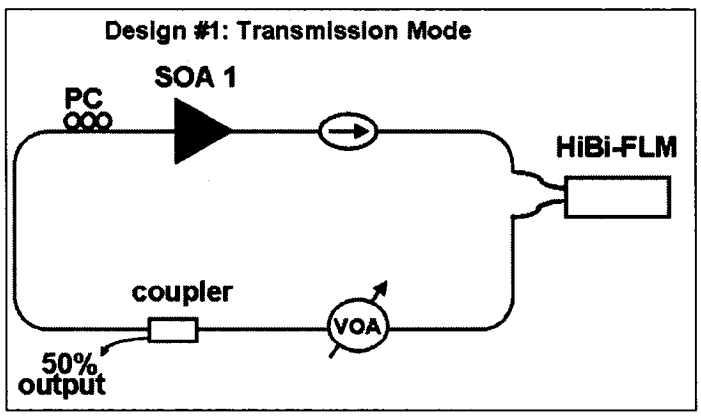

Figure 3- 12: Design #1: Transmission mode

a. 3.2nm spacing:

Figure 3-13 presents the output spectra for $\Delta\lambda$ = 3.2nm, with the SOA bias current set 180mA, and the VOA set at either 0.0, 0.5 and 1.0dB loss respectively.

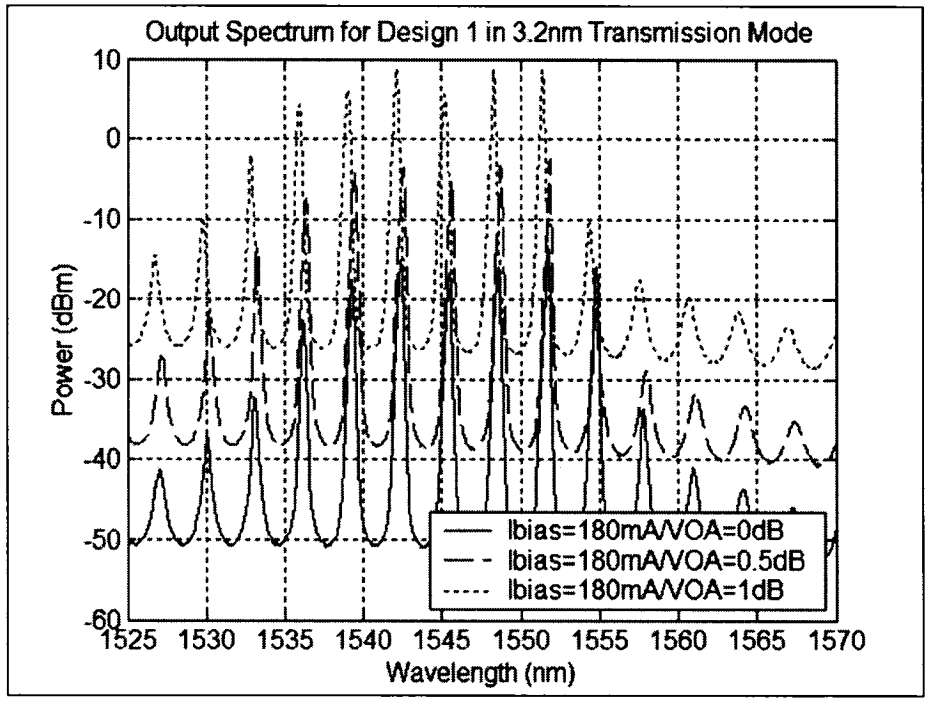

Figure 3- 13: Output spectra for Design #1, 3.2nm spacing in Transmission Mode. Note that 2nd and 3rd spectra (dashed and dotted lines) were offset by +12 and +24dB respectively for clarity purposes.

Table 3-4 presents the characteristics of the corresponding output spectra. The characteristics for the VOA at 0.0dB, with the bias current set at 140mA, are also presented.

	Characteristics for 3.2nm Transmission Mode			
VOA Settings (dB)	0.0		0.5	1.0
SOA Bias Current (mA)	140	180	180	180
APP (dBm)	-16.59	-15.70	-16.23	-16.98
MPE (dB)	6.23	4.21	4.97	4.50
SNR (dB)	32.55	33.41	31.06	30.36
Linewidth range (nm)	0.13-0.22	0.17-0.24	0.15-0.23	0.18-0.24
Number of Peaks	6	6	6	6

Table 3- 4: Characteristics of SFL Design #1 Output spectra in 3.2nm Transmission Mode.

Stability tests performed over one hour under the optimum bias current conditions (180mA), and VOA at 0.0dB, demonstrate a maximum wavelength deviation of +/- 0.05nm and a maximum power deviation of +/- 0.57dB. Figure 3-14 shows the measures taken.

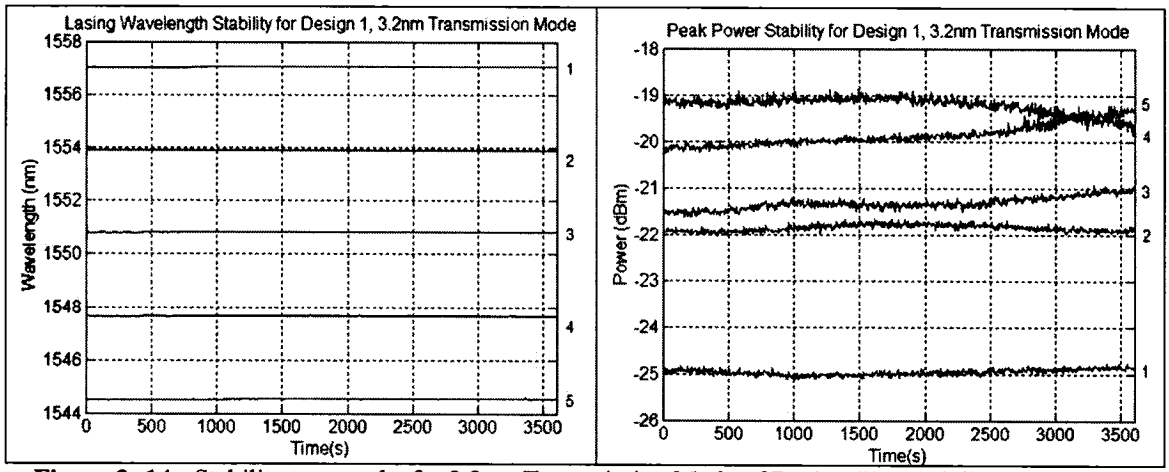

Figure 3- 14: Stability test results for 3.2nm Transmission Mode of Design #1. Each line represents a lasing peak.

b. 1.6nm spacing:

Figure 3-15 presents the output spectra for $\Delta\lambda$ = 1.6nm, with the SOA bias current set at 180mA, and the VOA set at 0.0, 0.5 and 1.0dB loss respectively.

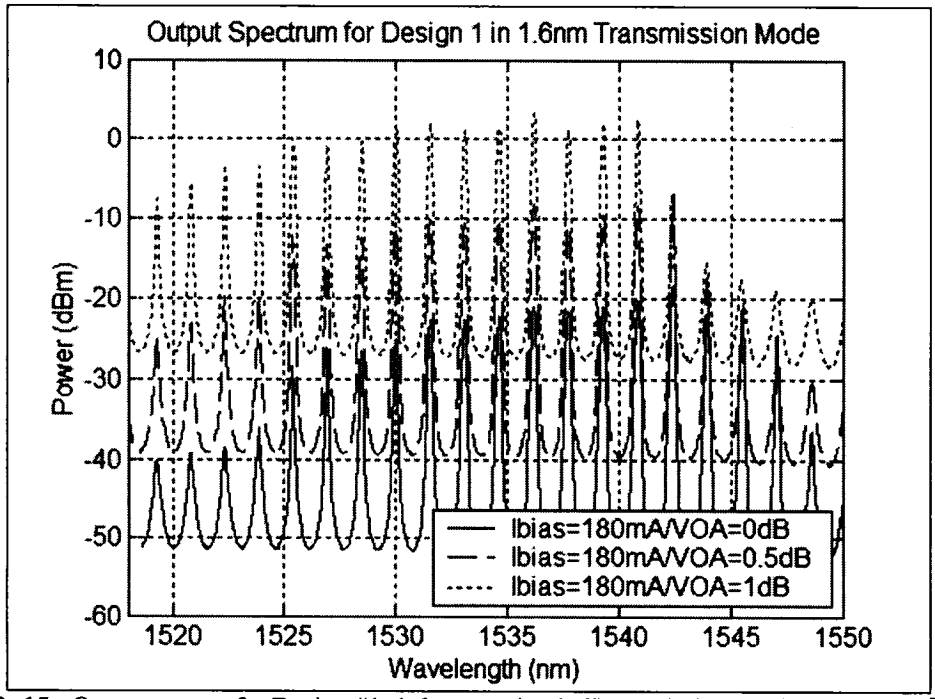

Figure 3- 15: Output spectra for Design #1, 1.6nm spacing in Transmission Mode. Note that 2nd and 3rd spectra (dashed and dotted lines) were offset by +12 and +24dB respectively for clarity purposes.

Table 3-5 presents the characteristics of the corresponding output spectra. The characteristics for the VOA at 0.0dB, and a bias current set at 140mA, are presented as well.

	Characteristics for 1.6nm Transmission Mode			
VOA Settings (dB)	0.0		0.5	1.0
SOA Bias Current (mA)	140	180	180	180
APP (dBm)	-22.19	-21.49	-22.42	-22.70
MPE (dB)	6.04	6.19	6.24	4.12
SNR (dB)	28.15	29.05	25.97	26.09
Linewidth range (nm)	0.11-0.16	0.11-0.17	0.12-0.16	0.13-0.17
Number of Peaks	10	11	12	11

Table 3- 5: Characteristics of SFL Design #1 Output spectra in 1.6nm Transmission Mode.

From figure 3-16 below, the stability tests performed under the same settings as in the cross state demonstrate a maximum wavelength deviation of +/-0.08nm and a maximum power deviation of +/- 3.85dB. The same instability reasons as in the reflection mode may be speculated upon.

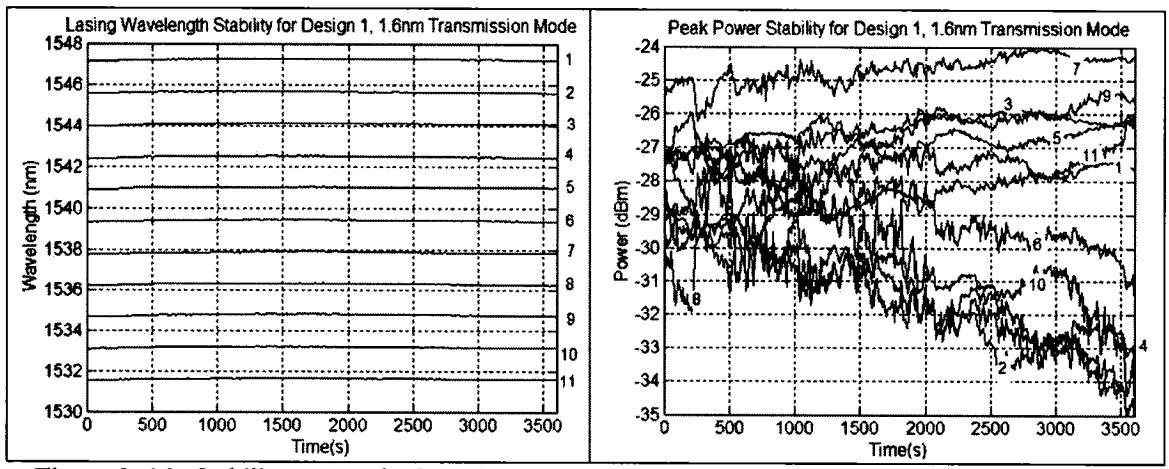

Figure 3- 16: Stability test results for 1.6nm Transmission Mode of Design #1. Each line represents a lasing peak.

3.3.2 Second Experimental SFL Setup: Two SOAs and intra-cavity VOA

This section performs the characterization of the SFL laser implemented using two SOAs and one VOA. As explained previously, different bias currents, PC orientations and VOA setting combinations are tested for in order to verify if two SOAs do increase the overall bandwidth of the laser spectrum, the output powers or even the peak flatness. Once the ultimate bias current settings are found with the VOA set at 0.0dB, the measures are retaken with the VOA delivering both 0.5dB and 1.0dB loss in the cavity, on top of its nominal 1.90dB loss. The same measurement conditions are kept as in the previous section.

HiBi-FLM in Reflection Mode:

We begin by considering the performance of the laser using the HiBi-FLM operating in reflection mode as shown in Figure 3-17.

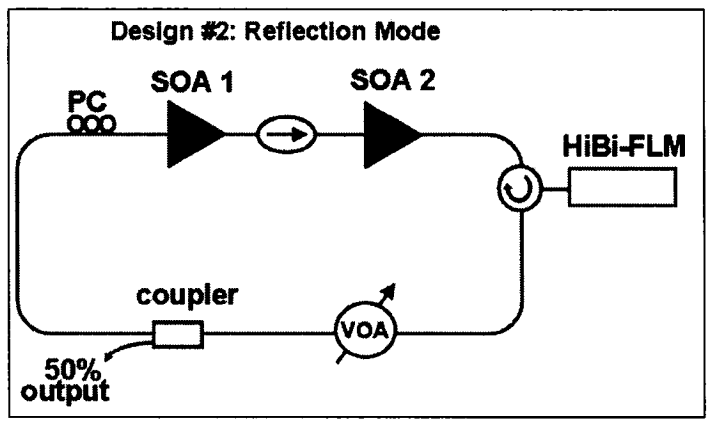

Figure 3- 17: Design # 2: Reflection Mode.

a. 3.2nm spacing

Figure 3-18 presents the output spectra of this second laser design for $\Delta\lambda = 3.2$nm, with 180mA SOA bias currents, and the VOA set at 0.0, 0.5 and 1.0dB loss respectively.

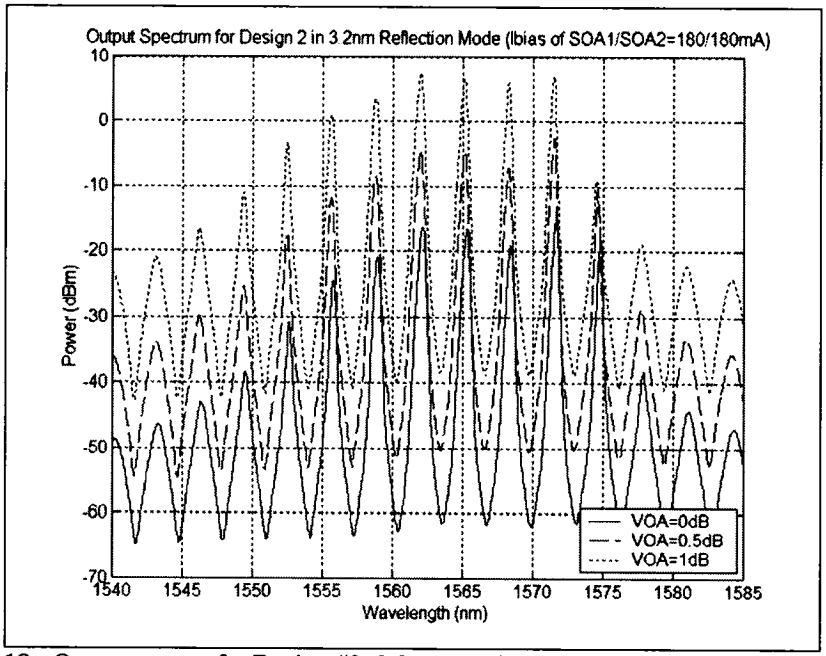

Figure 3- 18: Output spectra for Design #2, 3.2nm spacing in Reflection Mode. The bias current combination for the output spectra shown is kept at 180mA for both SOAs, the best combination found for this mode spacing. Note that 2nd and 3rd spectra (dashed and dotted lines) were raised by +12 and +24dB respectively for clarity purposes.

Table 3-6 below presents the characteristics of the corresponding output spectra. The output characteristics for the VOA at 0.0dB loss, with more combinations of bias currents, are also presented to show how the lasing differs under different biasing conditions and to find the best combination of currents.

	Characteristics for 3.2nm Reflection Mode						
VOA Settings (dB)	**0.0**					**0.5**	**1.0**
SOA Bias Currents (mA) (SOA1/ SOA2)	100/ 180	140/ 180	180/ 180	180/ 140	180/ 100	180/ 180	180/ 180
APP (dBm)	-17.09	-16.45	-16.93	-17.40	-18.52	-17.57	-17.87
MPE (dB)	5.59	5.56	5.04	4.63	5.44	6.04	3.95
SNR (dB)	42.61	42.49	42.64	42.53	41.78	42.97	43.63
Linewidth range (nm)	0.25-0.34	0.23-0.35	0.24-0.33	0.23-0.34	0.22-0.31	0.22-0.33	0.24-0.34
Number of peaks	5	4	5	5	5	5	5

Table 3- 6: Characteristics of SFL Design #2 Output spectra in 3.2nm Reflection Mode.

Figure 3-19 below, demonstrates that the stability tests performed using the optimum bias current combination (180/180mA), with the VOA set at 0.0dB, again for one hour, show a maximum wavelength deviation of +/-0.07nm and a maximum power deviation of +/- 0.10dB.

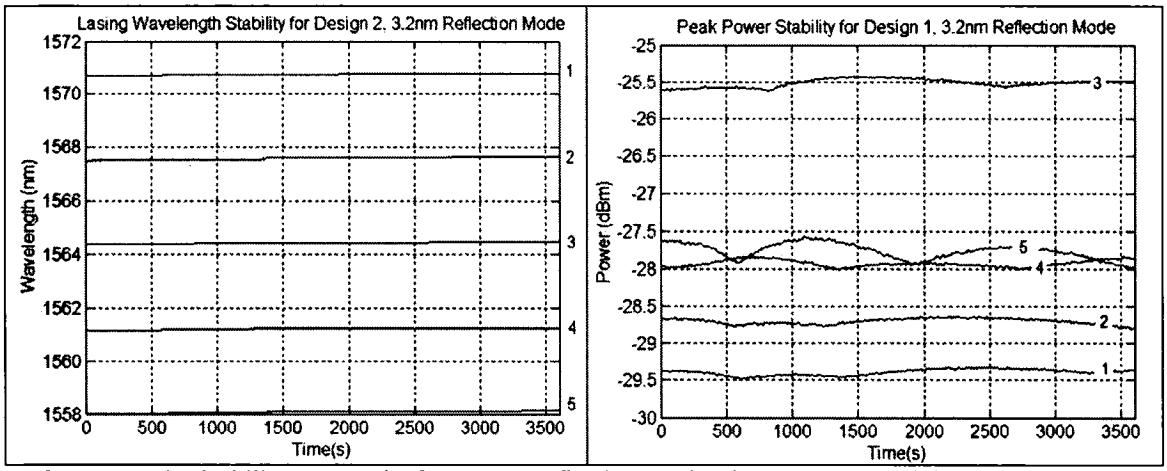

Figure 3- 19: Stability test results for 3.2nm Reflection Mode of Design #2. Each line represents one lasing peak wavelength.

b. 1.6nm spacing

Figure 3-20 now presents the output spectra of this second laser design for $\Delta\lambda$ = 1.6nm with the SOA 1 bias current set 180mA, and the SOA 2 bias current set at 140mA. The VOA is also varied to either 0.0, 0.5 and 1.0dB loss respectively.

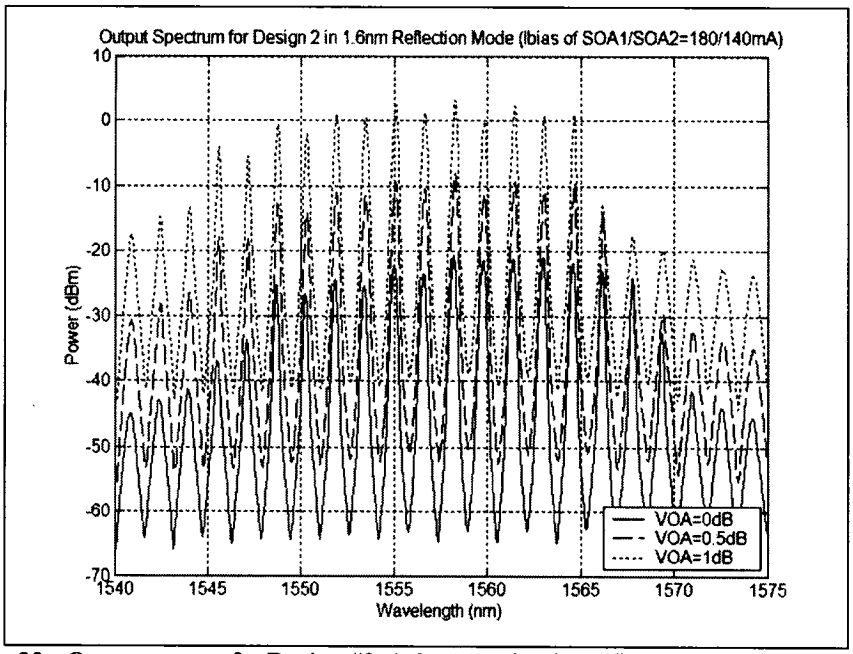

Figure 3- 20: Output spectra for Design #2, 1.6nm spacing in Reflection Mode. The bias current combination for the output spectra shown is kept at 180mA for both SOA 1 and 140mA for SOA 2; the best combination found for this mode spacing. Note that 2nd and 3rd spectra (dashed and dotted lines) were raised by +12 and +24dB respectively for clarity purposes.

Table 3-7 presents the characteristics of the corresponding output spectra. The characteristics for the VOA at 0.0B with more combinations of bias currents are also presented, as in the previous case.

	Characteristics for 1.6nm Reflection Mode						
VOA Settings (dB)	**0.0**					**0.5**	**1.0**
SOA Bias Currents (mA) (SOA1/ SOA2)	100/ 180	140/ 180	180/ 180	180/ 140	180/ 100	180/ 140	180/ 140
APP (dBm)	-22.18	-21.67	-22.25	-23.14	-23.57	-23.00	-23.20
MPE (dB)	6.27	5.05	5.89	6.04	5.29	5.86	5.23
SNR (dB)	38.48	39.63	38.62	37.53	37.14	37.02	38.69
Linewidth range (nm)	0.16- 0.27	0.17- 0.26	0.15- 0.27	0.14- 0.23	0.15- 0.23	0.16- 0.28	0.17- 0.26
Number of peaks	11	10	11	13	11	12	11

Table 3- 7: Characteristics of SFL Design #2 Output spectra in 1.6nm Reflection Mode.

Figure 3-21 below, demonstrates that the stability tests with a 180/140mA bias current combination, and VOA at 0.0dB, show a maximum wavelength deviation of +/- 0.08nm and a maximum power deviation of +/- 1.11dB. One may again speculate on the same reasons as before regarding the bar state power instabilities.

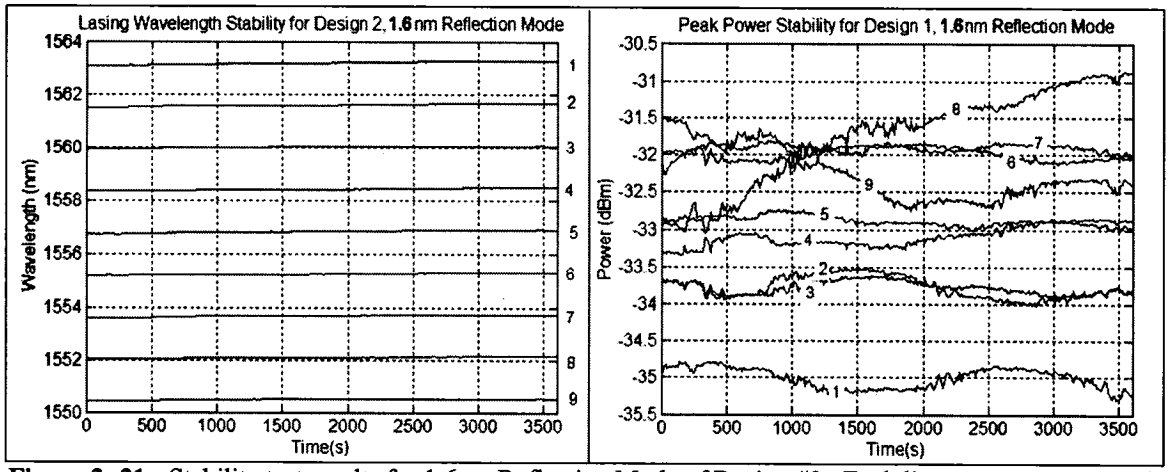

Figure 3- 21: Stability test results for 1.6nm Reflection Mode of Design #2. Each line represents one peak wavelength.

HiBi-FLM in Transmission Mode:

Next, we consider the performance of this second laser design using the HiBi-FLM operating in transmission mode.

a. 3.2nm spacing

Figure 3-22 presents the output spectra for $\Delta\lambda$ = 3.2nm, with the SOA bias currents both set at 180mA, and the VOA set either at 0.0, 0.5 and 1.0dB loss respectively.

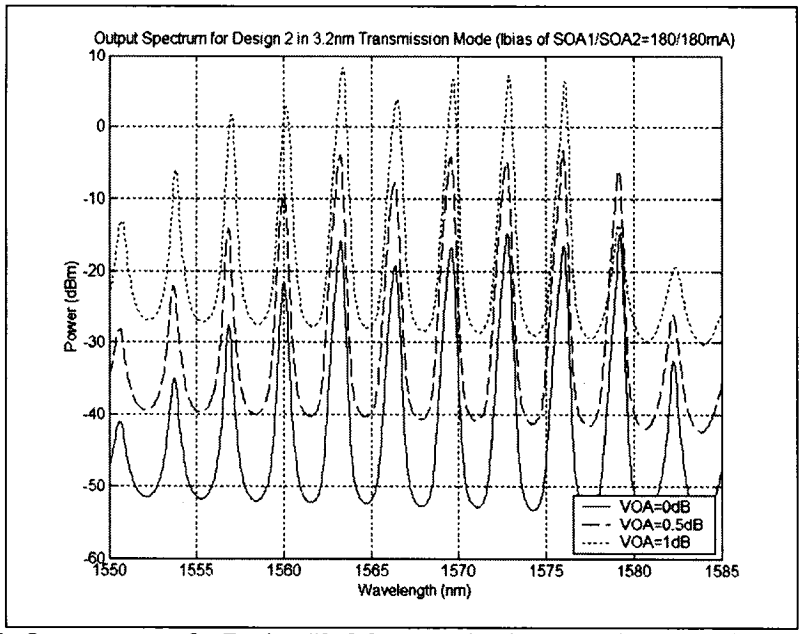

Figure 3- 22: Output spectra for Design #2, 3.2nm spacing in Transmission Mode. The bias current combination for the output spectra shown is kept at 180mA for both SOAs, the best combination found for this mode spacing. Note that 2nd and 3rd spectra (dashed and dotted lines) were raised by +12 and +24dB respectively for clarity purposes.

Table 3-8 presents the characteristics of the corresponding output spectra, together with the characteristics for the VOA at 0.0dB with more bias current combinations.

	Characteristics for 3.2nm Transmission Mode						
VOA Settings (dB)	**0.0**					**0.5**	**1.0**
SOA Bias Currents (mA) (SOA1/ SOA2)	100/ 180	140/ 180	180/ 180	180/ 140	180/ 100	180/ 180	180/ 180
APP (dBm)	-12.67	-16.51	-16.38	-16.88	-17.94	-20.52	-18.16
MPE (dB)	6.01	4.21	4.43	5.42	6.13	5.98	5.43
SNR (dB)	34.76	33.87	33.08	32.26	31.08	30.77	30.30
Linewidth range (nm)	0.2- 0.34	0.25- 0.34	0.24- 0.36	0.22- 0.36	0.19- 0.34	0.19- 0.37	0.2-0.35
Number of peaks	4	6	6	6	6	7	6

Table 3- 8: Characteristics of SFL Design #2 Output spectra in 3.2nm Transmission Mode.

Figure 3-23 below, demonstrates the stability tests under again 180/180mA bias current setting, and the VOA set at 0.0dB. These show a maximum wavelength deviation of +/-0.05nm and a maximum power deviation of +/- 0.26dB.

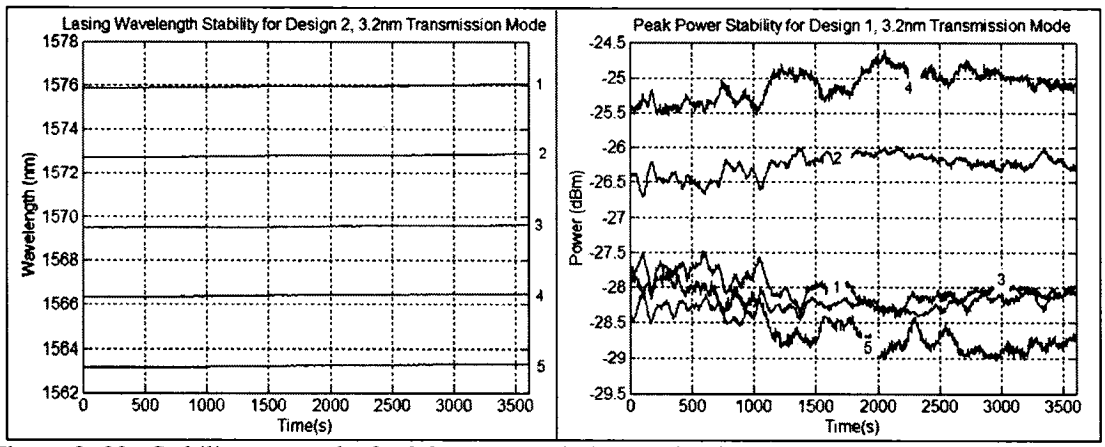

Figure 3- 23: Stability test results for 3.2nm Transmission Mode of Design #2. Each line represents one lasing peak.

b. 1.6nm spacing

Figure 3-24 presents the output spectra for $\Delta\lambda$ = 1.6nm, with the SOA1 bias current set at 140mA, the SOA2 bias current set at 180mA, and the VOA varied to either 0.0, 0.5 and 1.0dB loss respectively.

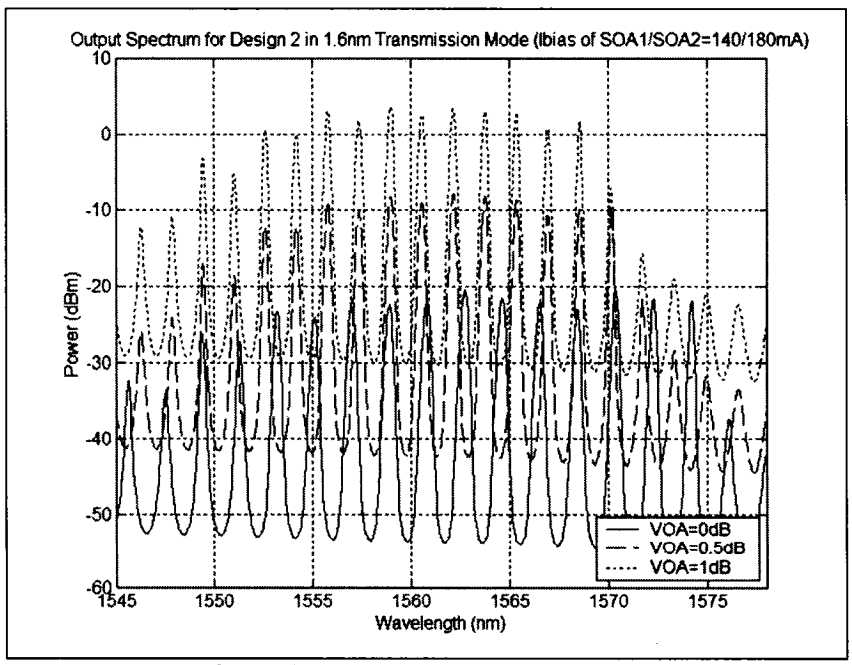

Figure 3- 24: Output spectra for Design #2, 1.6nm spacing in Transmission Mode. The bias current combination for the output spectra shown is kept at 140mA for both SOA 1 and 180mA for SOA 2; the best combination found for this mode spacing. Note that 2nd and 3rd spectra (dashed and dotted lines) were raised by +12 and +24dB respectively for clarity purposes.

Table 3-9 presents the characteristics of the corresponding output spectra, together with the characteristics for the VOA at 0.0dB with more combinations of bias currents.

	Characteristics for 1.6nm Transmission Mode						
VOA Settings (dB)	**0.0**					**0.5**	**1.0**
SOA Bias Currents (mA) (SOA1/ SOA2)	100/ 180	140/ 180	180/ 180	180/ 140	180/ 100	140/ 180	140/ 180
APP (dBm)	-20.79	-21.18	-21.97	-22.11	-23.36	-21.68	-21.95
MPE (dB)	3.96	4.00	5.40	3.54	4.64	4.43	3.68
SNR (dB)	32.84	30.67	27.64	29.10	26.97	29.43	29.48
Linewidth range (nm)	0.17-0.26	0.18-0.28	0.19-0.26	0.18-0.27	0.17-0.25	0.18-0.24	0.18-0.25
Number of peaks	11	12	14	12	12	12	11

Table 3- 9: Characteristics of SFL Design #2 Output spectra in 1.6nm Transmission Mode..

Figure 3-25 below, shows the results of the stability test performed under the optimum 140/180mA bias current combination, and VOA set at 0.0dB. The maximum wavelength deviation is +/-0.14nm and the maximum power deviation is +/- 0.99dB. The bar state peak powers are once again more unstable than in the cross state. We also notice the effects of gain competition between the lines.

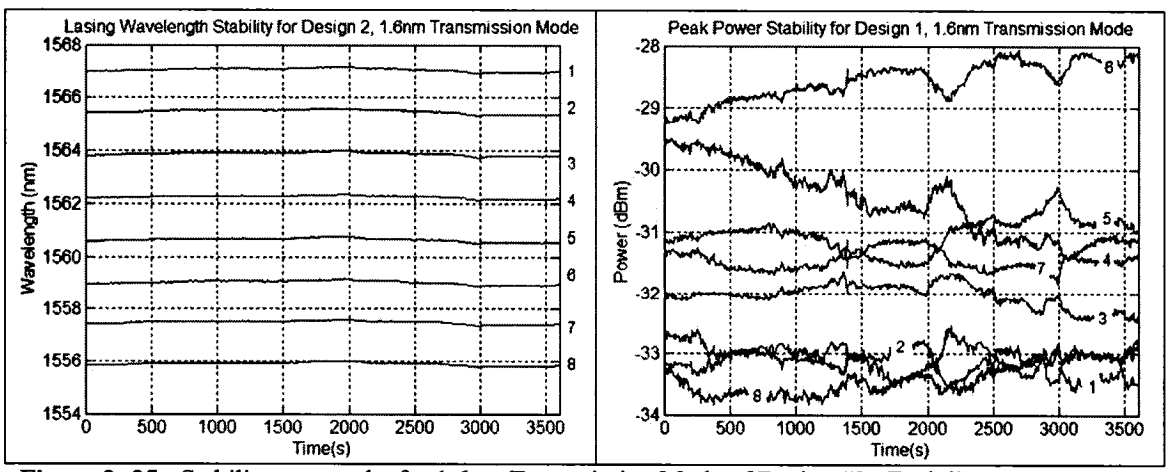

Figure 3- 25: Stability test results for 1.6nm Transmission Mode of Design #2. Each line represents one lasing peak wavelength.

3.3.3 Third Experimental SFL Setup: One SOA

In order to verify clearly whether or not it is necessary to use a VOA for better peak power control, both implementations previously characterized are re-investigated without the use of a VOA. More characterizations will help in better deciding if the second SOA really does improve the peak powers and the number of peaks obtained. From the analysis of the results already collected, it seems that the second SOA is driven close to saturation, and thus does not improve much on the gain. Also, since both SOAs have very similar gain spectrums, we can only hope to increase the number of lasing peaks by a small amount.

Nonetheless, each setup must be investigated in order to find the best compromise. This section thus presents the results obtained for the case where the VOA is eliminated and only one SOA is kept, operating at a bias current of 180mA. The following section 3.3.4 employs two SOAs in the loop, with again different bias currents and PC orientation combinations. Since the final implementation decision will be taken mostly upon the comparison of parameters such as output powers, number of peaks and MPE, the stability measurements were not performed in this section as well as in the next. In the case where the final design does not incorporate the VOA, stability measurements will be completed in order to obtain full final characteristics.

HiBi-FLM in Reflection Mode:

First, we consider the performance of the laser using the same configuration as shown in Figure 3-7, but without the VOA.

Figure 3-26 presents the output spectra of this third laser design for the two switch states, or mode spacings, and with the SOA bias current set at 180mA.

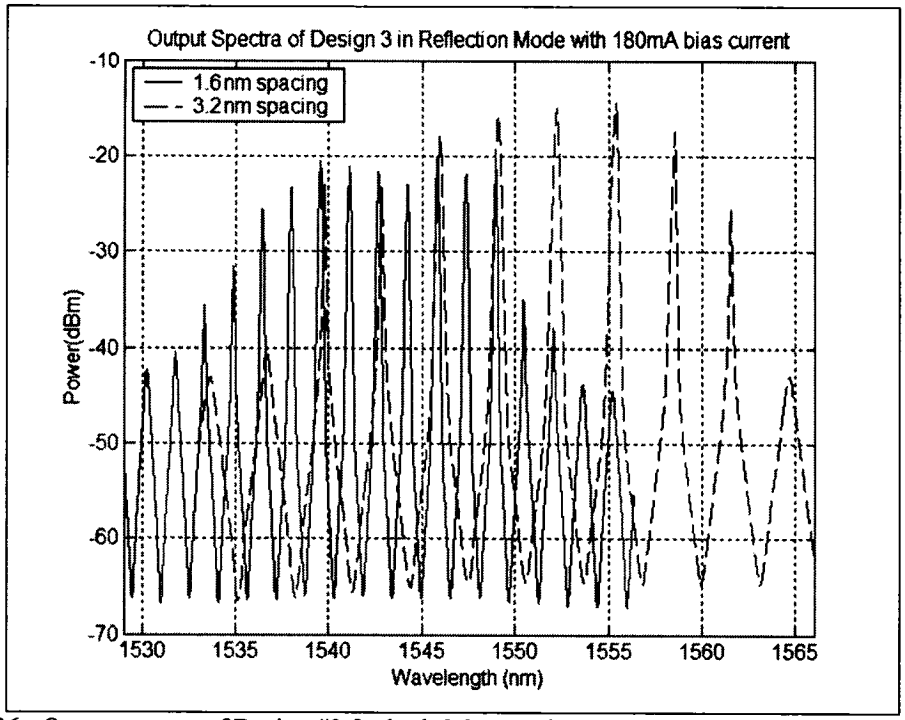

Figure 3- 26: Output spectra of Design #3 for both 3.2nm and 1.6nm spacings with filter in reflection mode.

Table 3-10 presents the characteristics of the corresponding output spectra.

	Characteristics in Reflection Mode	
Wavelength Spacing	**3.2nm**	**1.6nm**
SOA Bias Current (mA)	180	180
APP (dBm)	-16.19	-21.99
MPE (dB)	3.79	5.68
SNR (dB)	46.52	40.70
Linewidth range (nm)	0.1-0.22	0.09-0.15
Number of peaks	5	9

Table 3- 10: Characteristics of SFL Design #3 Output spectra for both wavelength spacing obtained using the filter in Reflection Mode.

HiBi-FLM in Transmission Mode:

Next, we consider the same laser implementation, but this time using the HiBi-FLM filter in transmission mode instead. Hence, the configuration is similar to the one shown in Figure 3-12, but without the VOA in the laser cavity.

Figure 3-27 presents the output spectra of this laser design for the two switch states, and with the SOA bias current set at 180mA.

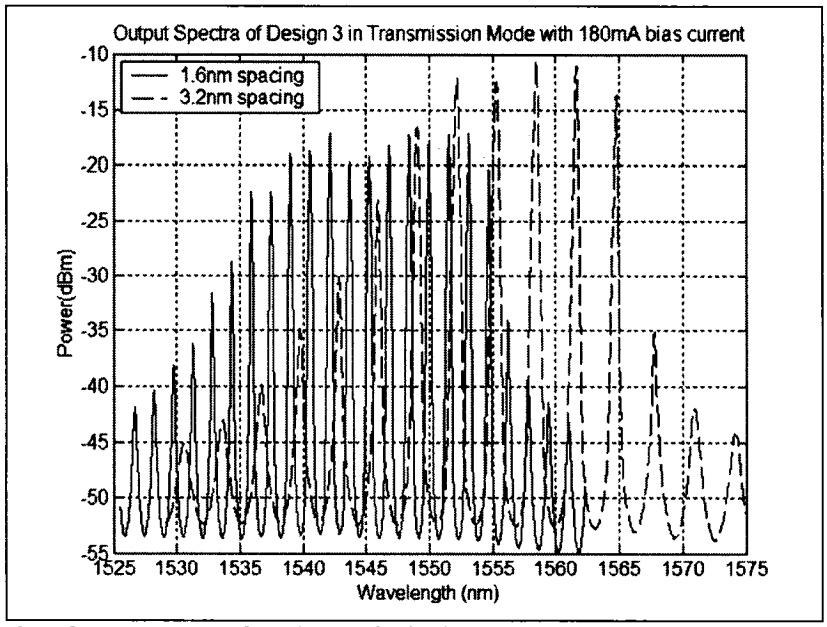

Figure 3- 27: Output spectra of Design #3 for both 3.2nm and 1.6nm spacings with the filter in transmission mode.

Table 3-11 presents the characteristics of the corresponding output spectra.

	Characteristics in Transmission Mode	
Wavelength Spacing	**3.2nm**	**1.6nm**
SOA Bias Current (mA)	180	180
APP (dBm)	-12.72	-18.97
MPE (dB)	6.03	5.36
SNR (dB)	35.78	31.13
Linewidth range (nm)	0.17-0.28	0.17-0.2
Number of peaks	6	13

Table 3- 11: Characteristics of SFL Design #3 Output spectra for both wavelength spacings in Transmission mode.

3.3.4 Fourth Experimental SFL Setup: Two SOAs

HiBi-FLM in Reflection Mode:

First, we consider the performance of the laser using the same configuration as shown in Figure 3-17, but without the VOA.

a. 3.2nm spacing:

Figure 3-28 presents the output spectra of this fourth laser design for $\Delta\lambda$ = 3.2nm, and with several SOA bias current combinations.

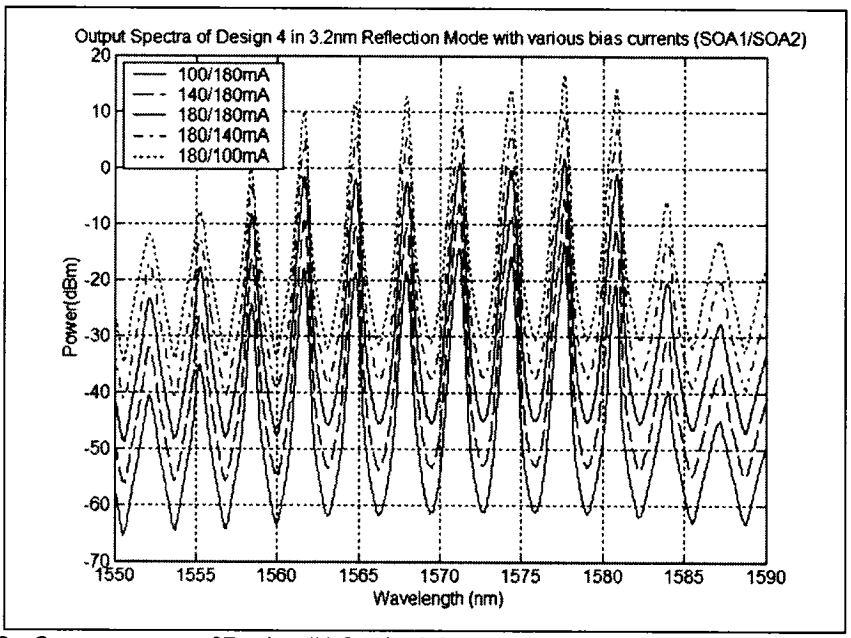

Figure 3- 28: Output spectra of Design #4 for the 3.2nm spacing in reflection mode. The different bias current combinations are shown for each line, where the first (100/180mA combination) is plotted with the real output powers, and the subsequent ones are shifted upwards by +8dB each for clarity purposes.

b. 1.6nm spacing:

Figure 3-29 presents the output spectra for $\Delta\lambda$ = 1.6nm with several SOA bias current combinations.

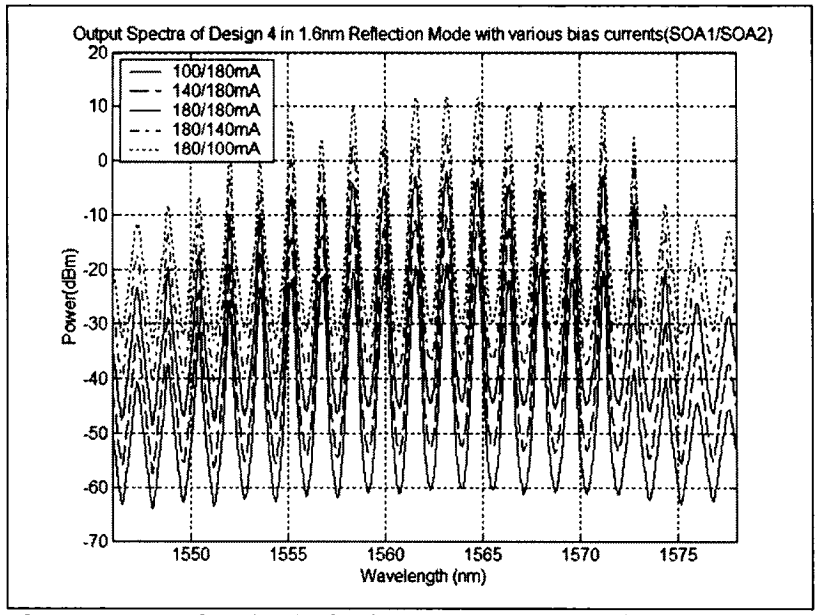

Figure 3- 29: Output spectra of Design #4 for the 1.6nm spacing in reflection mode. The different bias current combinations are shown for each line, where the first (100/180mA combination) is plotted with the real output powers, and the subsequent ones are shifted upwards by +8dB each for clarity purposes.

Table 3-12 presents the characteristics of the corresponding output spectra, with both the cross and bar filter switch states.

	Characteristics in Reflection Mode									
Wavelength Spacing	**3.2nm**					**1.6nm**				
Bias Currents (mA) (SOA1/ SOA2)	100 / 180	140 / 180	180 / 180	180 / 140	180 / 100	100 / 180	140 / 180	180 / 180	180 / 140	180 / 100
APP (-dBm)	16.03	16.73	16.59	17.26	17.90	21.68	21.27	20.48	20.48	20.79
MPE (dB)	5.19	5.04	4.42	4.70	4.83	4.40	5.77	5.84	6.05	4.56
SNR (dB)	42.99	42.64	42.93	43.18	43.36	38.06	37.56	39.48	38.65	38.31
Linewidth range (nm)	0.20-0.29	0.21-0.33	0.23-0.33	0.24-0.31	0.22-0.29	0.14-0.22	0.14-0.21	0.13-0.22	0.13-0.21	0.13-0.22
Number of peaks	5	7	7	7	6	9	12	12	12	12

Table 3- 12: Characteristics of SFL Design #4 – Reflection Mode Output spectra for both wavelength spacings.

HiBi-FLM in Transmission Mode:

Now, we consider the same laser implementation as above, but this time using the HiBi-FLM filter in transmission mode instead. Hence, the configuration is similar to Figure 3-17, without the VOA.

a. 3.2nm spacing:

Figure 3-30 presents the output spectra of this fourth laser design for $\Delta\lambda$ = 3.2nm and with several SOA bias current combinations.

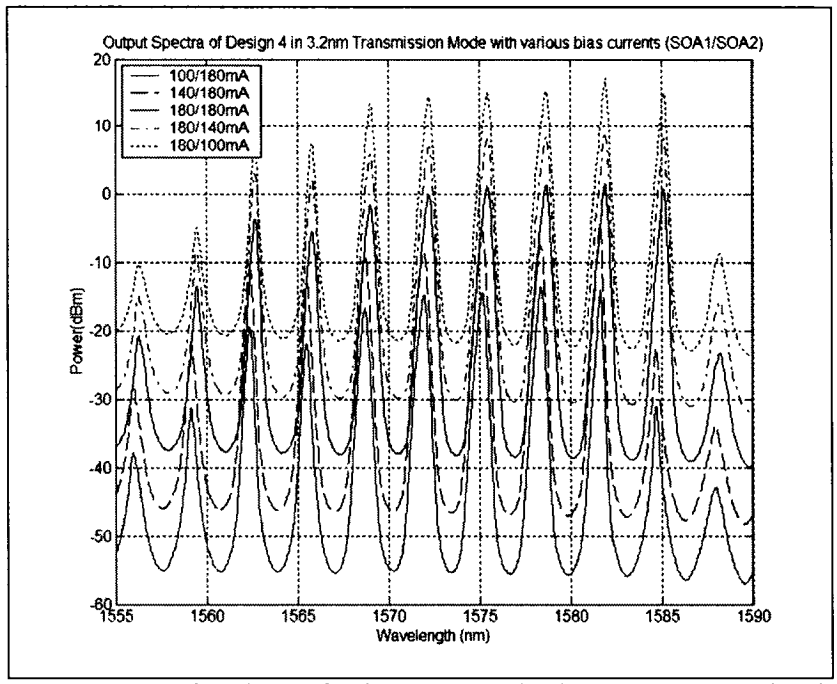

Figure 3- 30: Output spectra of Design #4 for the 3.2nm spacing in transmission mode. The different bias current combinations are shown for each line, where the first (100/180mA combination) is plotted with the real output powers, and the next ones are shifted upwards by +8dB each for clarity purposes.

b. 1.6nm spacing:

Figure 3-31 presents the output spectra of this fourth laser design for $\Delta\lambda$ = 1.6nm and with several SOA bias current combinations.

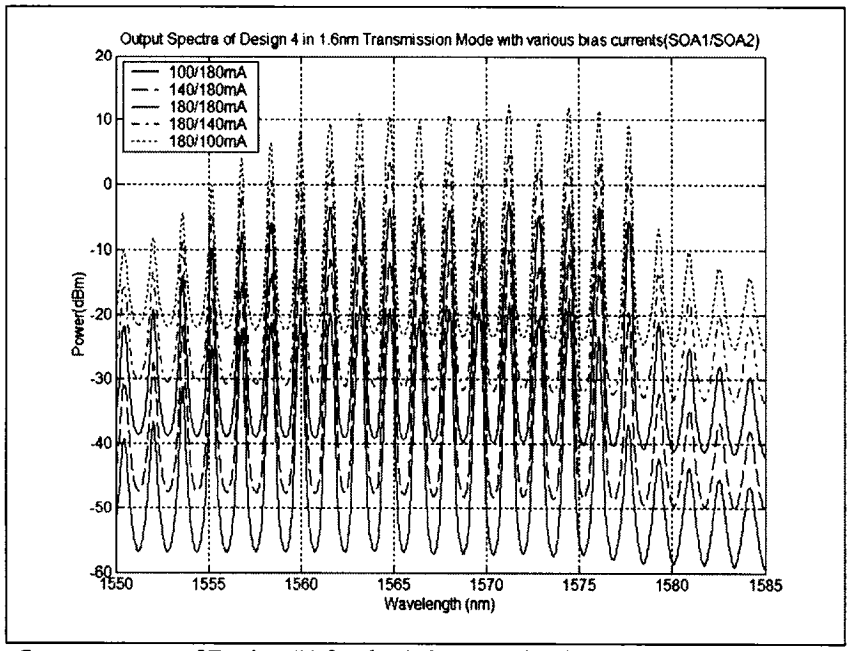

Figure 3- 31: Output spectra of Design #4 for the 1.6nm spacing in transmission mode. The different bias current combinations are shown for each line, where the first (100/180mA combination) is plotted with the real output powers, and the next ones are shifted upwards by +8dB each for clarity purposes.

Table 3-13 presents the characteristics of the corresponding output spectra, both under the cross and bar filter switch states.

	Characteristics in Transmission Mode									
Wavelength Spacing	**3.2nm**					**1.6nm**				
Bias Currents (mA) (SOA1/ SOA2)	100 / 180	140 / 180	180 / 180	180 / 140	180 / 100	100 / 180	140 / 180	180 / 180	180/ 140	180/ 100
APP (-dBm)	14.68	14.92	15.49	16.14	17.04	21.94	21.04	20.27	19.97	19.71
MPE (dB)	3.14	4.71	3.04	3.29	3.93	5.9	6.05	4.90	4.93	4.89
SNR (dB)	38.48	37.35	36.41	35.72	34.67	28.71	29.66	31.71	32.81	34.62
Linewidth range (nm)	0.18-0.32	0.21-0.35	0.25-0.37	0.24-0.35	0.25-0.33	0.16-0.24	0.17-0.24	0.17-0.24	0.17-0.23	0.14-0.22
Number of peaks	5	5	6	6	6	13	14	14	13	12

Table 3- 13: Characteristics of SFL Design #4 -- Transmission Mode Output spectra for both wavelength spacing.

3.3.5 Comparison of All Four Designs

It was initially stated that the best laser design should offer the most number of output peaks for the highest peak powers and smallest MPE. Linewidths are also preferred smaller for later applications. After collecting and analyzing all the data presented in sections 3.3.1 to 3.3.4, some conclusions must be taken and a final design implementation will be kept for later use in the two proposed applications.

By analysis of the characteristics of each setup, and more precisely by comparing the ones with and without the presence of a VOA, one readily notices that the use of such a component does not readily provide for better flatness, and mostly reduces output peak powers and contrasts (or SNRs). Since the VOA-induced blue-shifting effect of the whole wavelength spectrum is also not of much interest for later applications, this component is therefore readily taken out of the SFL design. From laboratory tests and from previous literature review, the best way to make the peaks flatter without the VOA is to use the polarization dependency of the most vulnerable SOA, or SOA 1. As such, a flatness of up to 3.1 dB has been obtained with the third setup, or employing only one SOA in the cavity.

The next step is to verify if the second SOA, without the VOA, improves furthermore the output characteristics. According to all the measures, the presence of the second SOA seems to decrease the contrasts by about 3dB and increase the number of lasing peaks by only one or two at most (and in turn decrease the average peak powers), while the flatness, or MPE, remains relatively the same. The linewidths, however, experience a net gain mostly in the 3.2nm spacing modes when using two SOAs. This increase in peak linewidths will not be very convenient for later applications such as the time-of-flight measurement of chromatic dispersion in fiber spools, as it may impose a maximum limit on the amount of measurable dispersion. The setup resulting in the smallest linewidths is thus the best.

Finally, one readily notices that the transmission mode offers less insertion loss, and thus higher output peak powers (3-5dB higher compared with the filter in reflection mode), but gives lower SNRs (about 7dB decrease depending on the specific laser implementation). This is somewhat in contradiction with the higher extinction ratios of the transmission HiBi-FLM response characteristics provided in section 3.2.2, but it may

be explained simply by the possibility that the sates of polarizations were not optimized as precisely as in the reflection modes. Nevertheless, the decision upon noticing the lower line contrasts present in transmission mode, is to keep this same laser implementation instead of the reflection mode because of the higher peak powers it provides, which will be of greater importance for future applications.

3.4 Final Design Implementation and Characterization

The final implementation will hence employ only one SOA, the most polarization dependant, SOA 1, in order to keep better flatness control and reduce MPEs via PC control. The HiBi-FLM is also employed in transmission mode for the reasons mentioned in the previous section, while a single isolator is included in the cavity to assure unidirectional propagation. The final configuration is thus similar to the one shown in Figure 3-12 with the VOA removed.

The characteristics of the final design are hence similar to those presented in section 3.3.3 with the FLM employed in transmission mode. Please refer to this section for spectra measures and characteristics.

Briefly, the cross state offers lasing wavelengths in the upper C-band, that is between 1545-1565nm, while the bar state tends to have lasing peaks between 1535-1560nm. One may also decrease the measured MPE by considering a reduced number of lasing peaks. Hence, again for a driving current of 180mA, the multi-wavelength source set in the cross state (3.2nm spacing) offers about 5 lasing peaks at an average power of -11.96dBm, for a total power of -4.83dBm. With this number of peaks, the maximum peak excursion is 3.11dB, taken across the 5 peaks offering highest powers, and the signal to noise ratio (SNR) is 39.20dB. Each peak has a linewidth between 0.17 and 0.28nm. Stability tests (figure 3-32a) performed for one hour show a maximum lasing wavelength deviation of +/-0.05 nm and a maximum peak power deviation of +/- 0.59dB.

In the bar state, considering the 11 highest lasing lines, giving an average power of -18.35dBm, for a total power of -8.06dBm, the maximum peak excursion is 3.19dB, while the SNR is 33.55dB, and the linewidths are within 0.17nm and 0.2nm. The maximum lasing wavelength deviation is +/-0.09 nm and the maximum peak power deviation is +/- 0.90dB when measured over one hour with an SOA bias current of

180mA (figure 3-32b). These results show, once again, greater power instability compared to the cross state, possibly due to the increased amount gain competition in the fiber loop mirror due to the smaller wavelength spacing. The polarization properties of the laser where not exactly measured, but the lines were previously shown to possess a random elliptical polarization in a similar laser configuration [3.1].

Since the states of the PCs have a different effect on the generated output spectra under the various types of filter setups (transmission or reflection, 1.6nm or 3.2nm spacing), most of the measures presented in this section were obtained using the optimum PC settings for each considered implementation. It is however important to show that the laser can operate at both 1.6nm and 3.2nm spacing without varying the states of polarizations. This is a feature of capital importance for ease of use in future applications. Figure 3-33 presents a proof that such an operation is possible. The output spectra shown are obtained when all PC orientations are kept the same for both wavelength spacings. Finally, we note that there exists a tradeoff between flatness of the lasing peaks and bandwidth: the best flatness is obtained for the least number of lasing peaks. Figures 3-34 a) and b) demonstrate this by presenting several output spectra with different PC orientations.

a)

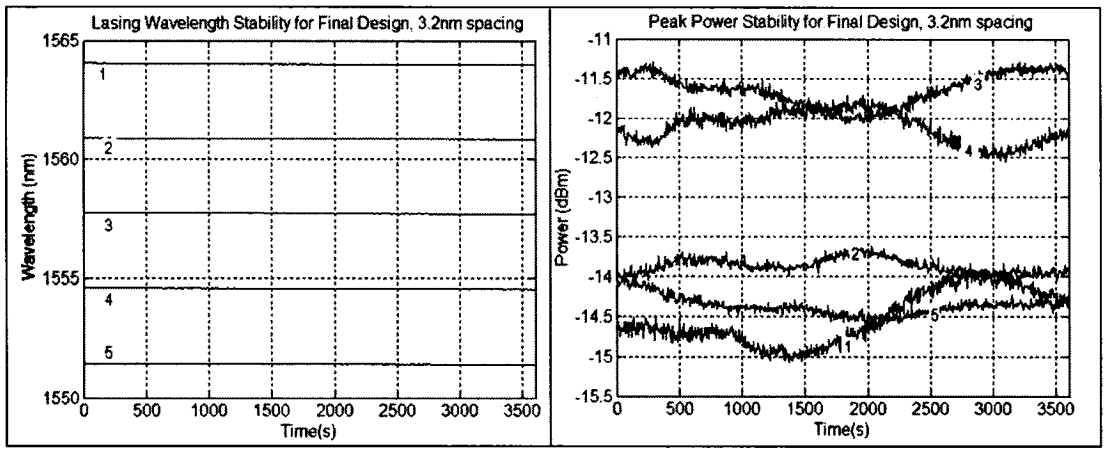

b)

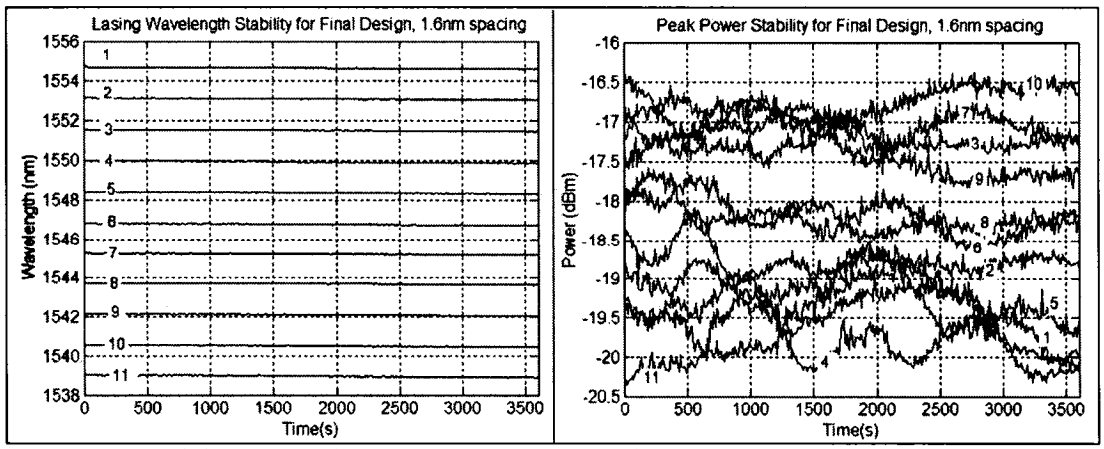

Figure 3- 32: Stability test results for (a) 3.2nm spacing and (b) 1.6nm spacing. Each line represents one lasing peak wavelength.

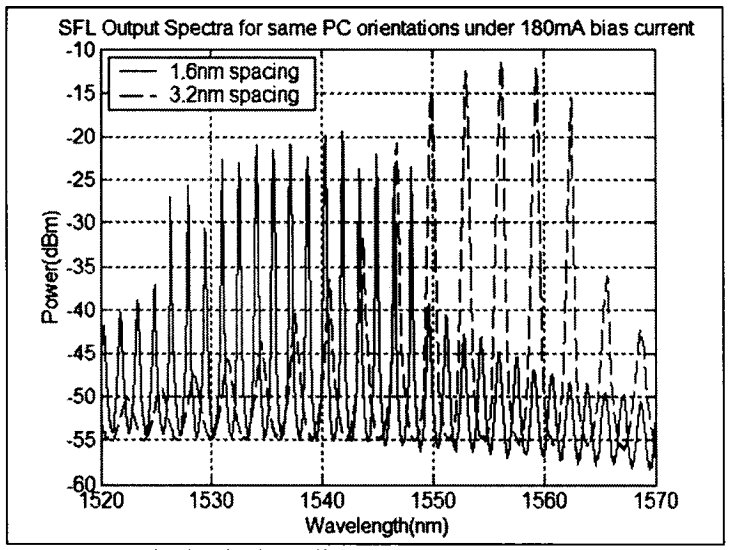

Figure 3- 33: Output spectra obtained when all PC orientations are kept the same for both wavelength spacing.

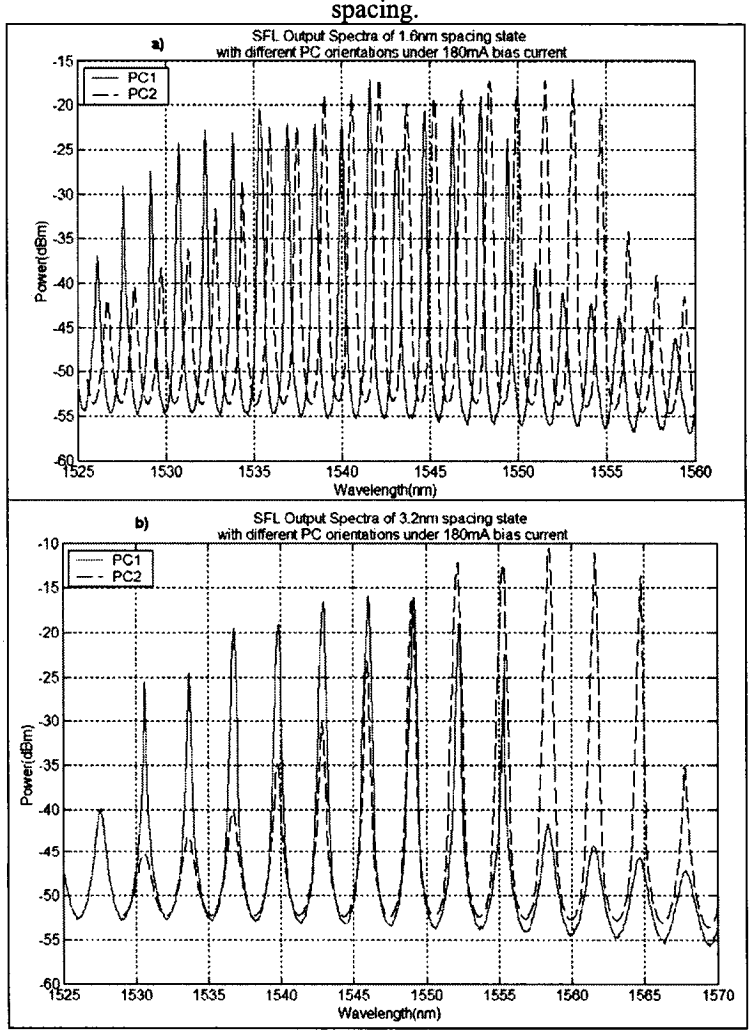

Figure 3- 34: Tradeoff between flatness of the lasing peaks and bandwidth with varied PC orientations: (a) for the cross state and (b) for the bar state.

3.5 Conclusion

The final SFL implementation has been decided upon and characterized in section 3.4 after multiple implementation trials. Each design attempt has given an insight on how the SFL could yet again be improved in the near future. For example, a second SOA with a different gain spectrum could offer a larger output spectrum bandwidth, greater peak powers, and better flatness when the SOAs are appropriately biased and the polarization-state is optimized. The possibility of wavelength-shifting the entire lasing spectrum while keeping the same wavelength spacing could also be offered using an intra-cavity VOA, provided that either the amplifiers offer higher gain, or the intra-cavity loss is reduced. Power fluctuations between modes could also be reduced, and stability improved upon, if the amplifiers were replaced by linear optical amplifiers, which are less affected by gain competition in the laser cavity, as explained in chapter 2 [3.3]. This would also reduce the gain competition experienced in the smallest wavelength spacing mode, and thus improve upon stability. Finally, power equalization and spectrum broadening could be offered by using a single-pass optical feedback arm in the output of the laser implemented with two SOAs [3.4], and peak powers could be better controlled using a fiber Bragg grating with a flat or apodized notch profile. All these additions would again be more expensive. The initial goal of offering a reliable, yet relatively simple and affordable solution was thus accomplished.

3.6 References

3.1 L. R. Chen. "Tunable multiwavelength fiber ring lasers using a programmable high-birefringence fiber loop mirror," *IEEE Photonics Technology Letters*, vol. 16, no.2, pp. 410-412, February 2004.

3.2 Y. Shiquan, L. Zhaohui, D. Xiaoyi, Y. Shuzhong, K. Guiyun, and Z. Qida. "Generation of wavelength-switched optical pulse from a fiber ring laser with F-P semiconductor modulator and a HiBi fiber loop mirror," *IEEE Photonics Technology Letters*, vol. 14, no.6, pp. 774-776, June 2002.

3.3 K. K. Qureshi, H.Y.Tam, W.H. Chung, and P.K.A. Wai. "Multiwavelength laser source using linear optical aAmplifier," *IEEE Photonics Technology Letters*, vol. 17, no. 8, pp. 1611-1613, August 2005.

3.4 N. Pleros, C. Bintjas, M. Kalyvas, G. Theophilopoulos, K. Yiannopoulos, S. Sygletos, and H. Avramopoulos. "Multiwavelength and power equalized SOA laser sources," *IEEE Photonics Technology Letters*, vol. 14, no.5, pp. 693-695, May 2002.

Other Readings:

- H. Dong, G. Zhu, Q. Wang, H. Sun, N.K. Dutta, J. Jaques, and A.B. Piccirilli. "Multiwavelength fiber ring laser source based on a delayed interferometer," *IEEE Photonics Technology Letters*, vol. 17, no.2, pp. 303-305, February 2005.
- H. Chen. "Multiwavelength fiber ring lasing by use of a semiconductor optical amplifier," *Optics Letters*, vol. 30, no. 6, pp. 619-621, March 15, 2005.
- G. Keiser, *Optical Fiber Communications*, 3rd Edition. Boston: McGraw-Hill (2000)
- B-A. Yu, J. kwon, S. Chung, S-W. Seo and B. Lee. "Multiwavelength-switchable SOA-fibre ring laser sampled Hi-Bi fibre grating," *Electronics Letters*, vol. 39, no.8, pp. 649-650, April 17th, 2003.

IV. First Application: Chromatic Dispersion Measurements using Time-Of-Flight Method

The recent development of wavelength division multiplexed (WDM) optical systems was a major step in meeting the ever-growing bandwidth demand. Further increase in network capacity can be accomplished either by adding more wavelengths or by modulating the channels at higher rates. As the data or channel rates increase, however, nonlinear effects and chromatic dispersion issues become increasingly important. These may cause severe signal degradation if not compensated for or properly controlled. Making accurate measurements of chromatic dispersion is thus an important step towards managing such phenomena. Many measurement methods have been proposed, but the ultimate solution should ideally be simple, fast, low cost, and permit the measurement of long, already-deployed fiber links [4.1].

This chapter demonstrates a new and improved method for measuring the chromatic dispersion of optical fiber based on the time-of-flight (TOF) technique using the tunable multi-wavelength semiconductor fiber laser (SFL) previously implemented and characterized in chapter 3. Section 4.1 briefly explains the chromatic dispersion phenomena and exposes the different measurement techniques recognized by the International Telecommunications Union (ITU). The experimental setup employed to collect the TOF measurements is then summarized in section 4.2, together with the data analysis method necessary for making effective measurements. The various experimental results are fully revealed in section 4.3. The TOF measurements are finally compared to those obtained using the conventional phase-shift technique; section 4.4 explains how the phase-shift measurements were performed and summarizes the collected data, while section 4.5 fully compares both sets of measures. The errors are then analyzed, and future measurement recommendations are made in section 4.6. The (SFL) proves to offer many advantages over its predecessors since it is fast, simple, relatively low-cost, and yet reliable for such dispersion measurements.

4.1 Chromatic Dispersion and its ITU Recognized Measurement Techniques

Chromatic Dispersion is the intramodal dispersion that occurs as a pulse travels along a length of waveguide, and is also known as group velocity dispersion or GVD. It comprises both waveguide and material dispersion effects [4.2], and is a phenomenon of great importance in single-mode waveguides. Material dispersion occurs because the index of refraction in the fiber varies with wavelength. Thus different spectral components in a given signal will travel at a different speed, thus contributing to pulse spreading. Waveguide dispersion arises as the waveguide propagation constant and effective mode index varies with wavelength, once material dispersion is neglected. In single-mode fibers, waveguide dispersion becomes important because only 80 percent of the optical power is concentrated in the core, while the other 20 percent of the light propagates in the cladding where it travels faster than the energy in the core. The amount of dispersion will thus also depend on the fiber design, especially the core radius variation along the fiber length. [4.2]

As a modulated signal travels along a fiber length, each wavelength component experiences different time delays or group delay per unit length in the direction of propagation:

$$\tau_g(\lambda)/L = 1/V_g = 1/c(d\beta/dk) = -\lambda^2/2\pi c(d\beta/d\lambda) \text{ [ps/km]} \quad (18)$$

where L is the distance traveled by the pulse, c is the speed of light, β is the propagation constant along the fiber, $k = 2\pi/\lambda$, and group velocity, V_g, is the velocity at which the energy of the pulse travels. The amount of pulse spreading along the fiber will thus depend on group delay variation with respect to wavelength.

For an optical source with a small spectral width, the delay difference per unit wavelength along the length of fiber approaches $d\tau_g/d\lambda$. For spectral components $d\lambda$ apart, centered at λ_o, the total delay $d\tau$ difference over a distance L is:

$$d\tau = (d\tau_g/d\lambda)\, d\lambda = (-L/2\pi c)\,[2\lambda(d\beta/d\lambda) + \lambda^2(d^2\beta/d\lambda^2)]d\lambda \quad \text{[ps/nm]} \quad (19)$$

$$= L(d^2\beta/d\omega^2)d\omega\,, \quad \text{in terms of angular frequency} \quad (20)$$

where $\beta_2 = d^2\beta/dw^2$ is the group velocity dispersion GVD parameter. Hence, for a pulse with a spectral root-mean square (rms) width of σ_λ, its pulse spreading will be approximated by its rms pulse width according to:

$$\sigma_g = |d\tau_g/d\lambda|\sigma_\lambda = DL\sigma_\lambda \quad (21)$$

$$\text{where } D = (1/L)\, d\tau_g/d\lambda = -2\pi c\beta_2/\lambda^2 \quad (22)$$

is the dispersion parameter, or the pulse spread per unit fiber length as a function of wavelength change, which is measured in ps/(nm-km) [4.2].

There are three principal methods recognized by the ITU for measuring chromatic dispersion: interferometric, phase-shift, and time-of-flight [4.3]. In the first approach, an interferometer is employed, where one arm is the fiber under test, and the other arm is the reference fiber with a well-known group delay profile. The measured cross-correlation will vary according to the time delay between both arms of the interferometer. This technique is very accurate but limited to short lengths of fibers [4.1]. The phase-shift technique has been predominantly used in the industry by several commercially available chromatic dispersion measurement instruments [4.3]. In this case, the input signal is amplitude modulated. The phase of the transmitted signal envelope is compared with a reference input signal in order to obtain the group delay. This measurement is performed over a range of different wavelengths, and thus requires a certain amount of time to scan the desired wavelength range [4.4, 4.5]. The differential phase-shift technique modulates the input signal both in amplitude and frequency, while scanning over the wavelength range, making the measurement more immediate. The phase-shift method permits the precise measurement of both long and short fiber lengths, as well as passive fiber components such as fiber Bragg gratings. Unfortunately, this technique usually relies on a reference signal [4.3].

In the time-of-flight (TOF) or pulse-delay method, the chromatic dispersion is derived from the relative temporal group delay experienced by various wavelengths during their propagation through a fiber length. The delay is measured by detecting, recording and processing the differences in propagation time experienced by pulses at various wavelengths. Dispersion can then be obtained for a fixed wavelength or over a desired range. The optical source must be stable in lasing wavelength and intensity over

enough time to complete the measurements. The modulation frequency must also be set such that there is enough time resolution to make the measurements. In this way, a reference channel is not necessary [4.1, 4.3]. The technique requires that short temporal pulses at multiple known wavelengths be simultaneously launched into the test fiber. A photodetector and sampling oscilloscope captures the output signal and the relative time delay between the consecutive pulses is recorded for each wavelength pulse. The group delay as a function of wavelength can then be obtained by using a least mean square fitting technique, and the dispersion can be calculated by differentiating this curve with respect to wavelength. However, the TOF approach is limited to relatively long lengths of test fiber (several km's) because the delays between the consecutive pulses must be distinguishable on a sampling oscilloscope, such as the communications signal analyzer (CSA), requiring a certain amount of cumulative chromatic dispersion [4.3]. Previous experiments have found that the measurements are possible for lengths of ten's of kilometers of single-mode fiber (SMF), when the temporal separation between the pulses is at least twice the full width half maximum (FWHM) of the input pulse [4.1, 4.3].

The TOF measurement method is faster than the phase-shift technique since there is no need for wavelength scanning. It is hence an interesting application for the measurement of dispersion in already-deployed fiber links. Many TOF implementations have indeed been proposed in the recent past. Examples include the use of Raman laser sources [4.5], superluminescent diodes [4.6], or EDF lasers filtered with fiber Bragg gratings [4.1]. The principle causes which degrade the accuracy of the measurements are related to the stability of the input signals and hence to the input optical source used. The above-mentioned approaches suffered from timing jitter and optical triggering instabilities in the case of Raman sources, low power efficiencies in the case of superluminescent diodes filtered with a set of spectrally separated FBGs, or cross-gain saturation effects and flatness issues in the case of an EDF laser with a FBG array filter. They all required additional expensive equipment as a method to compensate their respective problems [4.1]. For example, the low efficiency of the superluminescent diode source needed to be compensated for by the use of very sensitive photon-counting detectors cooled to 220K [4.6]. In the last case, the EDF laser must suppress the cross-gain saturation effect with the use of a frequency shifter placed inside the laser ring

cavity, as shown in figure 4-1. The individual reflectivity of each FBG in the array filter necessary to select the laser lines must also be altered to have the best gain flatness. This alteration changed the laser feedback, and thus variable attenuators were needed to very precisely control the cavity loss. Even so, the flatness was limited to 6dB, although the laser could emit up to 17 lasing lines spaced by 2.2nm, with a signal to noise ratio of 45dB, and average output powers of -12dBm [4.1]. The TOF measurements obtained in this research were nonetheless very precise, although the underlying source complexity and the lack of wavelength spacing tunability may become somewhat of an issue for future applications.

A simpler source design would be welcomed for the TOF method to be made more commercially available. As such, we propose the use of our tunable multi-wavelength SFL to perform chromatic dispersion TOF measurements, and carefully evaluate our results.

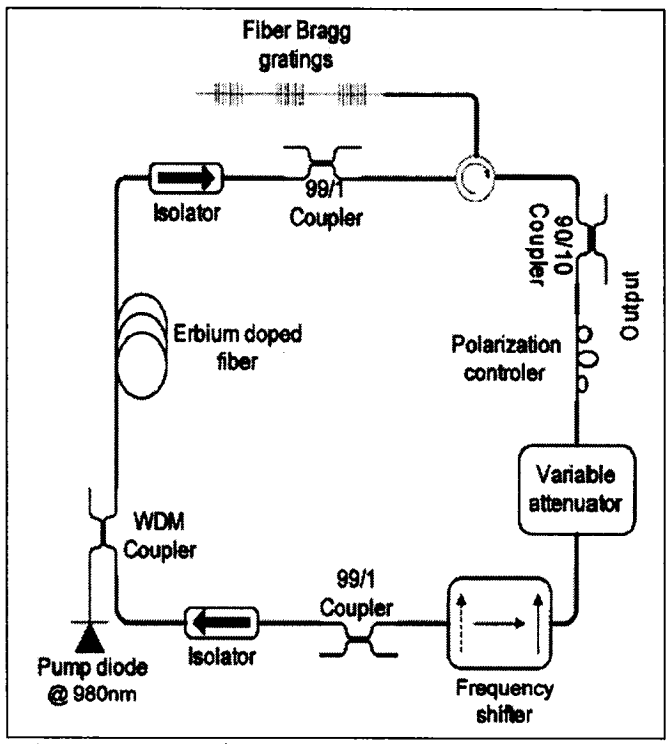

Figure 4- 1: EDF laser proposed by Larochelle et al. [4.1].

4.2 Time-of-Flight Measurement Laboratory Setup and Data Analysis Methods

Figure 4-2 shows the experimental setup used to obtain the TOF measurements using the proposed SFL (refer to figure 3.12 with the VOA removed). The laser output is modulated using a Mach-Zehnder electro-optic modulator (JDS Uniphase 10024291) driven by a pulse pattern generator (Anritsu MP1763B) and biased with a DC voltage set between 3.5V and 4.5V. The square pulses generated had a rise and fall time of approximately 30ps from the 10% to the 90% maximum amplitude level, giving a pulse full width half maximum (FWHM) of 110ps, with total powers averaging around 138.7uW for 3.2nm wavelength spacing, and 124.6uW for 1.6nm wavelength spacing. The input SOA bias current of the SFL was set at 196mA.

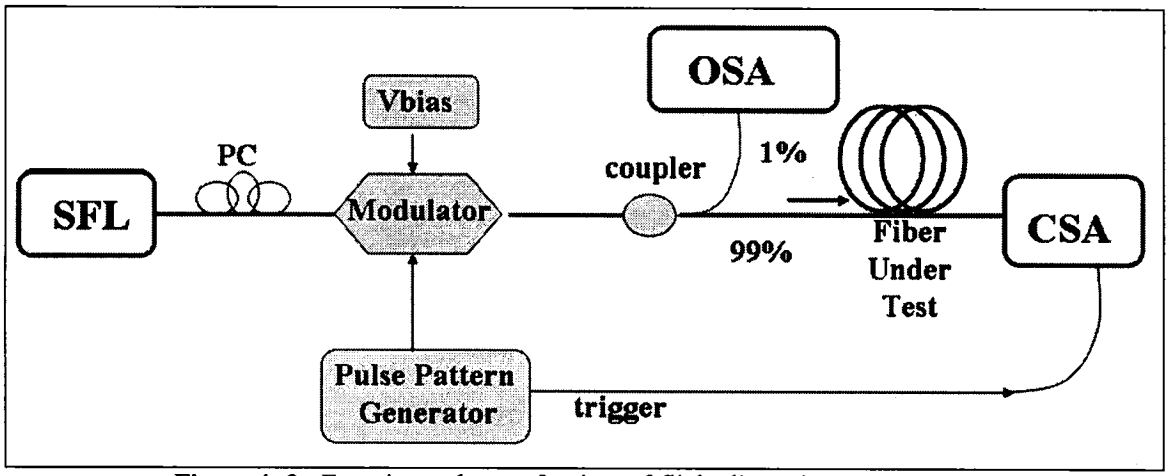

Figure 4- 2: Experimental setup for time-of-flight dispersion measurements

Increasing the number of bits encoded by the pulse generator, with more zeros after the initial one, decreased the repetition rate to a smaller value appropriate for making accurate time delay measurements. Thus 132 bits offered experimentally about 11ns between input pulses, or a repetition rate of 90.91MHz. The corresponding period is appropriate for measuring dispersion-length products (DL) smaller than 687.5ps/nm in the 3.2nm wavelength spacing mode (with a maximum of 6 peaks and 2.2ns time delay between each peak), or 572.92ps/nm in the 1.6nm wavelength spacing mode (with a maximum of 13 peaks and 0.92ns time delay between each peak; or 38km and 32km of SMF respectively). Larger DL products may also be measured by simply further decreasing the repetition rate. The polarization controller optimizes the modulator

throughput and extinction ratio. A 1% power tap is also used in order to monitor the SFL's lasing wavelengths with an OSA. Finally, the pulses are launched into the fiber under test and the transmitted signal is measured with a 20GHz bandwidth optical sampling module (Tektronix 80C01) and CSA. For test fibers longer than 7km, the transmitted signals are first amplified using an EDFA (INO) with a percent pump lower than 15%.

Various lengths of single-mode fiber (SMF) were tested (samples A, B, C and D with increasing lengths), along with a dispersion compensating module comprising about 6.9km of dispersion compensating fiber (DCF) (sample E). As an example, figure 4-3 presents the temporal traces obtained for samples B and E, using both wavelength spacings available from the SFL; i.e. 3.2nm and 1.6nm. These measurements were obtained by averaging the detected signal 500 times.

After propagating through a length of fiber, the pulses at the different wavelengths are separated in time and it is thus possible to measure the relative time delay between neighboring peaks. For the DCF module, the order in which the pulses arrive in time is reversed, and the corresponding delays are thus paired accordingly with the reversed lasing wavelengths. It is also important to note that several measurement procedures were taken for precision purposes. First, the delay between two consecutive peaks was measured from the CSA by zooming in the appropriate area with proper time resolution. Since the input pulse is square shaped, the exact location of each delayed peak was determined by taking the center point between the rising and falling edges. Initially, each recording was done simultaneously with the OSA input spectrum reading. This was done in order to reduce the effects of the anticipated input signal instabilities, but these were not the main cause of errors, as it will be made clear later on, and such a procedure was proven to be unnecessary.

Once the group delay between the consecutive peaks is collected, there are two possible ways to analyze the data. The ITU has made a series of recommendations for the use of different formulas to calculate the chromatic dispersion from any experimental data, for specific types of fibers operating in different wavelength regions. These recommendations were thus taken into consideration. The two analysis methods employed were named "Group-Delay" (GD) analysis, as it fits the group-delay with

respect to wavelength profile according to the ITU-recommendations, and the "Mid-Wave" (MW) analysis, a similar but faster and simpler version of the first.

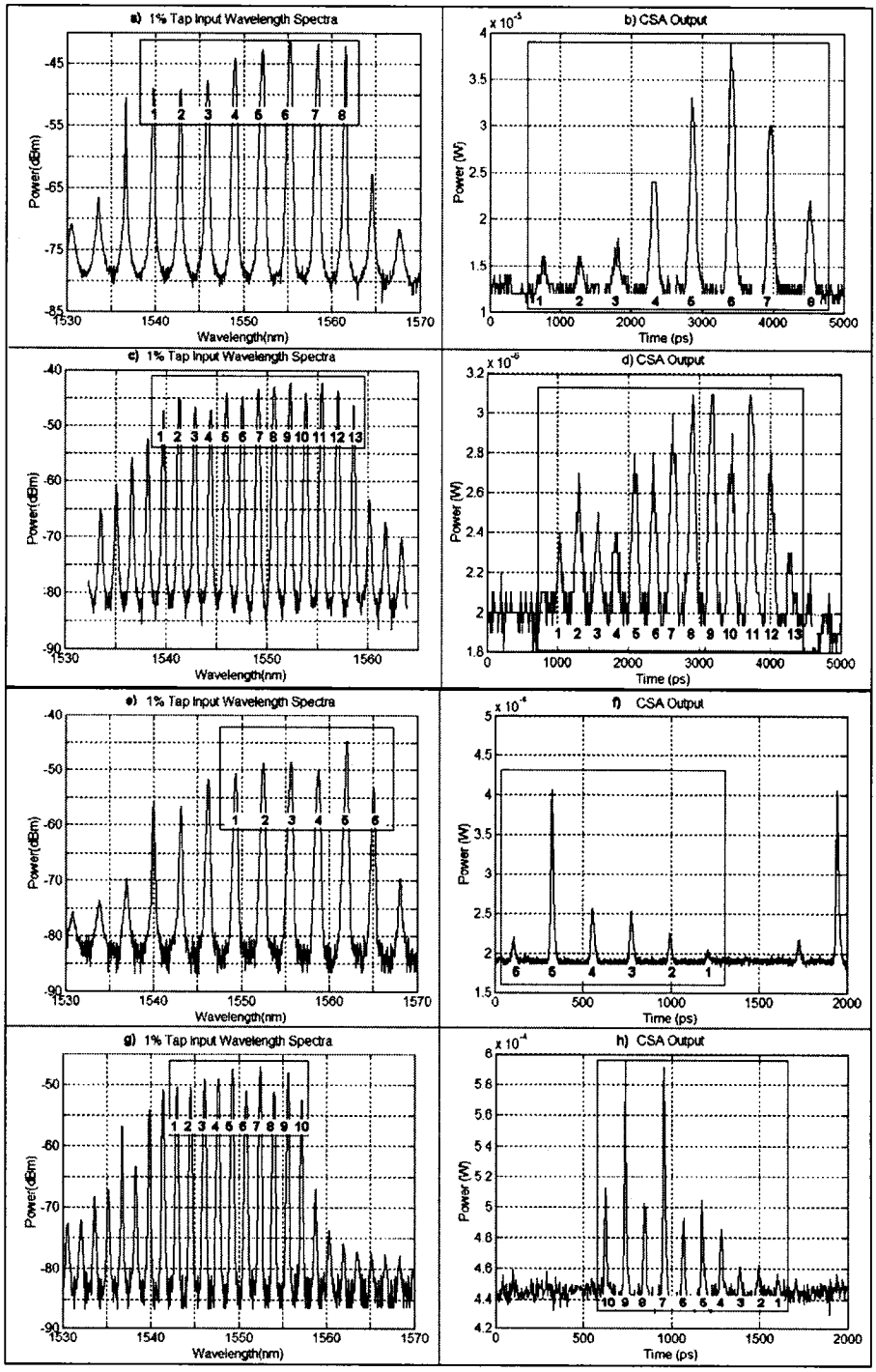

Figure 4- 3: TOF measurements for sample B: (a) and (c) are the input spectra for both wavelength spacing, (b) and (d) are the corresponding CSA output after circulating through sample B test fiber. TOF measurements for sample E: (e) and (g) are the input spectra for both wavelength spacings, (f) and (h) are the corresponding CSA output after circulating through the DCF test fiber. The boxes within each graph identify the relevant lasing modes and time delayed pulses, all numbered to their corresponding peak.

In the GD method, the measured group delay occurring from the first pulse to each of the subsequent ones is plotted against its corresponding lasing wavelength. For non-dispersion-shifted single-mode fibers operating in the 1500-1600nm range (Recommendation G.653) [4.3], the ITU standards recommend fitting the measured group delay per unit length to a quadratic expression, which can then be expressed in terms of τ_o, the relative delay minimum at the zero-dispersion wavelength λ_o, and S_o, the value of the dispersion slope $S(\lambda)$ at λ_o [4.3]:

$$\tau_g = \tau_o + (S_o/2)(\lambda-\lambda_o)^2 \text{ [ps/km]} \quad (23)$$

The dispersion slope $S(\lambda)$ follows the relation:

$$S(\lambda) = dD(\lambda)/d\lambda \text{ [ps/(nm}^2\text{-km)]} \quad (24)$$

where the chromatic dispersion $D(\lambda)$ is obtained by differentiating τ_g with respect to λ, and may be expressed in a linear fashion using the dispersion slope according to the equation below [4.3]:

$$D(\lambda) = d\tau_g/d\lambda = (\lambda-\lambda_o)S_o \text{ [ps/(nm-km)]} \quad (25)$$

In the MW method, the measured group delay occurring between each two consecutive peaks is divided by the wavelength separation occurring between those two same peaks. These values are then plotted against the wavelength located mid-way between those two lasing wavelengths, and the data points are fitted to a linear approximation using a "best-fit" mathematical algorithm (refer to Appendix B for the corresponding Matlab codes). This method essentially gives an alternate way of performing the group-delay curve fitting and differentiation. Such an analysis also provides for a straightforward way to obtain the desired chromatic dispersion values.

For both analysis methods, if the length of fiber being tested is not accurately known, the dispersion-length (DL) product as a function of wavelength can be obtained, and hence represents a more accurate measure that is appropriate for the comparisons presented in the next sections. The DL product profiles are lines characterized by a certain slope (s), given in ps/nm^2, and a certain offset (os), in ps/nm. The DL product as a function of wavelength thus fits the corresponding linear equation:

$$DL(\lambda) = s\lambda + os \quad (26)$$

For each sample, both data sets provided by the two SFL input wavelength spacings were first analyzed individually. The pair of slopes and offsets were then averaged to get the final "Averaged" DL curve in the case of the GD analysis method. In the MW analysis method, however, it was possible to assemble the two data sets together and obtain an "Overall" DL best-fit curve.

The following section reveals all the chromatic dispersion-length profiles experimentally obtained using the TOF technique and both data analysis methods.

4.3 Experimental TOF Measurement Results

Figures 4-4 and 4-5, together with Table 4-1, present the measurement results for all samples A through E, either analyzed using the GD or the MW techniques respectively. Samples A to D were measured using a 20GHz bandwidth optical sampling module, while sample E was done with a 30GHz module. We see a close agreement between the two GD and the MW analysis results. Section 4.4 will further determine which is closest to the phase-shift results, and thus if one analysis method is preferred over the other.

The differences between the measures taken with either the 1.6nm or the 3.2nm input wavelength spacings are most probably caused by the added dispersion and noise of the EDFA. In sample B and E, for example, the EDFA was used only for the 1.6nm input spacing due to this setting's lower input peak powers. This effect is minimized when both measurements are taken with the use of the EDFA, as is the case for samples C and D only. The added dispersion of the EDFA was later measured using the phase-shift technique, and presented a very small amount. It was thus concluded that the major source of error is caused by the added amplifier noise more than by its additional dispersion.

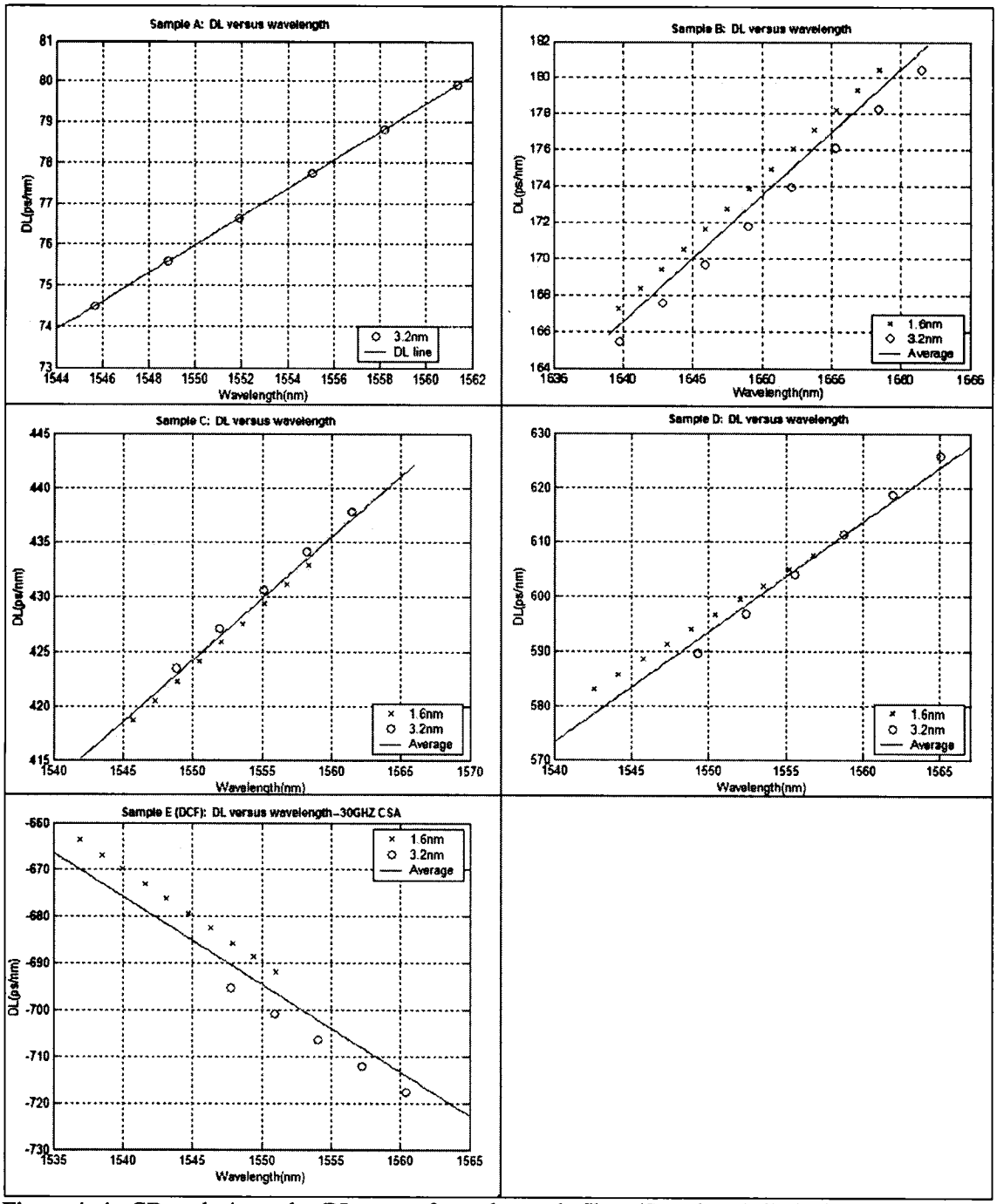

Figure 4- 4: GD analysis results: DL curves for each sample fiber. (Sample A is limited to 3.2nm spacing only).

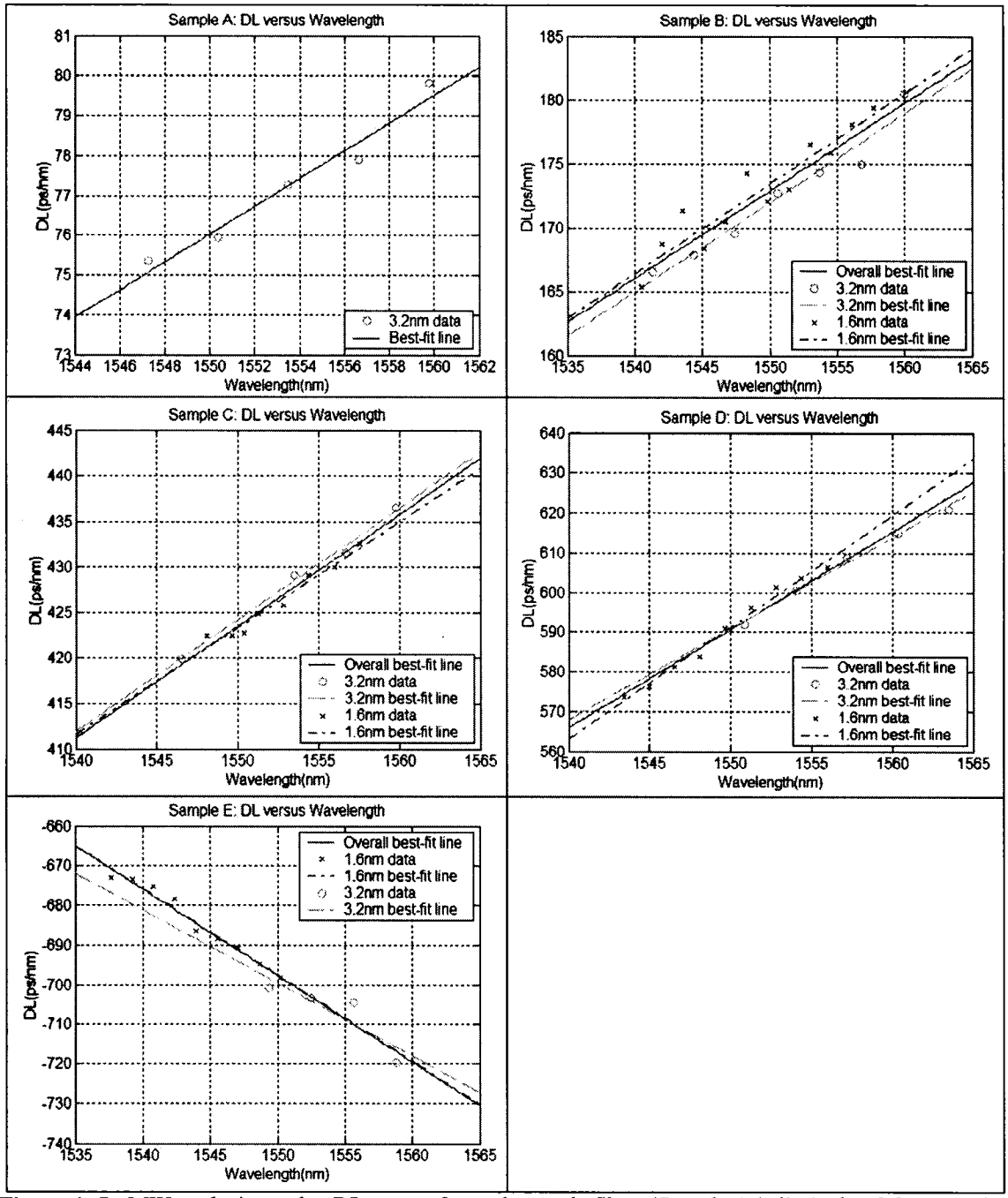

Figure 4- 5: MW analysis results: DL curves for each sample fiber. (Sample A is limited to 3.2nm spacing only).

DL curves for each test fiber (GD analysis)	Slopes (ps/nm^2)	Offsets (ps/nm)
Sample A: 3.2nm wavelength spacing	0.35	-459.4
Sample B: Average	0.69	-902.3
3.2nm spacing	0.70	-913.6
1.6nm spacing	0.69	-891.0
Sample C: Average	1.12	-1,318.5
3.2nm spacing	1.13	-1,326.8
1.6nm spacing	1.12	-1,310.3
Sample D: Average	2.01	-2,528.3
3.2nm spacing	2.31	-2,987.5
1.6nm spacing	1.72	-2,069.2
Sample E--DCF: Average	-1.88	2,223.7
3.2nm spacing	-1.77	2,045.7
1.6nm spacing	-1.99	2,401.6
DL curves for each test fiber (MW analysis)	**Slopes (ps/nm^2)**	**Offsets (ps/nm)**
Sample A: 3.2nm wavelength spacing	0.35	-464.6
Sample B: Overall	0.69	-890.9
3.2nm spacing	0.70	-911.5
1.6nm spacing	0.70	-919.0
Sample C: Overall	1.23	-1,483.1
3.2nm spacing	1.41	-1,755.4
1.6nm spacing	1.12	-1,313.0
Sample D: Overall	2.47	-3,240.0
3.2nm spacing	2.30	-2,980.0
1.6nm spacing	2.82	-3,780.0
Sample E--DCF: Overall	-2.19	2,691.8
3.2nm spacing	-1.85	2,161.8
1.6nm spacing	-2.18	2,682.9

Table 4- 1: MW and GD analysis results: Slopes and offsets of the corresponding DL curves shown in figures 4-4 and 4-5.

4.4 Experimental Phase-Shift Measurement Results

In order to verify the accuracy of the previous TOF measurements, the same samples were processed using a regular phase-shift technique to measure their respective DL versus wavelength profiles.

For such purpose, a lightwave component analyzer (Agilent 8703B 4114A00105) measured the phase difference between a reference CW source signal modulated at 500MHz, while a Labview program controlled the CW source's lasing wavelength to record the resulting group delay at each wavelength point. The scanning was performed over a wavelength range similar to the lasing wavelengths of the tunable multi-wavelength SFL (i.e. from 1540nm to 1570nm in 0.2nm increments).

The data analysis follows that of the GD TOF analysis previously explained in section 3.2 since $\tau_g(\lambda)$, the group delay as a function of wavelength, can be recovered from the phase shift according to the following relation [4.2]:

$$\phi(\lambda)=2\pi f\tau_g(\lambda) \qquad (27)$$

where $\phi(\lambda)$ is the phase difference measured at each wavelength step and f is the modulation frequency of the input signal employed.

The following table 4-2 gives the final phase-shift DL characteristics for each sample.

Phase-Shift Measurements	Slopes (ps/nm^2)	Offsets (ps/nm)
Sample A	0.27	-340.3
Sample B	0.59	-736.8
Sample C	1.17	-1,396.8
Sample D	1.89	-2,338.0
Sample E: DCF	-2.12	2,605.8

Table 4- 2: Phase-Shift measurement DL results: slopes and offsets.

4.5 Comparison between TOF and Phase-shift Results

Figure 4-6 presents the DL curves obtained using both the phase-shift and the TOF techniques, together with the percent differences at each wavelength (dotted centered lines). The dashed lines are the TOF measures analyzed using the GD method, while the dash-dotted lines are those evaluated using the MW method.

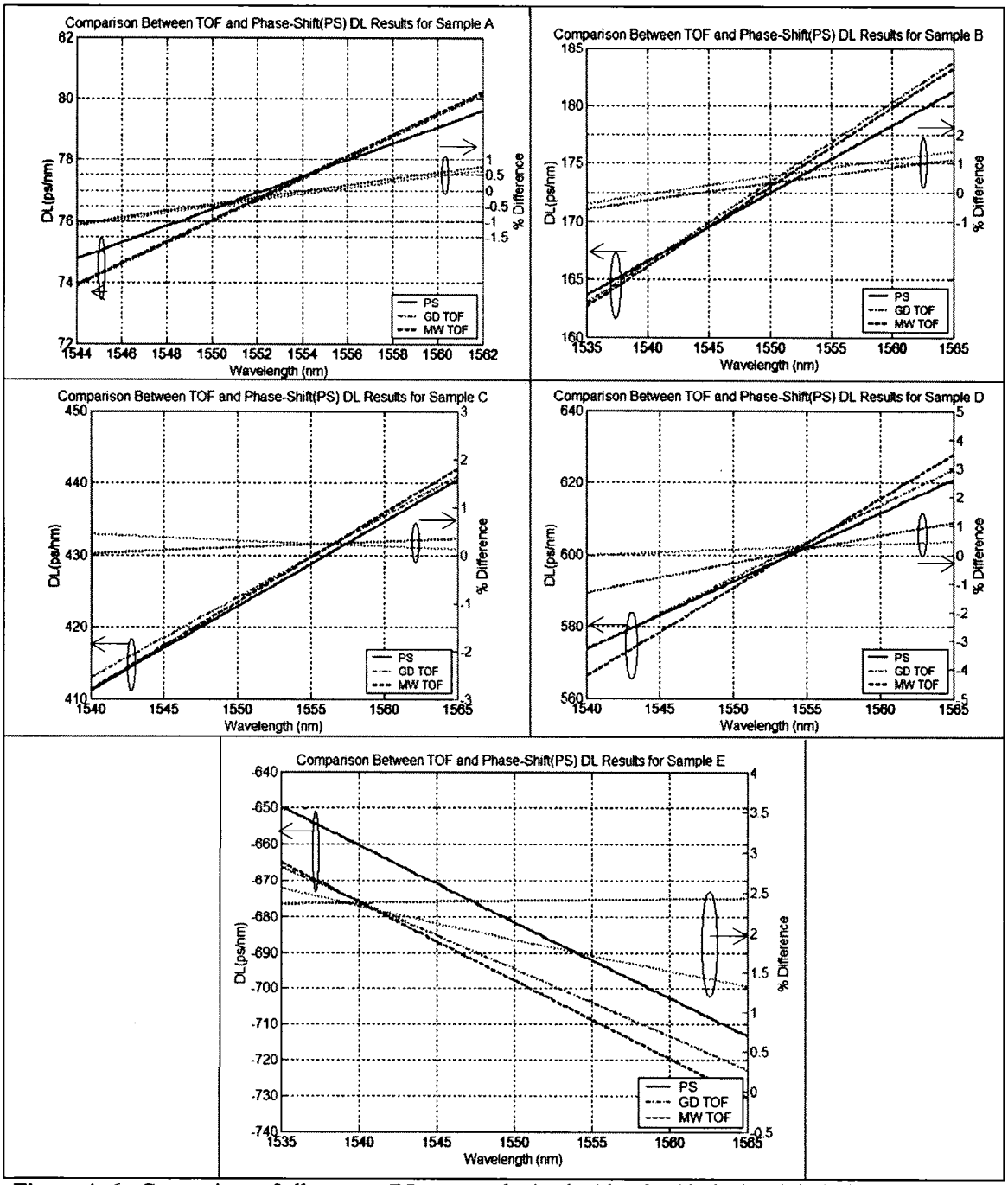

Figure 4- 6: Comparison of all average DL curves obtained with TOF (dashed and dash-dotted lines) and Phase-Shift technique (full lines) over their respective SFL lasing wavelength range. The dotted lines indicate the percentage difference relative to the phase-shift results taken a specific wavelength (axis on the right-hand side of each graphs).

The GD analysis has percent differences between the measurements within -0.73% and 1.13% for samples A through D, except for sample E, the DCF module. The MW analysis presents percent differences between -1.25% and 1.12% for samples A

through D as well. Sample E obtains percent errors between 11.3% and 2.6%. Finally, these phase-shift measurements did not account for the additional dispersion of the EDFA that was used for the TOF measurements. This added dispersion was later measured to be quite small, and it is thus assumed that the added noise of the EDFA increases the measurement errors. However, a slight reduction in percent differences of about 0.1% to 0.2% is calculated when taking into account this added amplifier dispersion.

It is believed that the accuracy of the TOF measurements are limited by the bandwidth of the optical sampling module, the use of square-shaped pulses, and by the noise induced from the amplifier.

First, averaging the results from 4 different measurements, each averaged in turn using measurements from both the input SFL's wavelength spacings, greatly improves on the precision. This was done using sample B, for which the averaged DL slope obtained via averaging shows a reduction of 10.0% (GD analysis) and 13.2% (MW analysis) in percent differences of the DL slopes (with respect to the DL slope measured with the phase-shift technique), compared to that of the non-averaged measurements. In this case, the percent differences in the DL curves calculated at each wavelength is within 0.55% for the GD analysis, and between -0.25% and 0.1% for the MW analysis (refer to figure 4-7 and table 4-3). The maximum slope deviation occurring within these repeated measurements was calculated to be +/-0.09ps/nm^2, with an average slope repetition error (from the average value) of +/- 14.7%. The MW analysis method gave similar maximum slope deviations within the repeated measurements: +/- 0.08ps/nm^2, for an average repetition error of +/-12.6%.

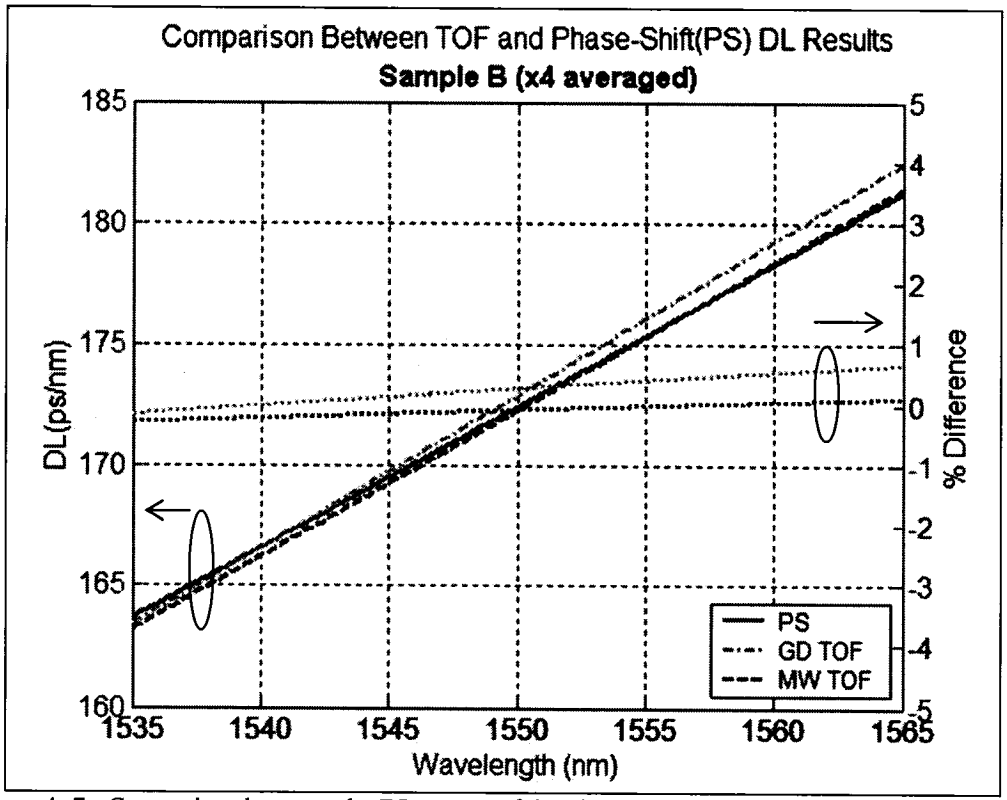

Figure 4- 7: Comparison between the DL curves of the phase-shift method and the TOF obtained by averaging over 4 TOF measurements.

Measurement Number	Slopes (ps/nm^2)	Offsets (ps/nm)
MW analysis results:		
1	0.58	-729.3
2	0.54	-669.7
3	0.61	-778.3
4	0.70	-907.3
Average	0.61	-771.2
GD analysis results:		
1	0.62	-786.4
2	0.54	-671.7
3	0.65	-828.1
4	0.73	-959.7
Average	0.63	-811.5

Table 4- 3: Sample B averaging results: slopes and offsets of the independent DL curve measurements.

Second, since the results for samples A to D were obtained with an optical sampling module of 20GHz, the possibility of using a module with a larger bandwidth (30 GHz), or a better impulse response, could be used to improve further upon the temporal measurements. For example, figure 4-8 and table 4-4 present the results and comparisons

for sample B using a 30GHz bandwidth optical sampling module. As anticipated, lower percent differences relative to the phase-shift measurements are obtained: for the GD analysis, there is a decrease from 18.31% to 2.78% difference between the averaged TOF slopes (both SFL input wavelength spacings) and the phase-shift slopes (refer to table 4-5). In the case of the MW analysis, the same sample shows a decrease from 17.0% to 0.1% difference. A 0.4% difference in the slopes is even obtained for the 1.6nm input spacing measurement analyzed using the GD method, the lowest yet obtained from one single measurement.

Sample B using 30GHz CSA	Slopes (ps/nm^2)	Offsets (ps/nm)
MW analysis: Overall	0.59	-736.3
3.2nm spacing	0.73	-963.8
1.6nm spacing	0.63	-806.8
GD analysis: Average	0.60	-760.4
3.2nm spacing	0.62	-782.2
1.6nm spacing	0.59	-738.7

Table 4- 4: Sample B results using 30GHz CSA.

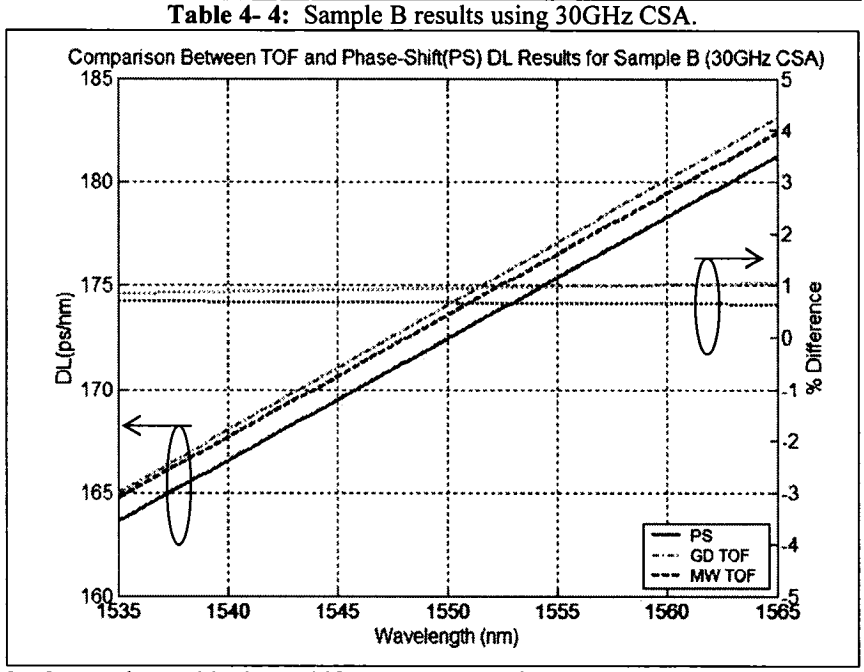

Figure 4- 8: Comparison with phase-shift measurements for the results obtained for Sample B using 30GHz bandwidth optical sampling module (Average GD and Overall MW measures). Dotted lines indicate respective percent differences relative to phase-shift results. (Dashed lines and dash-dotted lines are TOF, full line is from phase-shift technique).

It is also important to note that the possibility of making the measurements using both the 1.6nm and the 3.2nm wavelength spacing of the input SFL increases the flexibility of the process by providing for generally better accuracy of the results, as the

wavelength bandwidth is increased. Table 4-5 gives an idea of this advantage by listing the percent differences (again relative to phase-shift measures) between the resulting DL slopes from each independent and averaged or overall TOF readings, in both the 1.6nm and the 3.2nm spacing modes, and for both analysis methods.

	Percent difference between the TOF DL slopes relative to those from the phase-shift method (MW analysis)	Percent difference between the TOF DL slopes relative to those from the phase-shift method (GD analysis)
Sample A: 3.2nm wavelength spacing	29.8%	28.5%
Sample B: Both spacings	17.0%	18.3%
3.2nm spacing	19.3 %	19.7%
1.6nm spacing	20.3%	17.0%
Sample B: Averaged over 4 measurements (using both spacings)	3.8% (a 13.2% decrease)	8.3% (a 10% decrease)
Sample B: 30GHz CSA Both spacings	0.1% (a 16.9% decrease)	2.8% (a 15.5% decrease)
3.2nm spacing	25.0%	5.2
1.6nm spacing	7.9%	0.4
Sample C: Both spacings	4.8%	4.2%
3.2nm spacing	19.7%	3.7%
1.6nm spacing	4.6%	4.7%
Sample D: Both spacings	30.7%	6.5%
3.2nm spacing	21.9%	22.1%
1.6nm spacing	49.1%	9.1%
Sample E--DCF: all spacings	3.1%	11.2%
3.2nm spacing	13.0%	16.5%
1.6nm spacing	2.8%	6.0%

Table 4- 5: Percent differences between all DL slopes obtained from TOF measures relative to those obtained from phase-shift measures.

More accurate chromatic dispersion measurements based on the TOF technique are thus possible by first using an optical sampling module with a larger bandwidth and, then, by averaging over multiple measurements. Furthermore, both data analysis methods remain in good agreement with phase-shift measurements. It is also expected that better accuracy may be obtained by using shorter Gaussian pulses rather than the square-shaped pulses used here. This will help in determining the exact location of each peak, even in the presence of added noise due to the use of an amplifier in the TOF measurement setup.

4.6 Discussion

There exists certain limitations to the TOF technique, and these must be fully understood. First, the TOF method cannot be used to measure dispersion in fiber components, nor in C-band dispersion shifted fiber (DSF), as the order in which the pulses arrive in time cannot be predicted. Secondly, there is a minimum length of fiber, or DL product, which can be accurately tested. As cited in many sources and articles on TOF measurements [4.1,4.3-4], experiments have shown that a time delay equal to twice the FWHM of the input pulse is necessary in order to be able to distinguish the individual delayed pulses. For SMF with a dispersion of 17ps/(nm·km), this corresponds to a minimum test length of 4.04km for a wavelength spacing of 3.2nm. In the case where the multi-wavelength source has a wavelength spacing of 1.6nm, the lower limit increases to 8.09km. This explains why sample A was only measured using the 3.2nm setting; its length was later determined to be around 4.3km. The flexibility of our SFL also permits not only more precision for DL products greater than 138ps/nm, but also the possibility to increase the wavelength spacing to be able to measure smaller DL products not possible with the 1.6nm spacing mode. For very large amounts of dispersion, the period of the input pulse may be decreased in order to be able to eliminate the pulse overlapping that would occur for faster pulse periods. For even larger dispersions, there is always the possibility to reduce the amount of accumulated time delay by incorporating a DCF fiber length with a precisely known dispersion amount and profile that is the inverse (opposite sign) of the fiber under test, as proposed in reference [4.8]. In this way, a very large dispersion amount may be made smaller by the DCF, and the measure may be taken over a faster input pulse period without any problem.

The detector and sampling oscilloscope are the most limiting aspect of the measurement precision since these induce a resolution limit. One solution proposed by de Matos et al. in 2003, was to use an autocorrelator to measure the time delay between two lasing lines more precisely. The measurements were thus performed over a very small wavelength range, but these were very precise. The underlying measurement complexity, however, can become an issue, while the required scanning time may be long, as only two peaks can be measured at a time. The autocorrelator itself also presented systematic errors that needed to be carefully compensated for [4.8].

Finally, the method we propose is a fast, simple, low-cost solution for measuring dispersion in long fiber networks. The TOF chromatic dispersion measurement technique demonstrated using our SFL will be made even more accurate in the very near future, as sampling oscilloscopes and optical signal analyzers with greater resolutions are arriving.

4.7 Conclusion

We have successfully demonstrated the measurement of chromatic dispersion in fiber lengths using the TOF method with our newly developed tunable multi-wavelength SFL. The measurements were compared to the phase-shift technique and these show good agreement. The limitations and errors encountered can be improved upon through minor adjustments; such as using optical sampling modules with larger bandwidths, shorter Gaussian shaped optical input pulses, averaging over several measurements (ten or more), and using computer-controlled data acquisition. Nevertheless, this new measurement system offers the advantage of being much quicker and less complex, as no reference signal or wavelength scanning is needed. As for the multi-wavelength source's induced limitations, it is understood that an improvement on stability, output power, as well as smaller linewidths and greater spectrum flatness would further increase the accuracy of the TOF results here presented. The idea, however, was to offer a reliable, yet simple and low-cost application, that could measure the dispersion in long, already deployed fiber links. In such a case, the trigger signal sent to the optical sampling module and digital oscilloscope may then be replaced by using a slow detector in which the same output signal is fed. We have thus proposed a rapid and convenient, commercially applicable method of evaluating chromatic dispersion.

4.8 References

4.1 J.-N. Maran, Radan Slavik, Sophie LaRochelle, and Miroslav Karasek, "Chromatic dispersion measurement using a multiwavelength frequency-shifted feedback fiber laser," *IEEE Transactions on Instrumentation and Measurement*, vol. 53, no. 1, pp. 67-71, February 2004.

4.2 G. Kaiser, *Optical Fiber Communications*, 3rd Edition. Boston: McGraw-Hill (2000)

4.3 ITU: International Telecommunications Union, Recommendation G.650.

4.4 M. J. Heckert, "Development of chromatic dispersion measurement on multimode fiber using relative time of flight measurement technique," *IEEE Photonics Technology Letters,* vol. 4, no. 2, pp. 198-200, February 1992.

4.5 L.G. Cohen, "Comparison of single mode fiber dispersion measurement techniques," *J. Lightwave Technology*, vol. LT-3, no. 5, pp. 958-966, October 1985.

4.6 H. Riedmatten, M.Wegmuller, H.Zbinden, and N.Gisin, "Group-delay analysis of chirped fiber Bragg gratings using photon counting," *IEEE Photonics Technology Letters, vol.13,* no.6, pp. 615-617, June 2001.

4.7 C.J.S. de Matos, J.R. Taylor, "Use of an electroabsorption modulator and an autocorrelator for fibre chromatic dispersion measurement at 1550nm," *Optics Communications,* no. 226, pp. 221-225, 2003.

V. Second Application: Tunable and Reconfigurable Microwave Filter Design

5.1 Motivation

The last 25 years have seen the arrival of a new discipline known as Microwave Photonics. During that time, much active research has been completed on the exploitation of the advantageous properties of optical devices for the generation, transport, processing, and detection of microwave as well as millimeter-wave signals. The main interest resides in the possibility of realizing flexible microwave and radio-frequency (RF) filters free from the bandwidth constraints seen using traditional RF circuit approaches [5.1]. Electrical RF circuits are designed for a specific spectral band and thus suffer from very poor flexibility. When discrete-time signal processing must be done over the RF signal domain, a phenomenon known as the electronic bottleneck also arises and the sampling speed of the processor must thus be made faster. Finally, electromagnetic interference and frequency dependent losses are important sources of degradation occurring with RF domain signal processing [5.1]. Discrete-time optical processing of microwave signals (DOPMS) offers the possibility of overcoming these limitations, as the signal processing tasks are done using optical carriers directly in the optical domain. Figure 5-1 compares the traditional with the photonic approach. In the latter, an RF signal directly or externally modulates a laser, and the composite signal is then processed by the photonic circuit. A final receiver performs the final optical to RF conversion, after the processing unit has first sampled the composite signal in the time domain, weighing and combining them using optical delay lines. The advantages of such a novel approach are considerable. First and foremost, photonic microwave filters offer low frequency-independent loss, very high time-bandwidth products, and wide dynamic ranges. They are also potentially small in size, much lighter and immune to electromagnetic interference, offer very high-speed sampling frequencies (100GHz compared to 10GHz with available electronic technology), are much more flexible, and are finally compatible with WDM techniques [5.1-3].

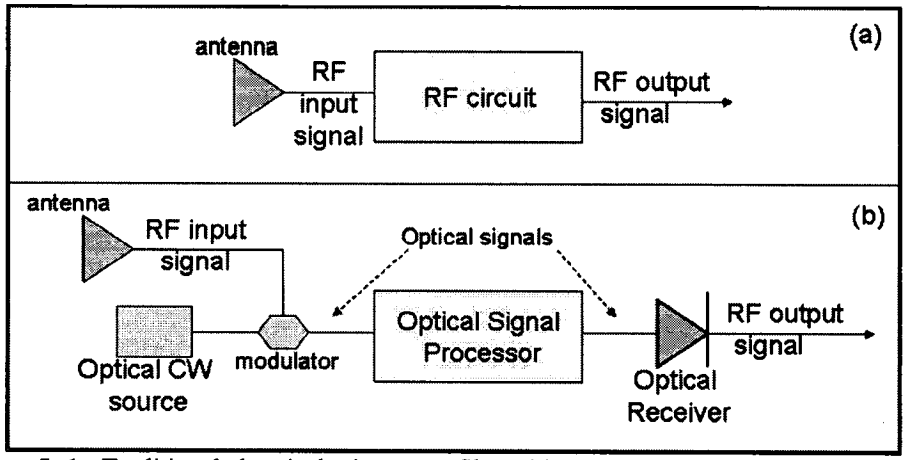

Figure 5- 1: Traditional electrical microwave filters (a) versus new photonic filters (b) [5.1].

Photonic technology is thus very attractive for any microwave and millimeter-wave engineering application. DOPMS is of interest for radio over fiber systems, needing both channel rejection and selection applications, and in radio-astronomy as well, where strong manmade interfering signals must be removed. Noise suppression and channel interference mitigation performed in the font-end stage, after the receiving antenna of a base station, as well as the RF band selection later required, can all be done in the optical domain, where the filter bandpass area can be made tunable over a very large frequency band (a few MHz to several tens of GHz) [5.1]. Other applications include satellite communication systems, benefiting from lightweight solutions. All applications suffering from the electronic bottleneck, such as moving target identification radar systems, also benefit from DOPMS [5.4]. In this case, the use of a photonic filter to remove unwanted noise before frequency downconversion to baseband, and analog to digital conversion (ADC), may be employed instead of a digital notch filter placed after such conversions. This would decrease the required ADC resolution. Finally, broadband photonic delay lines offer an interesting approach for the implementation of phased-array antennas as well as very high speed signal correlators [5.1].

Research contributions within the field started in 1976, when Wilner and Van de Heuvel noted that optical fibers were ideal candidates for broadband delay lines because of their low loss and high modulation bandwidths [5.1]. Extensive work has then been conducted in the 80's and 90's at the University of Stanford, but the technology status at the time imposed serious limitations like loss and lack of filter reconfiguration. The

introduction of optical amplifiers and other relevant optical components in the 80's has greatly helped in developing better microwave processing solutions. The recent availability of components like FBGs and AWGs, for example, has moreover opened the possibility of creating fully reconfigurable, tunable, and relatively low-cost DOPMS modules [5.1]. The last ten years has thus seen the implementation of flexible photonic microwave filters with relatively large tuning ranges of around several tens of GHz, with optical sidelobe suppression ratios of at least 30dB, reconfiguration possibilities, compactness, and low insertion loss [5.2]; a few of which are described in section 5.3. This chapter aims at demonstrating the tunability of such a filter using the proposed SFL. First, section 5.2 covers the operation principle of the proposed filter implementation. After the filtering examples of section 5.3, section 5.4 explains the simulations performed prior to data collection, while section 5.5 presents and compares the results to the simulations. Finally, section 5.6 further discusses the measurements and limitations, while section 5.7 makes some final conclusions.

5.2 Principle of Operation

The general optical processor schematic shown earlier in figure 5-1 may be implemented in several ways. The CW optical source may actually be constructed of many sources, or from a single multi-wavelength source. The optical processing unit may provide for spectrum splitting components and a means to apodize the created filter tap powers if not initially done by the optical source itself, and more importantly, delay lines to implement the time separation between the taps. From discrete-time signal processing theory, a DOPMS transversal, or non-recursive filter, must implement a general transfer function given by [5.1]:

$$H(z^{-1})=\sum_{k=0}^{N} p_k z^{-k} \qquad (28)$$

where z^{-1} is the basic delay between the samples, and p_k are the implemented filter coefficients, and N is the order of the non-recursive part (FIR) filter, or the number of optical taps employed minus one.

The electrical pulse response is derived from the above equation:

$$h(t) = \sum_{k=0}^{N} p_k \delta(t-kT) \tag{29}$$

giving the following output signal once convolved with the input RF signal $s_i(t)$:

$$s_o(t) = \sum_{k=0}^{N} p_k s_i(t-kT) \tag{30}$$

where T is the time delay between each pulse or filter tap. If all the samples or pulses have the same amplitude, the filter is said to be uniform, whereas apodized or windowed filters have taps of different amplitudes. The electrical frequency transfer response H(f) is obtained by Fourier transformation of the above equation:

$$H(f) = \sum_{k=0}^{N} p_k e^{-jkfT} \tag{31}$$

with a frequency period determined by the free spectral range (FSR), which is inversely proportional to the time delay T between neighboring pulses. The Q factor, or filter selectivity, is then given by the ratio between its FSR and the full width half maximum of the resonances. If the number of taps employed to implement a uniform filter is larger than ten, the Q factor can generally be approximated by that same number. Hence, the more optical taps, the better the filter response becomes [5.1].

In order to build a tunable microwave filter, one requires a means to generate the optical taps, the optical delay lines to impose a certain time delay T between the taps, and a way to weigh the taps in power and to recombine those before the receiving end. As such, several implementations have been proposed in the past and will be presented in section 5.3.

The filter can also be operated under coherent or incoherent regimes. Under coherent regime, each optical tap has a deterministic optical phase relationship with the rest of the inputs, and an interference term occurs when the photodetector converts the optical power into electrical current. Generally, this exists only when a single optical source is used. In this case, filters with negative and complex coefficients can be easily implemented, but since the operation of the filter relies on optical interference, any slight environmental change can greatly affect the filter response. Coherent filters are thus very difficult to implement, and the rest of the chapter will thus concentrate on incoherent

filters. In incoherent regime, the optical phase relationship between the filter taps is completely random. The interference is thus lost, no beating occurs at the photodetector, and the filter is quite stable and compact [5.1]. The above relationships are applicable to such incoherently operated filters. Unfortunately, this regime makes the implementation of negative coefficients more difficult, thereby limiting the range of possible transfer functions [5.1], as further detailed in the next section.

Finally, tunability can be achieved by changing the FSR or the time delay T between the taps. This can be done by either varying the spectral distance between the taps via wavelength tuning of one or multiple input sources, or by changing the propagation path length via delay lines. Reconfiguration of the filter occurs when the amplitude of each tap (p_k coefficients) is changed and the filter transfer function is reshaped. As such, many different coefficient apodizations have been experimented; Hanning giving relatively better Q factors than Gaussian windowing, as described in [5.5].

For the case of the specific incoherently operated microwave filter implementation considered in this thesis, the previously developed SFL is used to generate positive coefficient taps or optical carriers. The dispersive media is a simple fiber delay line that has a dispersion versus wavelength profile. An electro-optical modulator is used to modulate the optical carriers in time with an RF signal, and a detector collects the electrical output signal. More precisely, an EDFA compensates for the losses before a lightwave component analyzer (LCA), or a vector network analyzer, records the microwave filter response, as we will see in section 5.5. Filter tunability will be achieved by simply changing the wavelength spacing between the different lasing modes of the SFL, or by varying the length of dispersive fiber. Changing the individual powers of each wavelength peaks at the source, on the other hand, performs filter reconfiguration. For such a filter implementation, where an arbitrary dispersive element is used, together with N individual optical carriers RF modulated with frequency f_{RF}, the following two filter transfer functions are derived: [5.5-7]

AM modulation: $|H_{RF}(f_{RF})|=R\cos(\beta_2 f_{RF}^2/2)|\sum_{K=1}^{N} p_k e^{-j[f_{RF}(k-1)\Delta\tau]}|$ (32)

SSB modulation: $|H_{RF}(f_{RF})|=R|\sum_{K=1}^{N} p_k e^{-j[f_{RF}(k-1)\Delta\tau]}|$ (33)

where R is the detector's responsitivity, f_{RF} is the signal frequency, β_2 is the group delay slope of the dispersive element, and $\Delta\tau = \beta_2\Delta\omega$ is the time delay of the dispersive element, and Δw is the distance in frequency between the SFL's lasing modes. This expression can also be expressed by the dispersion-length product, DL, in ps/nm of the dispersive fiber element multiplied with the wavelength spacing, $\Delta\lambda$, of the SFL. The first term in equation (31) is due to the carrier-suppression effect, where the dispersive nature of the element cancels some signals at specific frequencies. This effect can be suppressed by using single sideband (SSB) modulation instead of amplitude (AM) modulation [5.5, 5.7].

The FSR of the filter will thus be related to the wavelength spacing $\partial\lambda$ between carriers through the following equation [5.5, 5.8]:

$$FSR = 1/(D\Delta\lambda)\ [THz] \quad (34)$$

where D is the dispersion–length product of the dispersive fiber in ps/nm, and $\Delta\lambda$ is the wavelength spacing, in nm, of the input SFL carriers. The quality factor Q is given by:

$$Q = FSR/FWHM \quad (35)$$

which is proportional to the number of carriers and depends on their relative amplitudes [5.9].

5.3 Past Microwave Filter Implementations

Four different approaches can be taken in order to implement an incoherently operated microwave filter, all of which are represented in figure 5-2 [5.1].

From top to bottom of figure 5-2, the first possibility makes use of one single-wavelength source. All the filter taps are thus delayed versions of this source. In this case, however, the coherence between the taps will set a limit to the maximum attainable

filter FSR. To avoid undesired interferences due to source coherence, the time delay between the filter taps must be made much larger than the source's coherence time. Since FSR is inversely proportional to the minimum allowable time delay, there is thus a maximum FSR possible. For small linewidth sources, this effect poses an even smaller maximum FSR limit. Hence, larger linewidth sources, such as low-quality DFB lasers, are preferred due to their smaller coherence time. The second approach makes use of N individual optical sources or single-mode lasers modulated with the same RF input signal. Each source thus implements one single filter tap. There is no coherence in this case and hence the FSR is unlimited. This approach is also interesting since the tap powers and lasing wavelengths can be independently adjusted to provide for the best filter characteristics. The number of tapping elements is however limited to the number of input sources, making this method quite expensive and impractical as the number of taps is increased.

In the third method, a broadband source (BBS) with low coherence time is modulated and generates all the filter coefficients. Since each tap carries all the spectral components present in the BBS, the linewidth can be said to be almost infinite, and there is thus no limit whatsoever on the filter FSR. The fourth approach is quite similar and may be implemented using an incoherent spectrally sliced BBS or a short coherent-time multi-wavelength laser. In this implementation, each tap carries a slice of the whole BBS spectrum or has a certain lasing peak linewidth. If the linewidth of each tap is relatively large, the maximum attainable FSR will not be too limited.

Finally, both the third and fourth approaches will present a filter response with an undesired low-pass envelope effect when joined to a dispersive element necessary to provide for the time delay T between each tap. Since each optical carrier possesses a range of spectral components, the exact time delay T will be affected by not only first, but also second-order dispersion, thereby imposing such a low-pass filtering effect. The fourth option can thus reduce this phenomenon by having carrier linewidths made not too large, but not too small either, so as not to impose a maximum limit on the FSR.

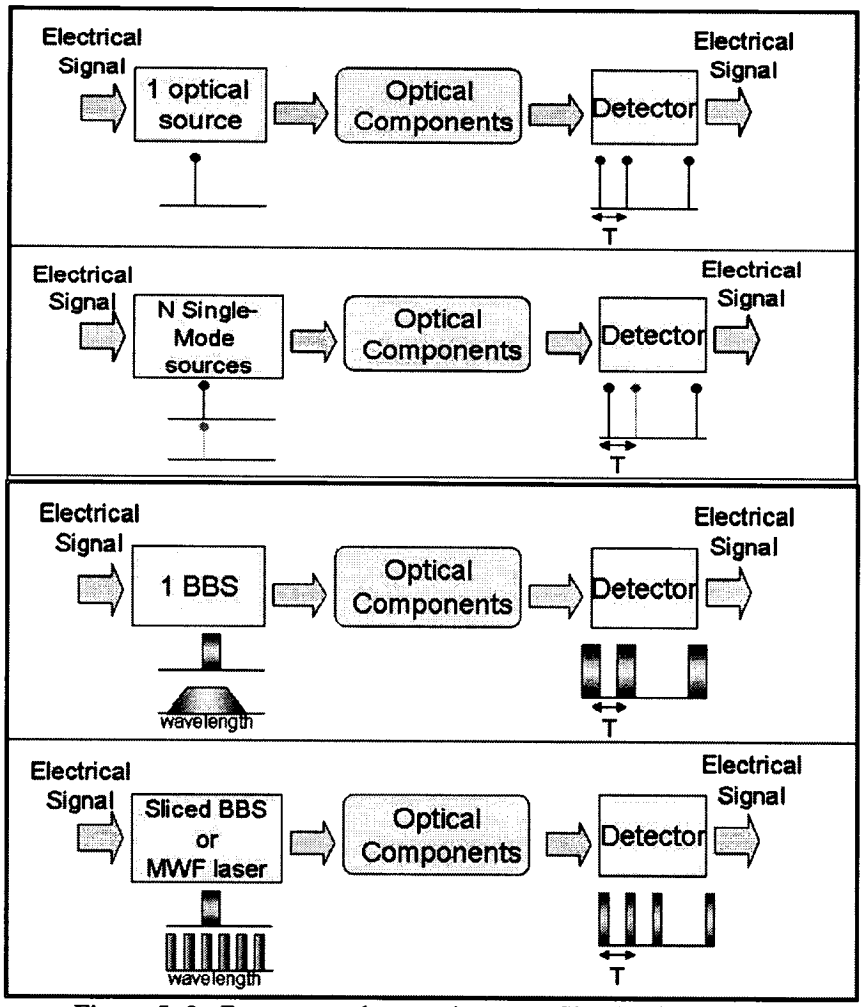

Figure 5- 2: Four approaches to microwave filter implementation.

In summary, the fourth technique offers the best solution in terms of filter characteristics, tunability and reconfiguration capabilities, as well as implementation simplicity. There have been two main schools of thought for the way in which this approach may be constructed: the optical carriers are either generated through spectrally sliced BBSs, or with a multi-waelength laser, and the delay lines may be implemented using fiber coils (fiber delay line filters—FDLFs), or fiber Bragg gratings (fiber grating delay line filters—FGDLFs) [5.1].

FDLFs:

Past photonic microwave filters based on fiber delay lines had to deal mainly with tunability and filter reconfiguration challenges. Many designs using a single tunable source were proposed as of 1994, but it was soon made clear that tunable multi-

wavelength sources were the key to implementing the most flexible filter responses. The first demonstration of a microwave filter based on spectrally sliced optical broadband sources dates back to 1996 when Foord et al. suggested a two-stage EDFA sliced with a tunable Michelson interferometer and externally modulated [5.10]. A length of dispersive fiber provided for the time delays before the signal was sent to a photodiode, preamplifier and analyzer. A filter based on seven taps having a Gaussian apodization profile was thus demonstrated. The main drawback of this technique is the low finesse of the interferometric filter, which thereby limits the performance of the overall microwave filter [5.1]. Later in 1999, Capmany et al. solved the problem by using a subnanometer high finesse FPF to also slice the broadband spectrum of an EDFA [5.11]. The 34 generated optical carriers thus provided for a filter sidelobe suppression ratio higher than 35dB. The problem with this approach, though, is the lack of filter tunability, as the FSR of the FPF cannot be varied. Future designs by Capmany et al. made use of FBGs instead to provide for tunability. In 2001, they proposed a multigigahertz tranversal notch filter based on the spectrum slicing of a broadband source by two uniform FBGS, one being made tunable by applying mechanical strain as shown in figure 5-3 [5.12].

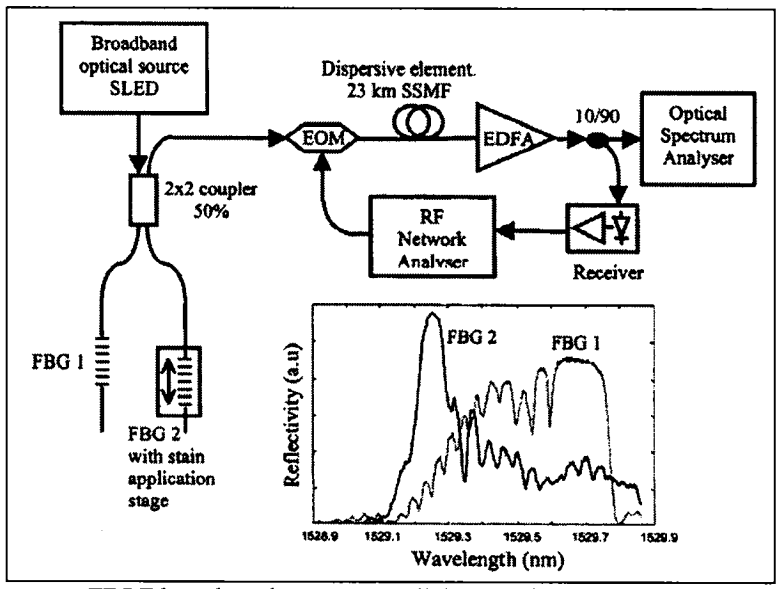

Figure 5- 3: Microwave FDLF based on the spectrum slicing of a broadband source via two uniform FBGs [5.12].

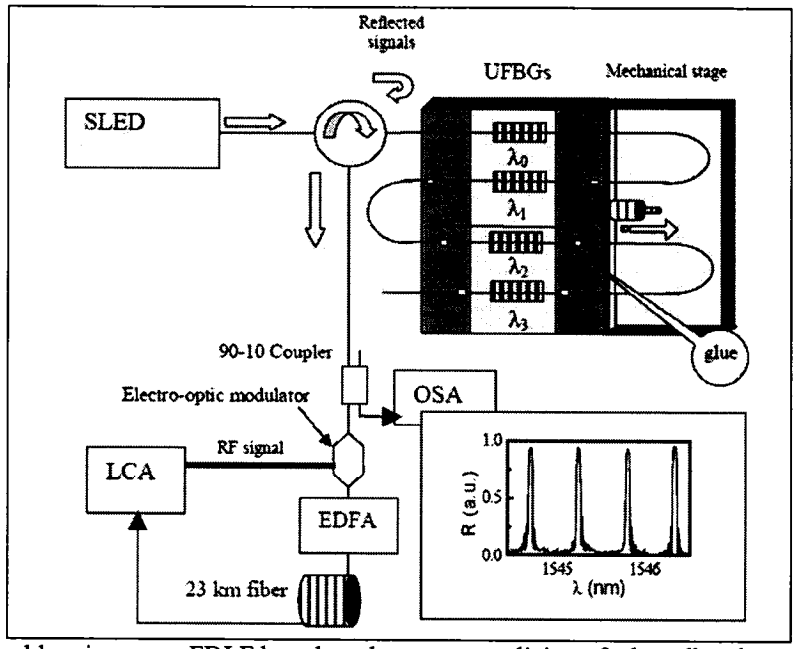

Figure 5- 4: Tunable microwave FDLF based on the spectrum slicing of a broadband source via a series of uniformly strained FBGs [5.5].

In 2002, an increased number of optical taps were created with a similar approach [5.5], as shown in figure 5-4. The FBGs were either in series or in parallel and hence providing for uniform wavelength spacing change between the optical taps. The grating reflectivity could also provide for weighing of filter coefficients. The same year, Zhang et al. proposed the use of a superstructured FBG to provide for the spectrum slicing method, giving precise filter characteristics with a rejection level greater than 45dB due to the intrinsic grating reflectivity apodization [5.6]. This technique, although offering high performances, does not allow for filter tunability. More recently, in 2005, Capmany's group extended the use of FBGs and made the spectrum slicing unit tunable by generating a periodic strain modulation along a uniform FBG using AOSLM, as mentioned in chapter 2. Hence, the acoustic wave frequency varies the filter FSR, and the acoustic wave power generated through a piezoelectric transducer offers filter reconfiguration [5.8]. The same group also investigated the option of using AWG's as spectrum slicing units [5.13-14]. In 2003, they have reported a 12 sample transversal filter using a two-stage 1x40 AWG, as shown in figure 5-5. If switches and variable attenuators are inserted between the two stages, different discrete FSRs and various filter configurations are possible [5.13]. More recently, the group also extended this filter design by offering even more filter tunability through the use of an 8x8 MEMS cross-connect with various

fiber delay lines, such that different amounts of time delays can be employed, and thus change the FSR accordingly [5.14].

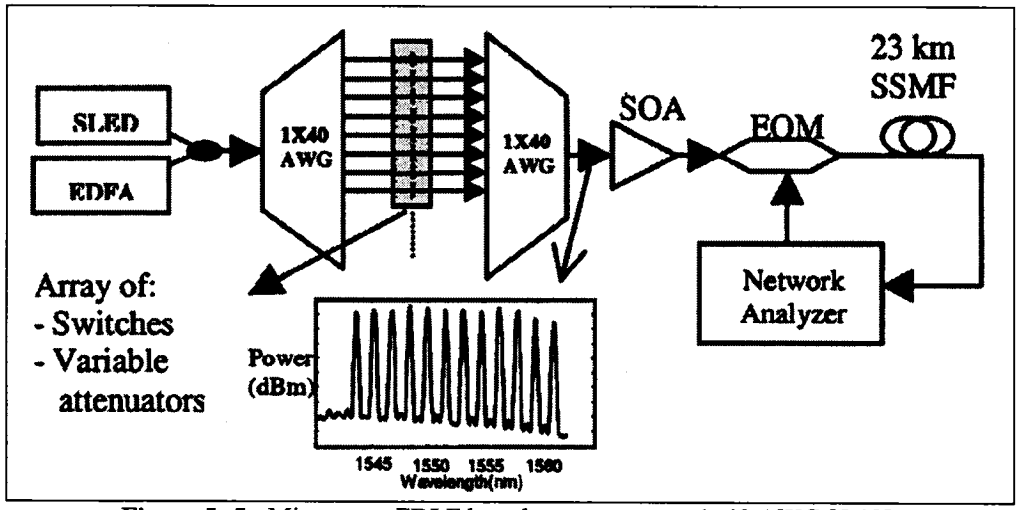

Figure 5- 5: Microwave FDLF based on a two-stage 1x40 AWG [5.13].

All of the above microwave filter implementations described made use of spectrum slicing techniques to create the optical taps. CW multi-wavelength lasers constructed using similar filtering techniques may also be employed to generate the optical taps, although not many previous works have been conducted using such laser sources.

An alternative method to using a tunable multi-wavelength source is to employ different amounts of dispersion to vary the time delays, and hence the FSR, of the filter. This was earlier proposed by Vidal et al. in 2003 [5.9]. They first made use of 2x2 optical switches to interconnect dispersive media, each having a dispersion D. The total dispersion will thus depend on the number of switch stages, and will increase exponentially as D, 2D, 4D...(2^{n-1})D, for n+1 2x2 switches, as demonstrated in figure 5-6. The same group also extended their proposition and later demonstrated the use of a NxN AWG as a switch element between different lengths of fiber delay lines to provide for discrete step tunability, as shown in figure 5-7 [5.7]. For such a system to work, the wavelength spacing of the source laser (an array or any MWL) must be made equal to that of the AWG FSR. If the input wavelengths are shifted by a multiple of the AWG channel spacing, another output port gets selected, and a new delay line becomes effective, thereby changing the microwave filter FSR. This method is an interesting approach,

although the input multi-wavelength laser(s) must be carefully designed in accordance with the optical delay line switch element.

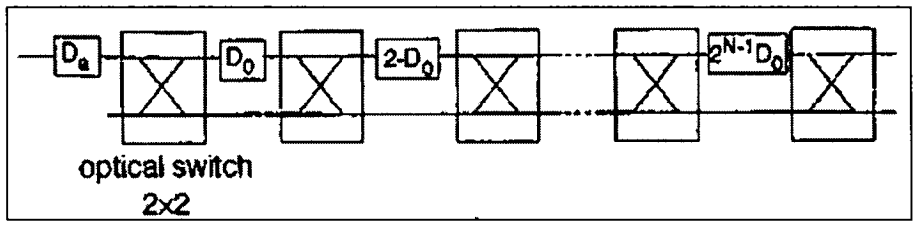

Figure 5- 6: Filter tunability via tunable delay lines: 2x2 switches [5.2].

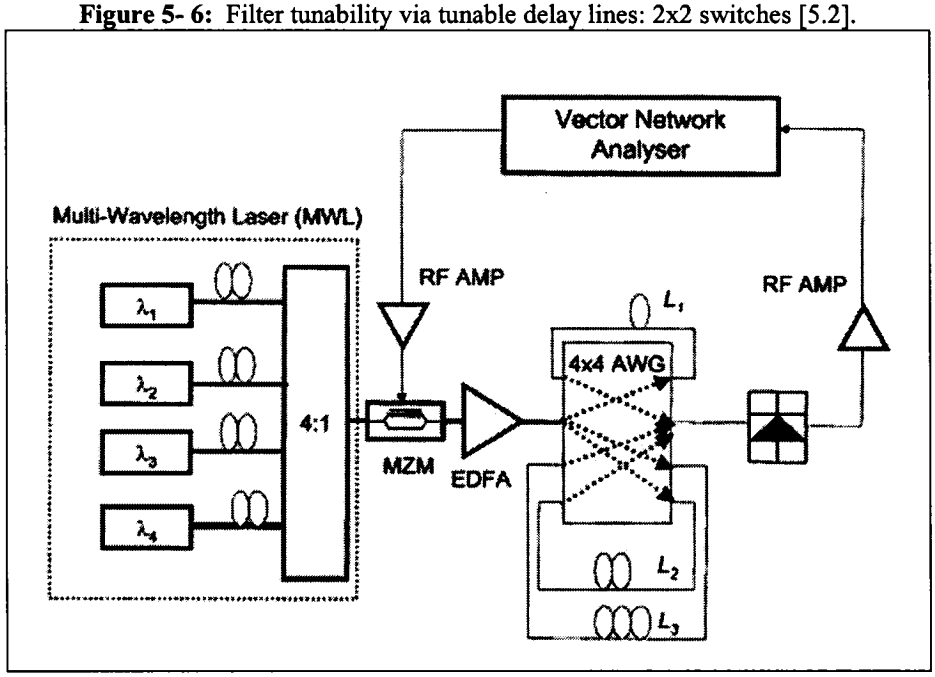

Figure 5- 7: Filter tunability via tunable delay lines: NxN AWG switches [5.7].

FGDLFs:

Photonic microwave filters based on FBG delay lines have also attracted much interest as they provide for a specifically designed dispersion profiles. In 1998, Marti et al. employed a multimode optical source in combination with a wideband chirped fiber grating (CFG). At the time, the tunability was however much limited to the grating bandwidth [5.15]. The group later proposed a better version by using electroabsorption modulators to vary the multimode source spacing between the lasing wavelengths, and thus offer both filter tunability and reconfiguration [5.16-17]. Since a single multimode source is employed, however, this poses a limitation on the number of possible filter taps. The problem was solved by Yu et al. by employing still a single tunable laser, but this time in conjunction with a 1x8 splitter where each output arm was connected to an array

of four FBGs. The choice in laser wavelength selects the appropriate operation grating in each arm and thus changes the amount of time delay between the generated filter taps. The weighing mechanism can even be obtained through the different grating reflectivities [5.18]. As such, a Hanning apodization function gave a filter stopband attenuation of over 30dB. The tunability is somewhat limited, however, to the number of FBGs used in each array.

All the implementations described above used a single laser source, and are thus limited in FSR since the allowable time delays must be set larger than the source's coherence time. The use of an array of lasers would prevent such coherence to occur but would also become impractical with the demand for larger optical bandwidths. A discretely tunable microwave filter using polaraization synthesis through a HiBi linearly chirped fiber Bragg grating (LCFBG) was hence proposed as an alternative. In this way, the filter becomes free of coherence interference of the input laser and continuous tuning is possible through the variable polarization delay line made of a HiBi fiber coupler, a polarization beam splitter and a HiBi LCFBG [5.9].

Generally speaking, high resolution tunable filters with higher quality factors have mostly been demonstrated using LCFBGs and an array of tunable lasers, such as the example shown in figure 5-8(a), and proposed by Capmany et al. [5.19-21]. Since each lasing wavelength is carefully chosen, a constant incremental delay T between the two adjacent wavelengths emitted by the array can be obtained through the use an LCFBG. Figure 5-8 (b) shows the group delay and reflectivity of the LCFBG they employed. The lasing wavelengths can further be varied by proper change of the laser central wavelength in the laser array. The output powers are also precisely controlled by each laser and the apodization process is made much simpler. Precise high-speed filter reconfiguration is thus possible. Many different filter characteristics were demonstrated: 3 to 5 input lasers with either Gaussian or Hanning apodized powers. Figure 5-9 shows the obtained spectrum for a five source laser array using either uniform or Hanning windowing. It is clear from the picture that Hanning apodization proves to offer a very good sidelobe suppression ratio [5.21].

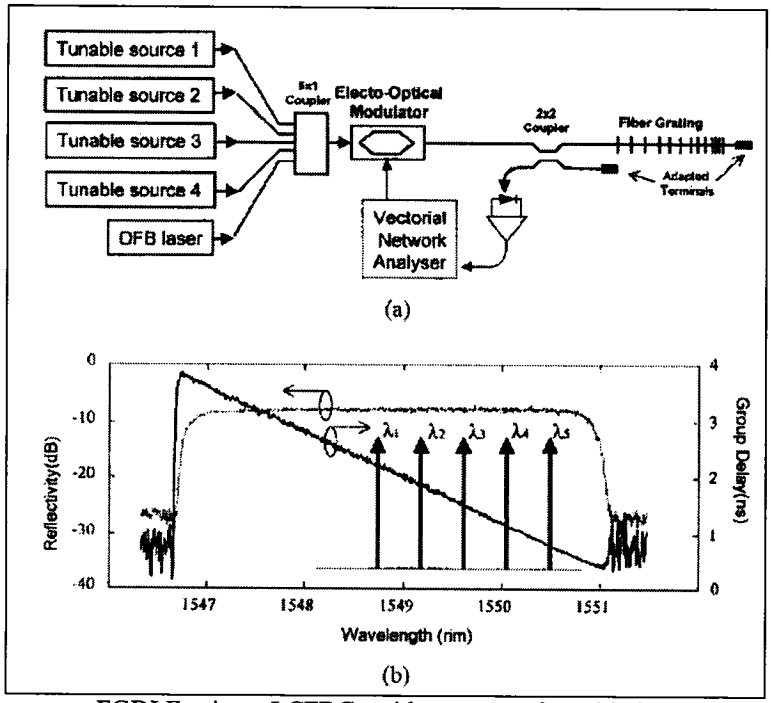

Figure 5- 8: Microwave FGDLF using a LCFBGs with an array of tunable lasers, Capmany et al. [5.21].

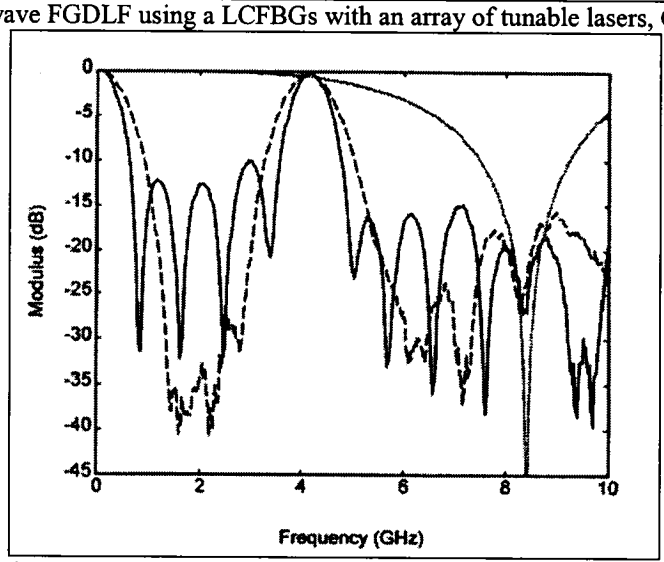

Figure 5- 9: Transfer function of the filter shown in figure 5-8 for five laser sources. The solid line represents the experimental results for uniform powers, while the dashed line shows the results for Hanning apodized tap powers. The dotted trace is the carrier suppression effect of AM modulation [5.21].

Capmany's research group also proposed the combination of an FBG spectrum sliced BBS with an LCFBG delay line [5.3]. Only two FBG's are used to slice the white light source, and thus a limited tuning range of 4nm is possible between optical carriers. This filter was tested in a frequency range of 0.5-6GHz. Later, the group explored filter tunability through the use of a uniform FBG whose chirp profile is controlled using a non uniform magnetic field and a magnetostrictive alloy as a transducer. A tunable filter

using an array of fixed lasing wavelengths was achieved by continuously changing the dispersion slope of the grating from 300-900ps/nm [5.1, 5.22]. This setup exhibited low extinction ratios, however, and the RF signal was not totally cancelled at the frequency notch. This was explained by the lack of phase matching between taps occurring because of the non-ideal behavior of the spectral dependence of the chirped grating time delay characteristics [5.23]. An alternative method to alter the magnetic chirp was given, but this technique can become complex under some applications, and a simpler filter setup would be more suitable.

The following addresses the efforts made to implement negative filter coefficients still under incoherent filter operation. Negative coefficients can make filters with flat passbands and sharper transitions without the zero-frequency baseband resonance that is always present when only using positive coefficients. Several techniques have been proposed: differential detection, hybrid optoelectronic, and all-optical approaches. Differential detection was first proposed in 1984, but only performed in 1995. In this case, two positive coefficient filters are combined and the signal subtraction is achieved in the final optoelectronic conversion. This structure duplication, however, requires an additional amount of components and careful path balance between the two filters is necessary before signal combination; all these factors make reconfiguration very difficult. In hybrid optoelectronic approaches, delay lines are optically implemented, while the filter taps are made electronically after being detected using either positive or negative current signals. This alternative is however very restrictive, as the filter performance is band limited to that of the electronic elements providing the taps; something we wanted to eliminate via the use of optical microwave solutions. The noise factor is also increased since active elements provide for tap weighing. An all optical approach is thus necessary. Recent research proposed the use of the π phase shift obtained in cross gain and cross phase wavelength conversions using SOAs [5.4]. This limits the filter bandwidth to that of the bandwidth conversion of the SOA, and such filters are difficult to reconfigure or to implement with several taps. Much more promising approaches include the use of a uniform FBG in transmission to "carve" out the negative filter taps from the broadband EDFA ASE spectrum. Tunability is also achieved by tuning the FBGs. The main

drawback is that the average optical radiation is never null and is equal to the average ASE radiation, giving rise to a dc component in the filter transfer function. This all-fiber solution is however polarization insensitive, a main advantage [5.24]. Another technique makes use of the counter phase modulation in a Mach-Zehnder external modulator [5.14]. The linear negative and positive parts of the modulator transfer function are used to implement both the negative and positive coefficients. A π phase shift will thus occur between the signals modulated at two bias voltages with equal magnitudes but opposite signs. A multi-wavelength source can thus create both positive and negative coefficients. The outputs from the modulators are then combined and sent to a dispersive element to create the time delay between the taps. This technique was demonstrated, amongst others, by Capmany et al. in 2005 [5.14]. They employed only one 2x1 Mach-Zehnder modulator with a tunable multi-wavelength spectrum sliced source created using a combination of AWGs, 2x2 switches and attenuators, together with an 8x8 MEMS switch that offered the use of different fiber delay lines, and thus increased filter tunability. This is, as of now, the best proposed method to implement negative taps with high filter flexibility, as the filter bandwidth is only limited by that of the modulator (which can be made high enough). There is also no need to duplicate the optical structure of the positive filter, and the tap weighing is independent of the way the negative sign is created [5.1].

5.4 Computer Simulations

In order to predict and better understand the behavior of our microwave filter under different conditions prior to performing any laboratory measurements, a simulation routine was coded in Matlab (refer to appendix II for codes). The simulation uses equation (32) for the transfer function magnitude versus frequency. The AM suppression factor, $\cos(\beta_2\Omega^2/2)$ term in equation (31), will be unavoidable in the laboratory since SSB modulation is not possible. This term is plotted separately for clarity purposes. It is understood that those two curves multiplied together is thus the final result that should be obtained.

5.4.1 Matlab Coding and Related Assumptions

Several assumptions have been made in order to perform such computations. First, the responsitivity R or the optical receiver is taken as being equal to one. The power losses induced by the dispersive element were also neglected. The input spectra for each wavelength spacing mode were taken directly from the SFL final characterization results given in chapter 3. While the first simulations were done only using the peak powers and lasing wavelengths, the final ones were performed using the entire SFL spectra, recorded over a relevant wavelength range with the maximum allowable resolution from the OSA. Finally, the dispersive element was modeled first using the SMF specified dispersion coefficient D (18ps/nm-km) times the length desired, and then by using the DL product measured in chapter 4. The fiber lengths were also varied, and the peak powers were either taken as is or equalized in order to clearly understand the effects of changing any parameter on the overall filter response. The following section clearly explains and demonstrates these effects individually or in pairs, carefully examining how filter tunability and reconfiguration is possible using our SFL as an optical carrier source.

5.4.2 Simulating the effects of various parameters on filter response

5.4.2.1 Wavelength spacing between emitting modes

Since the SFL emits with either 1.6nm or 3.2nm spacing between each lasing mode, it is important to understand how each state will change the filter response. The FSR of the filter is inversely proportional to the wavelength spacing multiplied with the dispersion induced by the delay line, as seen in section 5.2. Hence, smaller wavelength spacings will generate larger FSRs for fixed dispersion characteristics. Figures 5-10 a) and b) show the transfer function for both wavelength spacings (1.6nm and 3.2nm), with both 7 taps spread across a wavelength range of approximately 1538nm to 1548nm for the 1.6nm spacing, and from 1545nm to 1565nm for the 3.2nm spacing. The dispersive

element was modeled with a 30km length of SMF with D =18ps/nm-km at 1550nm. Note that the carrier peak powers were equalized in these graphs. These show clearly how the FSR doubles when the input wavelength spacing is halved.

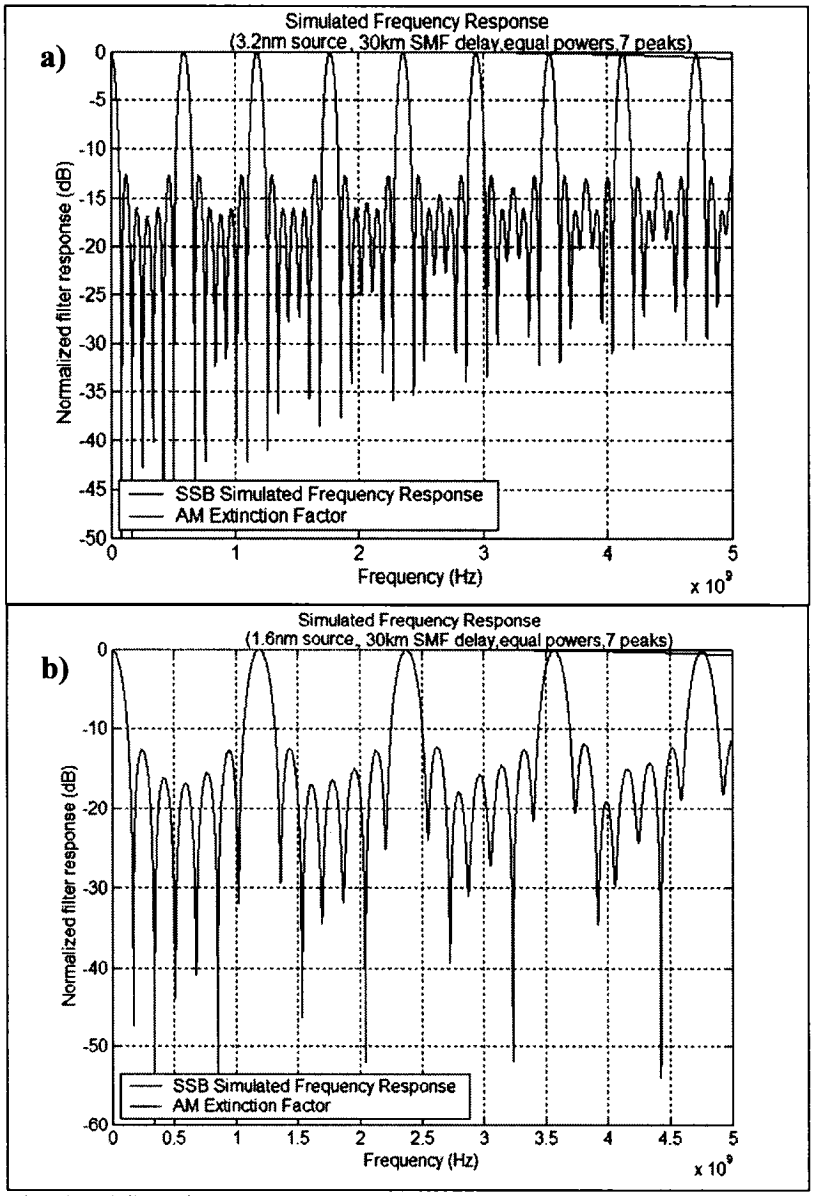

Figure 5- 10: Simulated filter frequency response for 7 taps spaced out by a) 3.2nm and b) 1.6nm, using 30km of SMF dispersive fiber.

5.4.2.2 Number of emitting modes

The number of lasing wavelengths, or taps, will also change the behavior of the filter response. From previous theoretical notions, one expects that more taps generate less sidelobes and thus a better Q factor. Figures 5-11 a) and b) show the responses for

the 3.2nm wavelength spacing source, with 7 and 13 emitting peaks respectively. In reality, however, the 3.2nm spacing state of the SFL emits only 7 peaks. If more modes were possible at 3.2nm spacing, the filter response would be better. These simulations were performed with equalized peak powers as well, and only the peak lasing wavelengths, using 30km of SMF as in the previous examples.

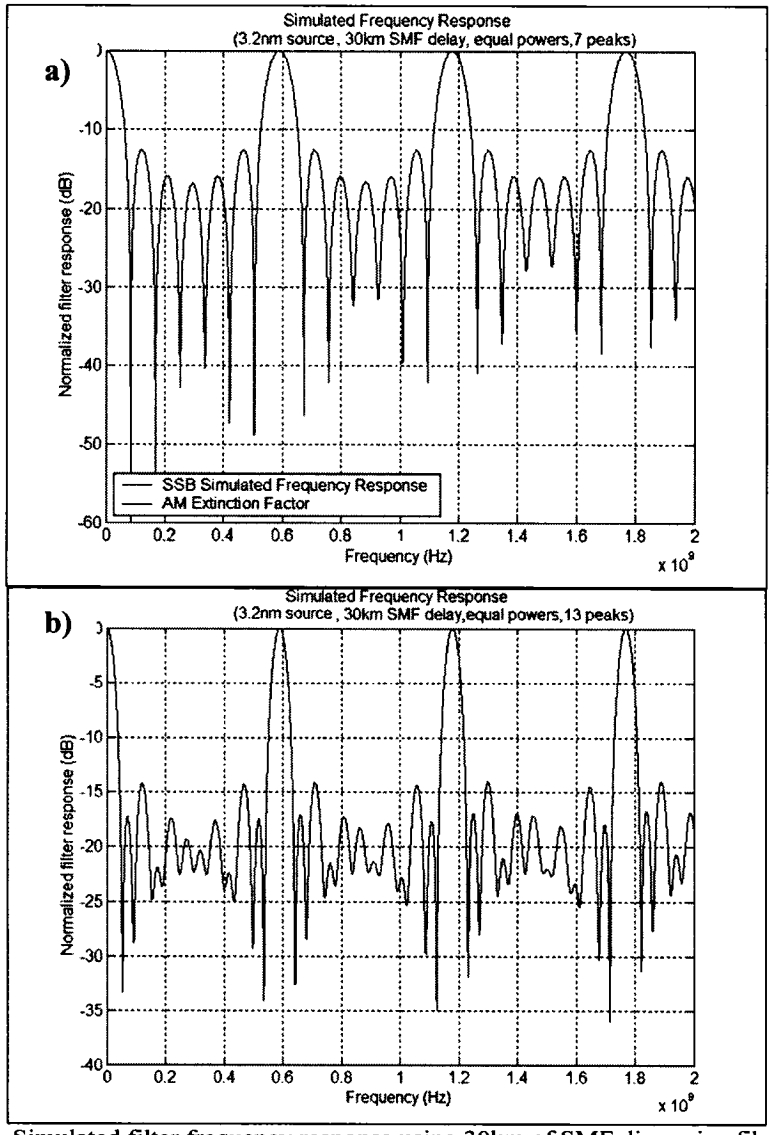

Figure 5- 11: Simulated filter frequency response using 30km of SMF dispersive fiber for a) 7 taps (zoomed version of figure 5-10a) and b) 13 taps, both spaced out by 3.2nm.

5.4.2.3 Variation in peak powers

All the previous examples showed the responses obtained from equalized powers. Changing the powers of each tap will undoubtedly vary the filter characteristics, or reconfigure the response. From filter theory, it is known that some power apodizations lead to better filter responses. As a comparison to figures 5-10 and 5-11, and in preparation to what laboratory measurements will reveal, figures 5-13 a) and b) demonstrate the transfer function simulated using both 1.6nm and 3..2nm wavelength spacings with the same lasing peak powers and number of modes as those shown in figure 5-12. The dispersive element is kept the same, that is, 30km of SMF fiber. From these we notice how the sidelobes differ from equalized peak power responses. They are less present since apodization reduces their importance. It is also interesting to note how the spectra for the 3.2nm state is generally better power distributed. This is much less noticeable for the 1.6nm spectra, making the fact that this input state offers more taps even more interesting, as more lasing modes can balance out the negative effect its poorer peak power distribution has on the overall filter response.

Input Spectra from the SFL

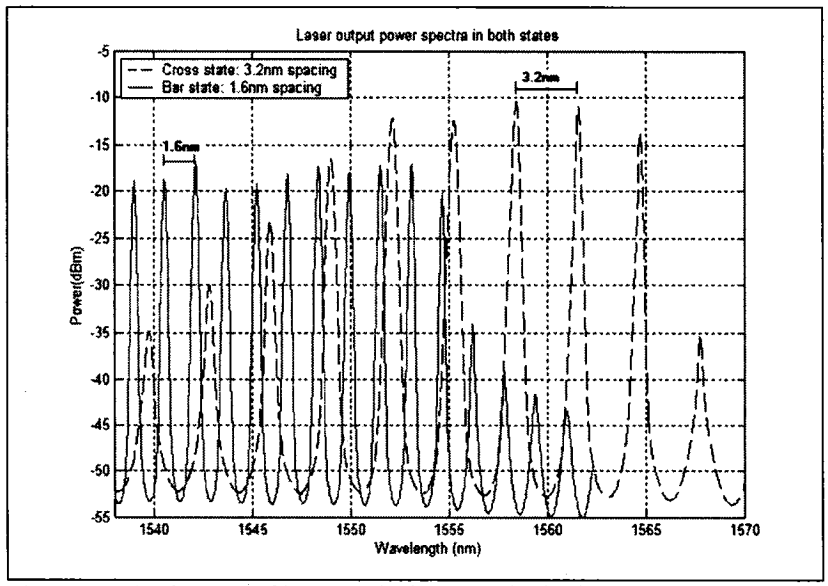

Figure 5- 12: Spectra of input optical SFL under both wavelength spacings.

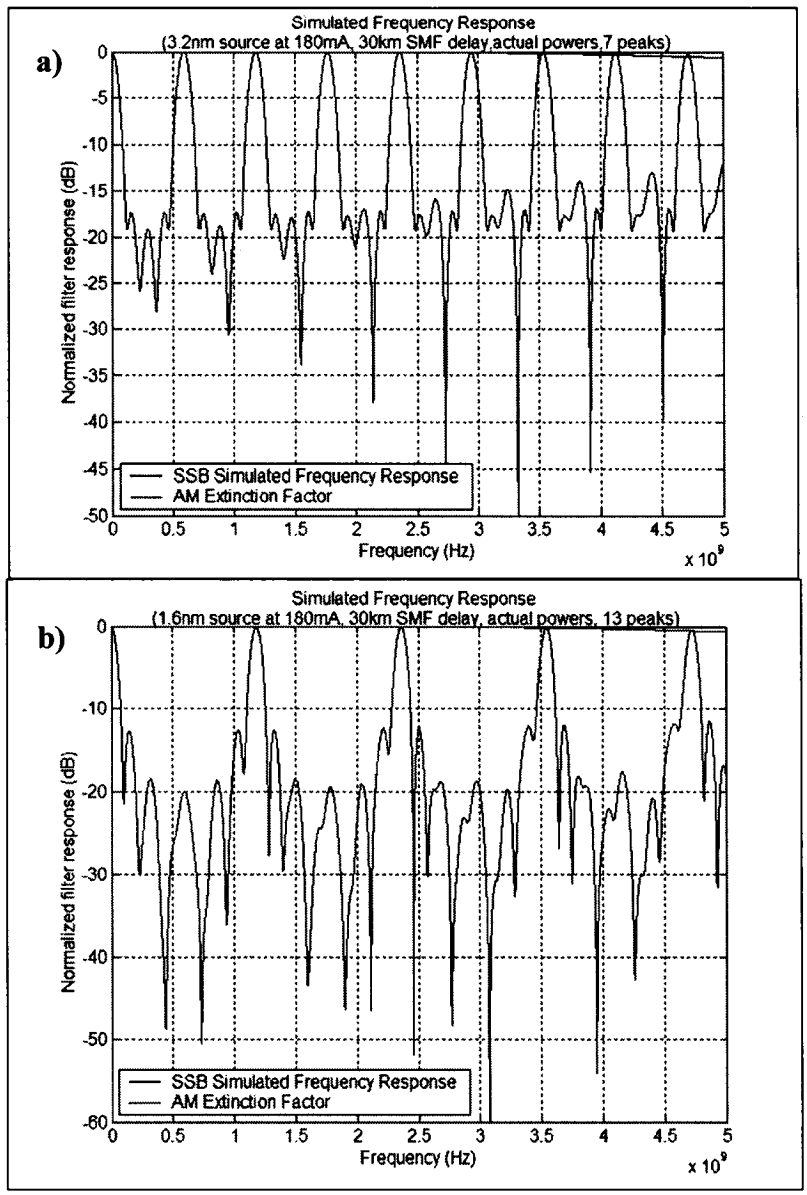

Figure 5- 13: Simulated filter frequency response for the real input powers of the SFL and 30km SMF: a) 3.2nm spacing: 7 taps and b) 1.6nm spacing: 13 taps.

5.4.2.4 Variation in dispersion-length profile of delay line

The ultimate variable leading to the tunability of our microwave filter is changing the length or the dispersion profile of the delay component. Again from theory, we know that greater lengths of fiber, of larger DL products, lead to smaller FSRs, for any fixed wavelength spacing. Figures 5-14 a) and b) present the transfer functions of both spacings with 10km SMF. These may be compared to the 30km examples given earlier.

The actual peak powers were conserved in both cases as well. We notice how smaller lengths of SMF induce less delay, and hence a larger FSR.

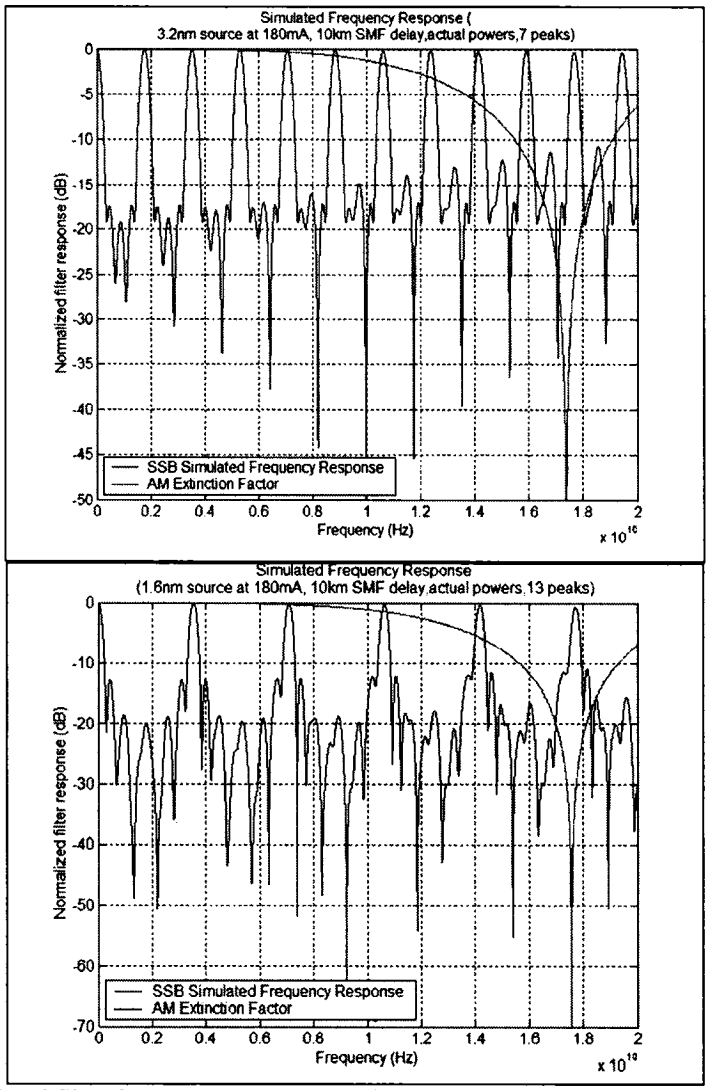

Figure 5- 14: Simulated filter frequency response for the real input powers of the SFL and 10km SMF: a) 3.2nm spacing: 7 taps and b) 1.6nm spacing: 13 taps. (from 0 to 20GHz)

All the above simulations were performed using only the peak powers and wavelengths. These thus assumed a null peak linewidth. In reality, however, and as we will see in the next section with the comparison of the experimental results to the simulations done with the entire SFL output spectra, the increased linewdith of each peak combined with the delay line's second-order dispersion induces an expected low-pass envelope to the overall transfer function.

5.5 Experimental Measurements

5.5.1 Experimental Measurement Setup

Figure 5-15 shows the setup employed for performing the measurements presented in this section.

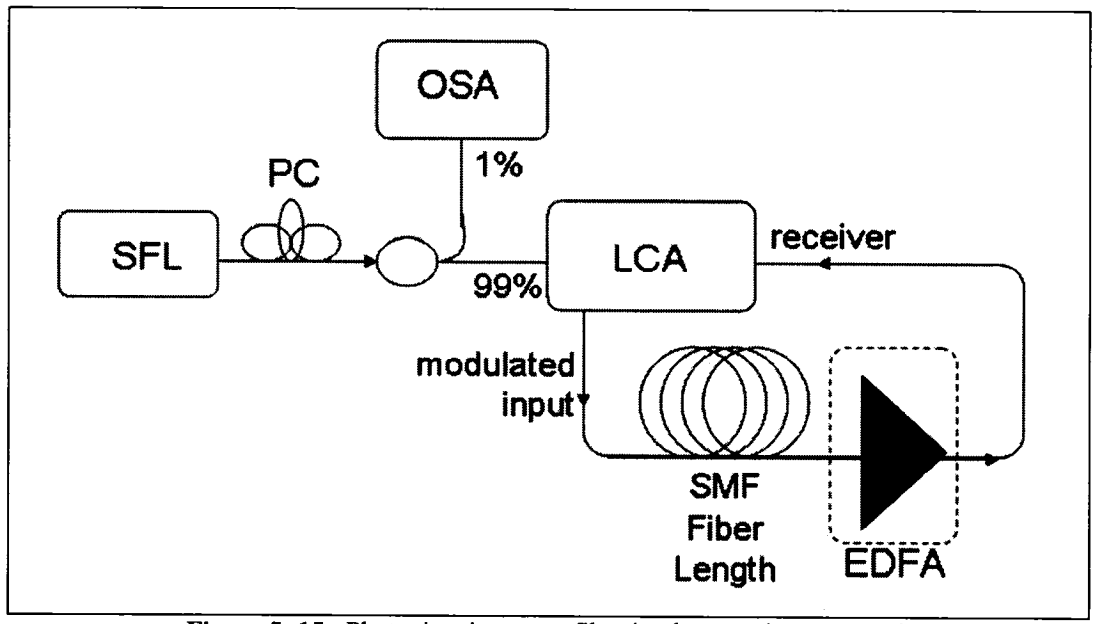

Figure 5- 15: Photonic microwave filter implementation proposed.

The SFL output spectra is monitored using a 1% tap in order to later compare the measured data with the simulated one performed using the same input spectra. The same lightwave component analyzer as in chapter 4 is then employed to internally modulate the source with an RF frequency, send it to the dispersive element, and read the filter's magnitude response as a function of frequency through its internal photodetection process. The frequency range readable by the LCA is from 50MHz to 20GHz. The resolution is set to the maximum number of points allowable within the desired range, that is, 1601 points. The polarization controllers ensures that the modulation is performed under optimized conditions.

An EDFA may also be inserted before the receiver end of the LCA in order to compensate for the losses induced by the fiber delay line and permit better measurements, especially for setups using the longest fiber spools. The LCA must be calibrated with the desired EDFA pump power and the SFL input source prior to taking any measurements.

5.5.2 Laboratory results

The following figures present the measurements taken for both fiber delay line samples B and D, under both SFL wavelength spacing states, with and without an EDFA pumped at 50% power. In the first graph of each set, the solid blue line shows the normalized AM simulated response (equation 31), while the dashed line represents the measured response. The second graph of each pair is the corresponding input spectra associated with these measures and simulations. The dispersion profiles of samples B and D, which were initially taken from the measured values of chapter 4, were slightly adjusted by trial end error in order to fit the simulated data to the measured response. The adjustments were very minor but gave an even more precise idea of the length and dispersion these samples really exhibit. The dispersion-length characteristics (refer to chapter 4) were thus changed to the following values: sample B has a slope of 0.5868 ps/nm^2 and a -751.00 ps/nm offset, while sample D has a slope of 1.868 ps/nm^2 and an offset of -2.345e3 ps/nm.

Four sets of FSRs are measured. Table 5-1 shows all the parameters collected for each set of results. Generally speaking, most parameters remain the same with or without the use of an EDFA. Only the losses and noise are changed. That is why the contrast may be altered, though the main cause for contrast change probably arises from a difference in tap powers arising from a different SFL polarization controller setting. The highest measured contrast of over 35dB was collected with the 3.2nm wavelength spacing and sample D dispersive element (figure 5-22). The input spectra of the SFL taken for this measurement shows nicely apodized lasing peak powers, with one more lasing wavelength than with the case when no EDFA was used (figure 5-16b). This is thus an example of the type of filter reconfiguration that we could accomplish with this filter design.

Delay sample	SFL Wavelength spacing	FSR (GHz)	St. Dev. (+/-)	Contrast (dB)	St. Dev. (+/-)	FWHM (GHz)	St. Dev. (+/-)
B	**3.2nm**	1.8	0.7%	30/25(EDFA)	10%	0.36	5%
B	**1.6nm**	3.75	0.3%	25/20(EDFA)	9%	0.42	10%
D	**3.2nm**	0.51	0.8%	23/35(EDFA)	15%	0.11	23%
D	**1.6nm**	1.11	1%	15/20(EDFA)	12%	0.12	25%

Table 5- 1: Summary of measured filter characteristics. The measures were averaged over the first clearest passebands, with the corresponding standard deviations.

1) No EDFA results:

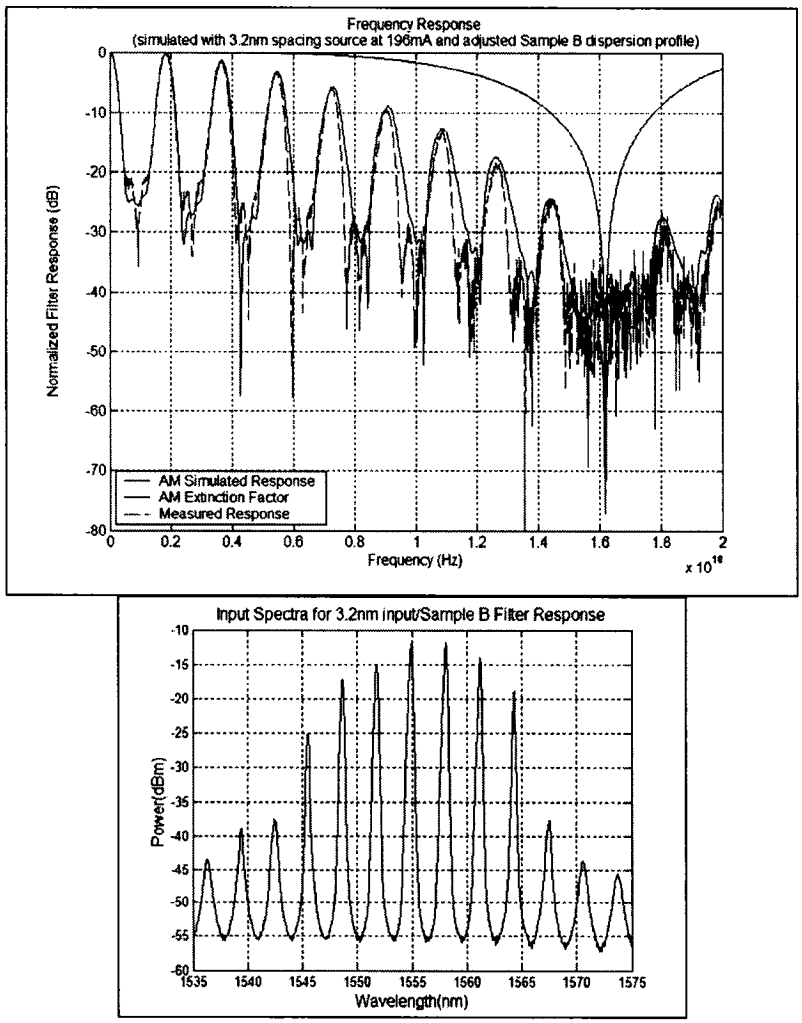

Figure 5- 16: a) Comparison between experimental and simulated filter responses for sample B delay line and the 3.2nm wavelength spacing input spectra shown in b).

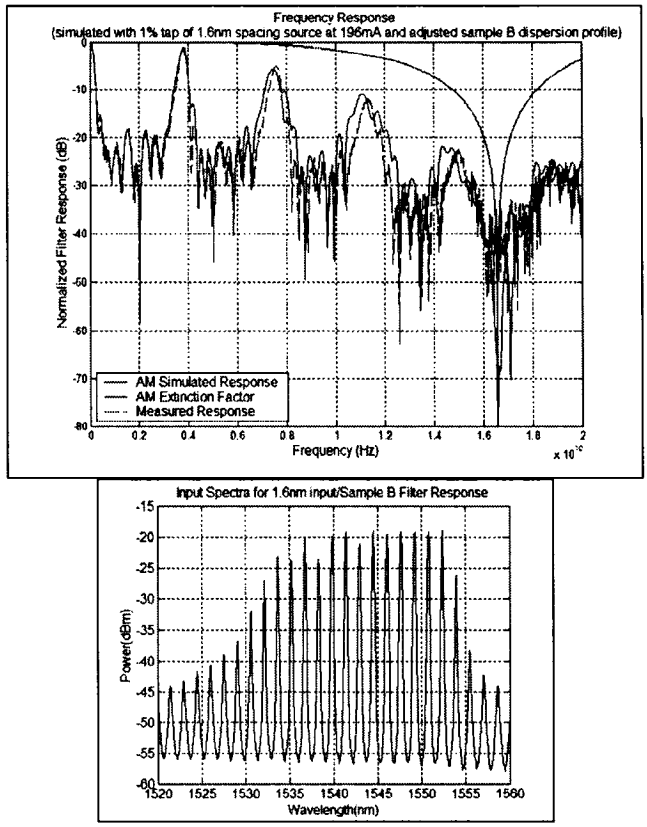

Figure 5- 17: a) Comparison between experimental and simulated filter responses for sample B delay line and the 1.6nm wavelength spacing input spectra shown in b).

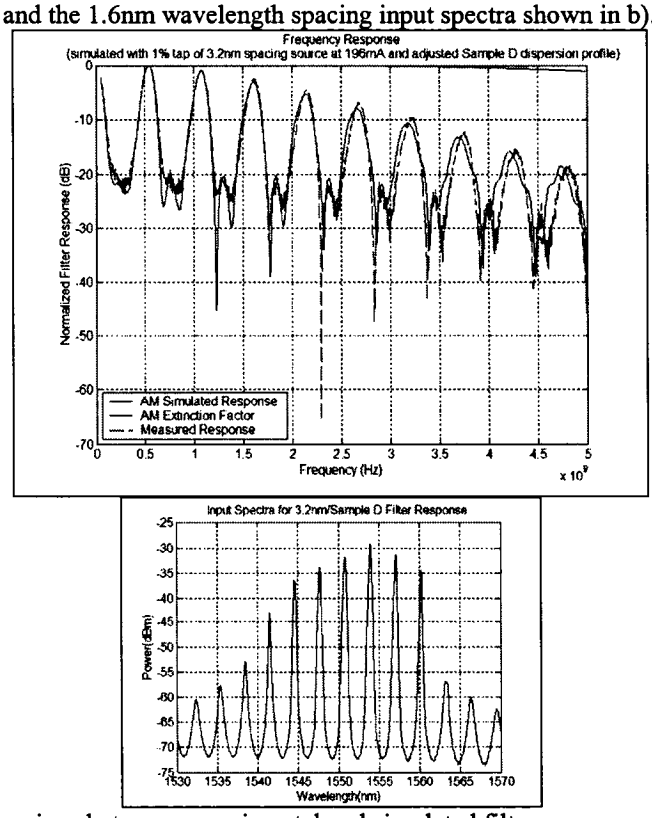

Figure 5- 18: a) Comparison between experimental and simulated filter responses for sample D delay line and the 3.2nm wavelength spacing input spectra shown in b).

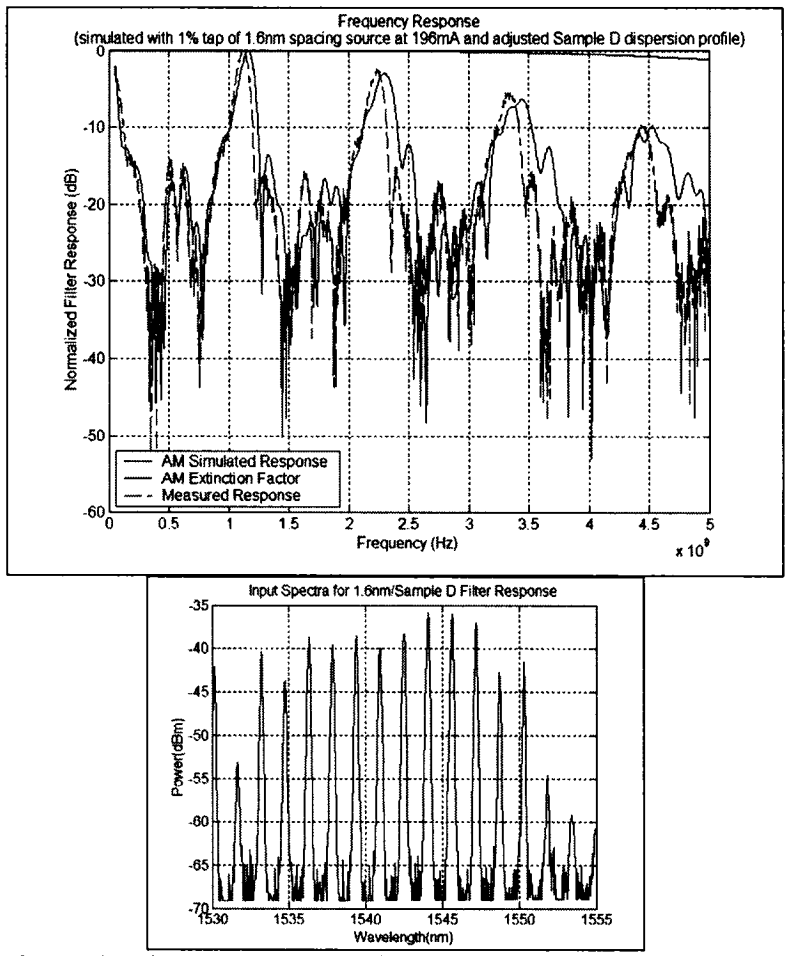

Figure 5- 19: a) Comparison between experimental and simulated filter responses for sample D delay line and the 1.6nm wavelength spacing input spectra shown in b).

2) 50% EDFA before receiver:

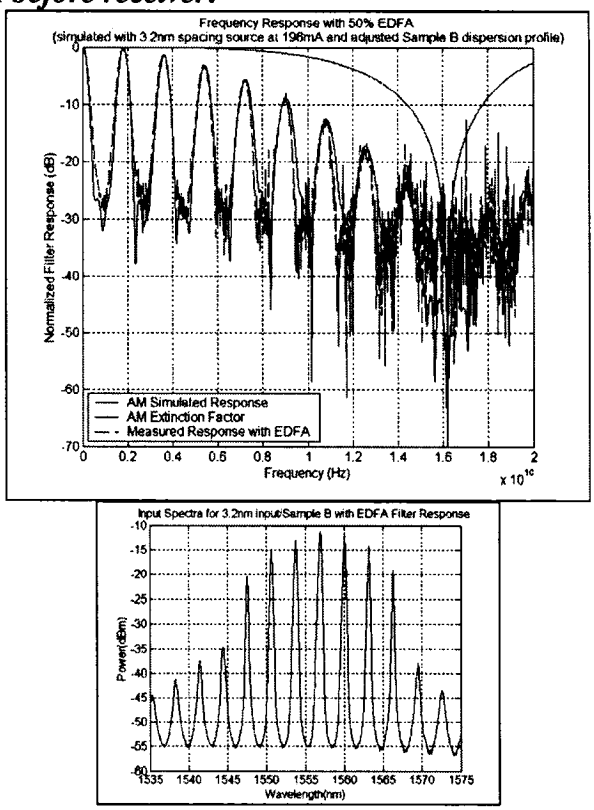

Figure 5- 20: a) Comparison between experimental results with EDFA and simulated filter responses for sample B delay line and the 3.2nm wavelength spacing input spectra shown in b).

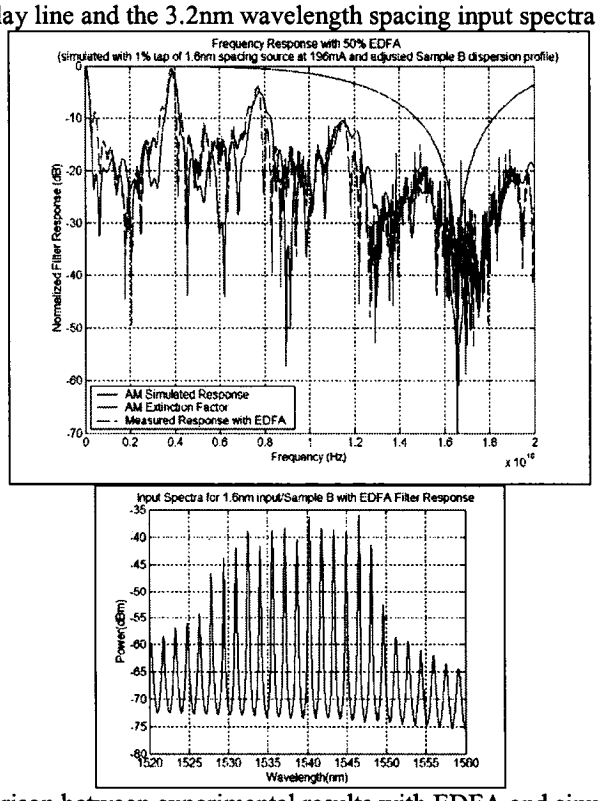

Figure 5- 21: a) Comparison between experimental results with EDFA and simulated filter responses for sample B delay line and the 1.6nm wavelength spacing input spectra shown in b).

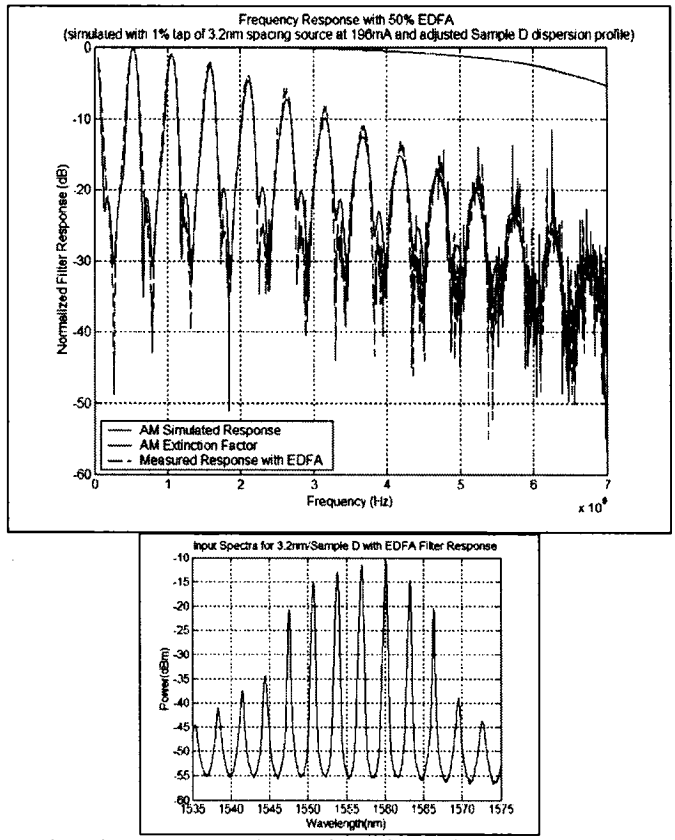

Figure 5- 22: a) Comparison between experimental results with EDFA and simulated filter responses for sample D delay line and the 3.2nm wavelength spacing input spectra shown in b).

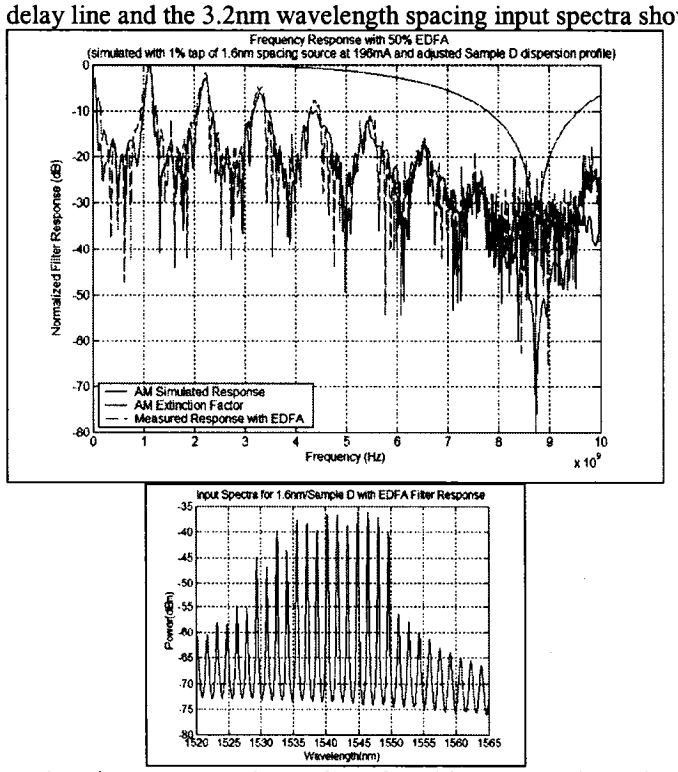

Figure 5- 23: a) Comparison between experimental results with EDFA and simulated filter responses for sample D delay line and the 1.6nm wavelength spacing input spectra shown in b).

5.5.3 Comparison with Simulated Responses

The previous figures show a nice agreement between simulations and experimental measurements. The results obviously present more noise and power losses, although all transfer functions were power normalized. We also notice that the use of an EDFA reduces the consequences of power loss but induces extra noise as frequency increases. The slight variations between measurements and simulations are mainly due to amplitude and frequency variations that may be caused by either temperature fluctuations or polarization instabilities [5.7]. Such transversal optical filters are indeed relatively sensitive to environmental disturbances and more control over these disturbances is needed for future applications.

5.6 Discussion

Before any further discussion, let us investigate the various limitations faced by the realization of any microwave photonic filter. First, there exists a maximum RF power or modulation index that may be sent to the external modulator. The photodetector can also generate intermodulation effects if too much power is incident on its surface, and fiber non-linearities may also occur if the optical carriers have too high powers [5.1], although this is not a problem in our case. Other effects such as polarization sensitivity must be considered however. It is thus important that polarization controllers be employed to adjust the source polarization before modulation. Optical source phase noise may also affect the filter characteristics. In incoherent operation, the noise will be periodic in frequency and will show notches at the zero frequency and at all FSR multiples [5.1]. If optical amplifiers are employed, new RF noise can appear because of the beating between the signal and the ASE of the amplifier, but this noise is shown to be very small compared to the filter response.

The results collected are very promising, although minor changes could improve for filter finesse, contrast and flexibility. First, the carrier-suppression or AM extinction effect may be compensated for by using SSB modulation in dual-drive MZM [5.7]. More control over the multi-wavelength source lasing peak powers would offer greater control

over filter windowing capabilities and provide for higher finesse, or quality factor, and contrast. The 3.2nm wavelength spacing of the SFL, for example, provides for a nicely apodized output power spectrum which generates the highest Q factors and filter contrasts (over 30dB). On the other hand, the irregularities in the SFL output peak powers of the lasing wavelengths spaced out by 1.6nm cause non-uniformities in filter responses, and thus provide for lower finesse and contrasts. It is though that by adding a second SOA with a gain peak slightly offset compared to the first SOA, together with a variable attenuator to control loss into the ring laser cavity, better SFL output peak power control, and thus filter apodization may be achieved. Finally, more tunability could be offered by either increasing the SFL wavelength spacing variations, or by using a variable fiber delay line matrix as proposed in many earlier filter schemes [5.2, 5.7, 5.14].

5.7 Conclusion

The above demonstration has shown that our tunable multi-wavelength SFL could provide for a reliable optical source in the realization of a tunable microwave filter. The results nicely agreed with the simulations, and the best sidelobe suppression was greater than 30dB. Four sets of FSR were made possible by both changing the wavelength spacing or the dispersive element. Reconfiguration was limited, but still demonstrated through a slight variation of the lasing peak powers by changing the axis of the polarization controllers and the SOA bias current of the SFL. Increased filter flexibility could be made possible by adding additional HiBi fiber segments into the SFL tunable filter, thereby providing for more than two source wavelength spacings and more filter FSRs. A dispersion matrix could also provide for further tunability. This filter implementation could even be easily adapted for fiber radio LMDS applications requiring an FSR of 28GHz, or approximately 0.62km SMF delay line under 3.2nm SFL wavelength spacing [5.11].

The best-case photonic microwave filters proposed until now present sidelobe suppression ratios of around 30-40dB, which is far from the currently available passive electrical microwave filters with ratios of 100dB. Electrical filters have many

disadvantages, however, that could be overcome with photonics. Optical filtering offers the possibility to easily extend the spectral region of operation to higher ranges—millimeter and THz regions. Noise and nonlinearities can also be more easily handled in the optical domain. Near future photonic microwave filters will be made reliable, compact, tunable, and reconfigurable. The rise of integrated optics, photonic crystal devices and fibers, will surely make possible the implementation of filters with higher quality factors of over 500, which will give rise to much higher extinction ratios. Some more research may also make the implementation of coherently operated filters more feasible, as these would allow for complete filter flexibility [5.1].

5.8 References

5.1 J. Capmany, B.Ortega, D.Pastor, S.Sales. "Discrete-time processing of microwave signals," *J. of Ligthwave Technol.*, vol. 25, no. 2, pp. 702-723, February 2005.

5.2 B. Vidal, V. Polo, J.L. Corral and J. Marti, "Photonic microwave filter with tuning and reconfiguration capabilities using optical switches and dispersive media," *Electronics Letters*, vol.39, no.6, pp. 547-549, March 2003.

5.3 J. Mora, B. Ortega, J.L. Cruz, J. Capmany, D. Pastor, M.V. Andres. "White light sources filtered with fiber Bragg gratings for RF-Photonics applications," Optics Communications, vol. 8878, pp.1-5, May 2003.

5.4 F. Coppinger, S. Yegnanarayanan, P.D. Trinh,, B. Jalali. "All-optical RF filter using amplitude inversion in a semiconductor optical amplifier," *IEEE Transactions on Microwave Theory and Techniques,* vol. 45, no.8, pp. 1473-1477, August 1997.

5.5 J. Mora, B. Ortega, J. Capmany, J.L. Cruz, M.V. Andres, D. Pastor, S. Sales. "Automatic tunable and reconfigurable fiber-optic microwave filters based on a broadband optical source sliced by uniform fiber Bragg gratings," *Optic Express*, vol.10, no.22, pp. 1291-1298, November 2002.

5.6 B.A.L. Gwandu,W. Zhang,, J.A.R. Williams, L. Zhang, I. Bennion. "Microwave photonic filtering using Gausian-profiled superstructured fibre Nragg grating and dispersive fibre," *Electronics Letters,* vol.38, no.22, pp.1328-1330, October 2002.

5.7 V. Polo, B. Vidal, J.L. Corral and J. Marti, "Novel Tunable Photonic microwave fFilter based on laser arrays and NxN AWG-based delay lines," *IEEE Photonics Technology Letters*, vol.15, no.4, pp. 584-586, April 2003.

5.8 M. Delgado-Pinar, J.Mora, A. Diaz, and M.V.Andres. "Tunable and reconfigurable microwave filter by use of a Bragg-grating-based acoustico-

optic superlattice modulator," *Optics Letters*, vol.30, no.1, pp. 8-10, January 2005.

5.9 Y. Xiaoke, Y. Xiufeng, Wen-De, F. Wei, D. Lei, W. Yixin, L. Chao, "Continuously tunable microwave photonic filter design using high-birefringence linear chirped grating," *IEEE Photonics Technol. Letters,* vol.15, no.5, pp. 754-756, May 2003.

5.10 A.P.Foord, P..Davies and P.A. Greenhalgh. "Synthesis of microwave and millimeter wave filters using optical spectrum-slicing," *Electronics Letters*, vol.32, no.4, pp. 390-391, February 1996.

5.11 J. Capmany, D. Pastor, B. Ortega. "Fibre optic microwave and millimeter-wave filter with high density sampling and very high sidelobe suppression using subnanomter optical spectrum slicing," *Electronics Letters*, vol.35, no.6, pp. 494-496, March 1999.

5.12 D. Pastor, J. Capmany, B. Ortega. "Broadband tunable microwave transversal notch filter based on tunable uniform fiber Bragg gratings as slicing filter," *IEEE Photonics Technology Letters*, vol. 13, no.7, pp. 726-728, July 2001.

5.13 D. Pastor, B. Ortega, J. Capmany, S. Sales, A. Martinez and P. Munoz. "Optical microwave filter based on spectral slicing by use of arrayed waveguide gratings," *Optics Letters*, vol.28, no. 19, pp. 1802-1804, October 2003.

5.14 J. Capmany, J. Mora, B. Ortega, D. Pastor. "Microwave photonic filters using low-cost sources featuring tunability, reconfigurability and negative coefficients," *Optics Express*, vol. 13, no.5, pp. 1412-1417, March 2005.

5.15 J. Marti, F. Ramos, R.I. Laming, "Photonic microwave filter employing multimode optical sources and wideband chirped fibre gratings," *Electronics Letters*, vol. 34, no.18, pp. 1760-1761, September 1998.

5.16 J. Marti, V. Polo, F. Ramos, D. Moodie. "Photonic tunable microwave filters employing electroabsoprtion modulators and wideband chirped fibre gratings," *Electronics Letters*, vol. 35, no.4, pp. 305-306, February 1999.

5.17 J. Marti, V. Polo, F. Ramos, D. Moodie, D. Wake. "Synthesis of photonic microwave filters based on external optical modulators and wide-band chirped fiber gratings," *J. of Ligthwave Technol.*, vol. 18, no. 2, pp. 213-220, February 2000.

5.18 G. Yu, W. Zhang and J.A.R. Williams. "High-performance microwave transversal filter using fiber Bragg grating arrays," *IEEE Photonics Technol. Letters*, vol.12, no.9, pp. 1183-1185, September 2000.

5.19 D. Pastor, J. Capmany, "Fibre optic tunable transversal filter using laser array and linearly chirped fibre grating," *Electronics Letters*, vol.34, no.17, pp. 1684-1685, August 1998.

5.20 J. Capmany, D. Pastor, B. Ortega. "Experimental demonstration of tunability and transfer function resonfiguration in fibre-optic microwave filter composed of linearly chirped fibre grating fed by laser array," *Electronics Letters*, vol.34, no.23, pp. 2262-2263, November 1998.

5.21 J. Capmany, D. Pastor, B. Ortega. "Efficient sidelobe suppression by source power apodization in fibre optic microwave filters composed of linearly

chirped fibre grating by laser array," *Electronics Letters*, vol. 35, no.8, pp. 640-642, April 1999.

5.22 P.M. Lane and K. Kitiyama. "Optical generation of mm-waves using spectrum-sliced ASE for low-cost WD based fibre radio systems" *Electronic Letters*, vol. 34, no.10, pp. 1010-1011, May 1998.

5.23 J. Mora, B. Ortega, J.L. Cruz, J. Capmany, D. Pastor, M.V. Andres, S. Sales. "Dynamic optical transversal filters based on a tunable dispersion fiber Bragg grating," March 2002: Available online at www.uv.es/~jmoraa/artic/mwp01.pdf

5.24 J. Mora, M.V. Andres, J.L. Cruz, B. Ortega, J. Capmany, D. Pastor, S. Sales, "Tunable all-optical negative multitap microwave filters based on uniform fiber Bragg gratings," *Optics Letters*, vol.28, no.15, pp. 1308-1310, August 2003.

Other Readings:

- Y. Xiaoke, F. Wei, N.J. Hong, L. Chao. "Tunable microwave filter design using wavelength conversion technique and high dispersion time delays," *IEEE Photonics Technol. Letters*, vol.13, no.8, pp. 857-859, August 2001.
- J. Capmany, J. Cascon, D. Pastor, B. Ortega. "Reconfigurable fiber-optic delay line filters incorporating electrooptic and electraabsorption modulators," *IEEE Photonics Technol. Letters*, vol. 11, no.9, pp. 1174-1176, September 1999.

VI. General Conclusion

This thesis investigated the various ways to implement a continuous-wave tunable MWS. Several past experimentations guided the light towards the development of a new kind of SFL, where the tunability was made possible through the use of a special class of HiBi Sagnac loop, or a HiBi-FLM. This filter could be switched between two different wavelength spacings by means of two 2x2 switches, and two sets of HiBi fiber lengths and polarization controllers. Various fiber ring cavity designs were tested: one or two SOAs, with or without a variable attenuator. The design with the highest output powers, smallest peak linewidths and best spectrum flatness was kept. The SFL operation was demonstrated under both wavelength spacing settings, with only the change in switch state varied from one setting to the other.

Two SFL applications were then demonstrated. The first consisted in measuring the chromatic dispersion inside various lengths of SMF and a DCF module using the time-of-flight measurement method. The results were compared to the traditional phase-shift method, and various conclusions were taken. The two methods shows very good agreement and the percent differences were within -1.23 and 1.13%. The technique could be improved upon by averaging the measurements over several different measures, and using a sampling oscilloscope of greater bandwidth for example. The ease of use and rapidity of the method makes it readily applicable within the industry. The SFL flexibility also increases the measurement precision and offers the possibility of measuring smaller dispersion amounts with the greatest wavelength spacing. More HiBi fiber stages in the FLM of the SFL could provide for more wavelength spacings, and thus even greater measurement capabilities.

The second application enabled us to enter the new emerging and very promising field of Microwave Photonics. In this case, the SFL provided for the optical carriers of the electrical RF signal being processed. Greater source flexibility consequently increases the resulting microwave filter tunability. The two possible wavelength spacings of the SFL provided for two possible filter FSRs. Overall, four FSRs were demonstrated using two different dispersive elements. Reconfiguration was limited but still possible through polarization state controllers and SOA bias current of the SFL. The best filter

contrast obtained was greater than 35dB, and proved that more filter taps and better peak apodization generates better filter characteristics.

6.1 Towards better Optical Instrumentation, Sensing, and Photonic Filtering

Future applications of multi-wavelength sources will require higher and better controlled output peak powers, offer an increased number of peak wavelengths and flexibility in terms of wavelength spacing, and present a means to direct and change at will the various output modes. Once this is achieved, the applications will become numerous. For example, the time-of-flight chromatic dispersion measurement technique investigated in this thesis would be more precise and reliable if the multi-wavelength source is made more stable and more flexible. Knowing exactly where the various lasing peaks occur and being able to change the wavelength step precisely, and at will, is very important for the measurements to be accurate. Larger wavelength spacings would make the measurement of small amounts of dispersion possible, while smaller wavelength spacings would give precise measurements for very long fiber lengths (50km and up). The development of even faster sampling oscilloscopes and more precise optical spectrum analyzers will make such measurement terribly easy to perform in the near future. Any technician in the field will be able to know exactly how much dispersion a fiber spool presents and then be able to compensate for the phenomena through the use of specially designed fiber gratings, for example.

Next generation microwave filters will no longer be made of bulk, bandwidth restrained electrical RF circuits sensitive to electromagnetic interferences. Photonics will provide for a means to readily process the RF signal in the optical domain instead, and relax the analog-to-digital resolution needed in many applications, thereby reducing the overall costs of such applications, and offer much more flexibility.

The work done in this thesis opens the way towards more research in the field of multi-wavelength tunable lasers and their applications, and offers several ways to progress upon the proposed SFL design. Such improvements will enable the optimization of many applications like the ones demonstrated in this thesis. This process

cannot be accomplished, however, without a thorough understanding of the various applications at hand. The two examples treated and reviewed have clearly revealed, for example, how large bandwidth and contrast, wavelength spacing, and peak power control as well as stability, are of capital importance in designing tunable MWSs.

Appendix A

A.1 Theory on Fiber Loop Mirrors (Reflectors)

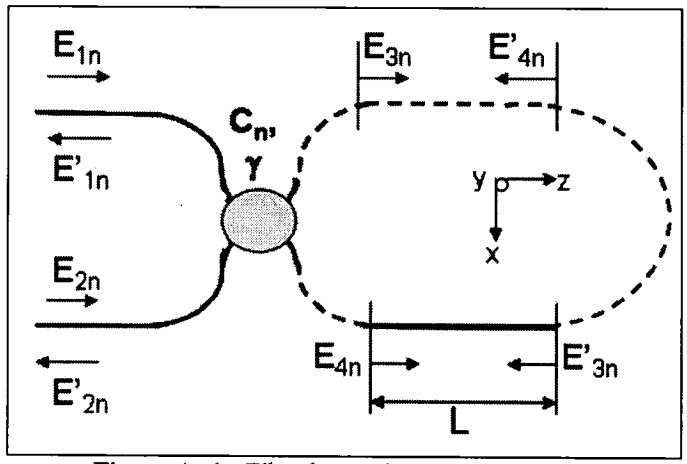

Figure A- 1: Fiber loop mirror representation.

Figure A-1 represents a schematic of a fiber loop mirror. The input fields E_{1n} and E_{2n} enter the coupler via ports one and two respectively. These are transmitted by the coupler and exit at ports 3 and 4 in the form of fields E_{3n} and E_{4n}. The n represents the x and y directed field components. The loop may be viewed as a straightened length of fiber along the z-axis, with a certain attenuation and birefringence either arising from fiber bends and twists, or from optical components inserted in the loop. The two fields E_{3n} and E_{4n} travel in opposite directions inside the loop and the x and y field components thus experience different optical path lengths and attenuations. After traveling inside the loop, E'_{3n} and E'_{4n} are finally re-coupled and exit the coupler in the form of E'_{1n} and E'_{2n}. Each step can be modeled through the use of equivalent transmission and reflection matrices, or Jones matrices.

From coupled-mode theory, E_{3n} and E_{4n} may be derived from the input fields:

$$\begin{pmatrix} E_{3n} \\ E_{4n} \end{pmatrix} = (1-\gamma)^{1/2} \begin{pmatrix} (1-C_n)^{1/2} & jC_n^{1/2} \\ jC_n^{1/2} & (1-C_n)^{1/2} \end{pmatrix} \begin{pmatrix} E_{1n} \\ E_{2n} \end{pmatrix} \qquad (1)$$

where C_n represents both the x and y coupling coefficients, and γ is the excess loss coefficient of the coupler [A.1].

The loop may then be represented as equivalent Jones matrices J_A and J_C, for both the anticlockwise and clockwise transmission respectively. For reciprocal paths, J_A is the

transpose of J_C. The clockwise propagation in the loop occurs for E_{3n}, which is assumed to experience a change in its x-direction before entering the loop, as exemplified in figure A-1. Hence, if the phase component is ignored, E'_{3n} may be expressed as:

$$\begin{pmatrix} E'_{3x} \\ E'_{3y} \end{pmatrix} = \begin{pmatrix} J_{xx} & J_{xy} \\ J_{yx} & J_{yy} \end{pmatrix} \begin{pmatrix} -E_{3x} \\ E_{3y} \end{pmatrix} e^{-\alpha L} \tag{2}$$

where $\begin{pmatrix} J_{xx} & J_{xy} \\ J_{yx} & J_{yy} \end{pmatrix}$ is the Jones transmission matrix J_C and α is the absorption coefficient of the fiber length [A.1].

E_{4n}, on the other hand, travels inside the loop before having a change in its x-direction. The input to port 3 of the coupler, E'_{4n}, thus becomes:

$$\begin{pmatrix} -E'_{4x} \\ E'_{4y} \end{pmatrix} = \begin{pmatrix} J_{xx} & J_{yx} \\ J_{xy} & J_{yy} \end{pmatrix} \begin{pmatrix} E_{4x} \\ E_{4y} \end{pmatrix} e^{-\alpha L} \tag{3}$$

where the Jones matrix is the transpose of J_C.

E'_{3n} and E'_{4n} then re-enter the coupler, and the final output fields may be expressed as:

$$\begin{pmatrix} E'_{1n} \\ E'_{2n} \end{pmatrix} = (1-\gamma)^{1/2} \begin{pmatrix} (1-C_n)^{1/2} & jC_n^{1/2} \\ jC_n^{1/2} & (1-C_n)^{1/2} \end{pmatrix} \begin{pmatrix} E'_{4n} \\ E'_{3n} \end{pmatrix} \tag{4}$$

Combining all the above equations lead to one single matrix, which may be expressed in terms of two 2x2 symmetric reflection matrices, J_{11} and J_{22}, and two 2x2 transmission matrices, J_{21} and J_{12}:

$$\begin{pmatrix} E'_{1x} \\ E'_{1y} \\ E'_{2x} \\ E'_{2y} \end{pmatrix} = (1-\gamma)e^{-\alpha L} \begin{pmatrix} J_{11} & J_{21} \\ J_{12} & J_{22} \end{pmatrix} \begin{pmatrix} E_{1x} \\ E_{1y} \\ E_{2x} \\ E_{2y} \end{pmatrix} \tag{5}$$

where:

$$J_{11} = \begin{pmatrix} a & e \\ e & b \end{pmatrix},\ J_{21} = \begin{pmatrix} c & h \\ g & d \end{pmatrix},\ J_{12} = \begin{pmatrix} c & g \\ h & d \end{pmatrix},\ J_{22} = \begin{pmatrix} a & f \\ f & b \end{pmatrix}, \text{ and}$$

$$a = -2j(1-C_x)^{1/2} C_x^{1/2} J_{xx}$$

$$b = 2j(1-C_y)^{1/2} C_x^{1/2} J_{yy}$$

$$c = (2C_x - 1)J_{xx}$$

$$d = (1-2C_y)J_{yy}$$

$$e = j\left[C_x^{1/2}(1-C_y)^{1/2}J_{xy} - (1-C_x)^{1/2}C_y^{1/2}J_{yx}\right]$$

$$f = j\left[C_y^{1/2}(1-C_x)^{1/2}J_{xy} - (1-C_y)^{1/2}C_x^{1/2}J_{yx}\right]$$

$$g = (1-C_x)^{1/2}(1-C_y)^{1/2}J_{xy} + C_x^{1/2}C_y^{1/2}J_{yx}$$

$$h = -\left[C_x^{1/2}C_y^{1/2}J_{xy} + (1-C_x)^{1/2}(1-C_y)^{1/2}J_{yx}\right]$$

Power reflection and transmission coefficients R_{qq} and T_{pq} (p and q = 1,2) are found by using the following relations:

$$R_{qq}(\tilde{E}_q * E_q) = (1-\gamma)^2 e^{-2\alpha L}(\tilde{J}_{qq}E_q) * (J_{qq}E_q), \text{ and} \tag{6}$$

$$T_{pq}(\tilde{E}_p * E_p) = (1-\gamma)^2 e^{-2\alpha L}(\tilde{J}_{pq}E_p) * (J_{pq}E_p) \tag{7}$$

Several assumptions may simplify the above relations. For example, if the coupling coefficients $C_x = C_y = C$ and the attenuation factor is the same for both x and y directed fields, we may use conservation of energy to obtain the following relations if the Jones loop matrices are reciprocal:

$$|J_{xx}|^2 = |J_{xx}|^2 \text{ and } |J_{xy}|^2 = |J_{yx}|^2 \tag{8}$$

Then, reflectivity and transmissivity may be expressed as:

$$R = R_{11} = R_{22} = (1-\gamma)^2 e^{-2\alpha L} C(1-C)J \tag{9}$$

$$T = T_{12} = T_{21} = (1-\gamma)^2 e^{-2\alpha L}\left[1 - C(1-C)J\right] \tag{10}$$

where $J = 2(|J_{xx}|^2 + 1) - (J_{yx} * J_{xy} + J_{xy} * J_{yx})$

If the final Jones matrix is symmetric, Jxy=Jyx, $\mathbf{J} = 4|J_{xx}|^2$, and birefringence is equivalent to one waveplate of retardation angle ϕ oriented at angle θ [1], for which the equivalent Jones matrix takes the form of [A.2]:

$$J_{xx} = e^{j\phi}\sin^2\theta + \cos^2\theta,\ J_{yy} = e^{j\phi}\cos^2\theta + \sin^2\theta,\ J_{xy} = J_{yx} = (e^{j\phi} - 1)\sin\theta\cos\theta$$

We may also express the total loss as [A.1]:

$$A = 1 - R - T = 1 - (1-\gamma)^2 e^{-2\alpha L} \tag{11}$$

From these, we notice that maximum reflection depends on the loss of the fiber, the coupler splitting ratio and the birefringence of the loop. If birefringence appears as a half wave retardation waveplate with a fast axis at 45°, the Jones matrix is symmetric and J_{xx} is zero; reflection is thus a minimum and transmission is at a maximum. On the other

hand, maximum reflection, and thus minimum transmission, occurs when $J_{xx} = 1$ for a 50/50 coupling ratio [A.1].

The wavelength response of the fiber loop mirror will not only depend on the birefringence in the loop, but also on the spectral characteristics of the coupler [A.2]. The coupling coefficients of the coupler, for example, usually increase with wavelength. Its polarization dependence is modeled by a polarization difference δ equal to [A.2]:

$$\delta = (C_x - C_y)L \tag{12}$$

which is wavelength insensitive. If γ, the loss coefficient of the coupler, is also independent of wavelength, the transmission power of the coupler will vary with coupler polarization difference. Since polarization direction rotates with fiber twist angle, the coupling coefficients may vary accordingly if the coupler itself is slightly twisted or elongated [A.2]. Hence, generally speaking, if θ is non-zero, the equivalent loop mirror waveplate retardation angle ϕ will vary with wavelength as well [A.2]. For sake of simplicity, let us assume that the coupler is not twisted, and retardation angle is wavelength insensitive.

Then the orthogonal components of a field of wavelength λ acquire a relative phase difference upon traveling in the loop:

$$\Delta\varphi = \frac{2\pi}{\lambda} L(|n_o - n_e|) \tag{13}$$

where n_o and n_e are the fast and slow axis effective refractive indices of the fiber [A.1]. Assuming the phase difference is not a function of wavelength, the loop will appear as a half wave retarder when this difference is an odd multiple of π, and transmission reaches a maximum. On the other hand, if this difference is an even multiple of π, the loop behaves as a full wave retarder, the birefringence has no effect and the reflection is maximized [A.1,A.2]. The effective orientation angle θ of the retardation axis is also important in determining the absolute level of minimum reflectivity. If this angle is an even multiple of $\pi/2$, reflectivity is at a maximum, and if it is an odd multiple of $\pi/4$, reflectivity is zero.

Appendix A References

A.1 D. B. Mortimore, "Fiber loop reflectors," *J. Lightwave Technology*, vol. 6, no. 7, pp. 1217-1224, July 1988.

A.2 K. Morishita, K. Shimamoto. "Wavelength-selective fiber loop mirrors and their wavelength tunability by twisting," *J. of Lightwave Technology*, vol. 13, no.11, pp. 2276-2281, November 1995.

Appendix B

B.1 Chromatic Dispersion Application codes

B.1.1 Group-Delay data analysis example

The following code performs data fit to group delay recovered from CSA as a function of peak wavelength and then evaluates dispersion as function of lambda (ps/nm) using differentiation of data fit.

```
%import measures: accumulated group delay vs
peak wavelength
%example data:
%1.6nm results:
lambda1=[1536.87
1538.46
1539.96
1541.58
1543.14
1544.7
1546.29
1547.88
1549.41
1551];%nm

T1=[0
-1070.1
-2060.08
-3154.28
-4212.38
-5262.48
-6336.58
-7434.78
-8476.88
-9587.08]; %ps

% 3.2nm results
lambda2=[1547.76
1550.92
1554.04
1557.24
1560.4];
T2=[0
-2214.4
-4408.8
-6663.3
-8937.8];

%Analysis of 1.6nm results----------
%fit data to quadratic
 p1=polyfit(lambda1,T1,2);
 f1=polyval(p1,lambda1);

%plot fit and points
figure(1)
plot(lambda1, T1, 'o', lambda1,f1,'-'); grid on;
hold on;

%evaluate DL=dT/dlambda
k1 = polyder(p1);
DL1 = polyval(k1,lambda1);

%plot DL
figure(2)
plot(lambda1,DL1);grid on
hold on;

%slope and offset of DL
en1 =length(DL1);
Slope1 = (DL1(en1)-DL1(1))./(lambda1(en1)-
lambda1(1))
os1=DL1(5)- Slope1*lambda1(5)

%----------
%Analysis of 3.2nm results: same procedure

%fit data to quadratic
 p2=polyfit(lambda2,T2,2);
 f2=polyval(p2,lambda2);

%plot fit and points
figure(3)
plot(lambda2, T2, 'o', lambda2,f2,'-'); grid on;
hold on;

%evaluate DL=dT/dlambda
k2 = polyder(p2);
DL2 = polyval(k2,lambda2);

%plot DL
figure(4)
plot(lambda2,DL2);grid on
```

```
hold on;

%slope and offset of DL
en2 =length(DL2);
Slope2 = (DL2(en2)-DL2(1))./(lambda2(en2)-
lambda2(1))
os2=DL2(5)- Slope2*lambda2(5)

%-----------------------------------------------------
---------
%Average all results together to have Averaged
Slope and Offset:

AvgDL_S= (Slope1+Slope2)./2

AvgDL_Os= (os1+os2)./2

lambda=[1535:0.2:1570];%put overall
wavelength range
Overall_DL = AvgDL_S.*lambda + AvgDL_Os;

%plot final figure with all results:
figure(5)
plot(lambda1, DL1,'x',lambda2,
DL2,'o',lambda,Overall_DL,'-');grid on;
xlabel('Wavelength(nm)')
ylabel('DL(ps/nm)')
title('DL measured in Sample')
clear all;
```

B.1.2 Mid-Wave data analysis example

The following program codes performs Best-fit line algorithm once the DL (ps/nm) are calculated with their corresponding mid-wavelength points.

```
%program does best-fit line algorithm of DL
(ps/nm)
%data taken from measured time delays between
consecutive peaks/wavelength spacing
%input DL and mid-wavelength into program
%------------------------------
% example data: Sample B:
%Full data combining 1.6nm and 3.2nm
measures:
 lambda=[1540.467271
 1541.3
 1542.026669
 1543.570316
 1544.34
 1545.113963
 1546.704865
 1547.44
 1548.280015
 1549.839413
 1550.56
 1551.430315
 1552.989713
 1553.7
 1554.53336
 1556.124262
 1556.82
 1557.699412
 1559.96]; %nm
 dl=[165.3944069
166.5669156
168.7698029
171.3663163
167.8682143
168.3880091
170.4835095
169.5699038
174.3002889
172.1299497
172.7814744
173.0280291
176.5592133
174.3994304
175.8718902
178.1170682
175.0336076
179.389328
180.4891987 ];%ps/nm

%-----------------------
%plot data points:

plot(lambda,dl,'go'), grid on;hold on;

%perform bestfit algorithm:
N = length(dl);
k1=0;k2=0;k3=0;k4=0;

for i=0:N-1
k1 = k1 + lambda(i+1);
k2 =k2+dl(i+1);
k3 = k3 + lambda(i+1)*lambda(i+1);
k4 = k4+lambda(i+1)*dl(i+1);
end
```

```
%output best-fit line's slope and offsets
S = (N*k4-k1*k2)/(N*k3-k1*k1)
offset = k2/N - S*(k1/N)

%generate line with calculated slope and offset:
l=[1535:0.2:1565];
bestfit = S*l + offset;

%plot final bestfit line over data points:
plot(lambda, bestfit,'r');grid on;
xlabel('Wavelength(nm)');
ylabel('DL(ps/nm)');
title('Measured DL for Sample B (mid-wave
analysis)');
clear all;
```

B.1.3 Phase-Shift data analysis example

This code performs the analysis of the Phase-Shift measurements taken for sample A, together with curve fitting algorithm and differentiation in order to obtain its DL profile as a linear curve with a slope and an offset.

```
%group delay collected at 500MHz
%Sample A

M=[ 2175.17   2203.592   2223.828   2223.828   2253.728
    2253.728  2274.191   2300.226   2300.226   2312.504
    2343.541  2343.541   2368.097   2388.561   2388.561
    2413.685  2413.685   2436.309   2458.705   2458.705
    2487.809  2512.252   2512.252   2532.261   2555.68    2555.68
    2581.26   2581.26    2594.675   2623.892   2623.892
    2650.381  2673.346   2673.346   2690.968   2719.73    2719.73
    2753.154  2753.154   2759.862   2789.193   2789.193
    2812.385  2837.055   2837.055   2865.704   2882.871
    2882.871  2914.817   2914.817   2927.663   2958.473
    2958.473  2975.071   3009.973   3009.973   3035.893
    3054.197  3054.197   3081.595   3081.595   3093.191
    3130.481  3130.481   3146.738   3172.431   3172.431   3209.72
    3225.409  3225.409   3251.444   3251.444   3268.951
    3304.194  3304.194   3320.338   3344.894   3344.894
    3371.724  3401.283   3401.283   3421.064   3421.064
    3442.665  3473.019   3473.019   3484.729   3523.269
    3523.269  3547.484   3561.922   3561.922   3595.801
    3595.801  3621.494   3641.503   3641.503   3665.377
    3697.096  3697.096   3713.694   3742.343   3742.343
    3768.719  3768.719   3793.275   3820.56    3820.56
    3837.613  3861.715   3861.715   3891.955   3910.373
    3910.373  3952.437   3952.437   3961.759   4003.141
    4003.141  4015.419   4042.249   4042.249   4070.671
    4091.362  4091.362   4127.969   4127.969   4140.929   4172.08
    4172.08 4191.861   4220.737   4220.737   4251.206   4268.031
    4268.031  4302.365   4302.365   4318.281   4347.385
    4347.385  4359.89    4391.268   4391.268   4424.237   4446.52
    4446.52   4484.036   4484.036];
lambda=[1540.4:0.2:1570];

m=length(M);
%fit to quadratic
p= polyfit(lambda,M,2);
%evaluate quadratic
```

```
f = polyval(p,lambda);
%plot fitted curve with data points
plot(lambda,M,'o',lambda,f,'-')
%differentiate group delay quadratic
k = polyder(p);
DL = polyval(k,lambda);

%slope and offset of DL curve
en =length(DL);
Slope = (DL(en)-DL(1))./(lambda(en)-lambda(1))
os=DL(5)- Slope*lambda(5)
%plot DL curve obtained
figure(2)
plot(lambda,DL);grid on
clear all;
```

B.2 Microwave filter transfer function simulation codes

B.2.1 Simulations only employing input lasing peaks and length of SMF

The following code example performs simple simulations of microwave filter responses with individual peaks, either power equalized or not, using a given length of SMF fiber with dispersion D = 18ps/nm-km

```
%3.2nm input spectra: 7 peaks
osa1=[ .....];
lambda1=[1529.128:0.052803:1581.931];

%1.6nm input spectra, 13 peaks
osa2=[....];
lambda2=[1525.548:0.036778:1562.326];

% plot relevant input spectra:
figure(1)
plot(lambda,osa);grid on;
title('3.2nm Wavelength Spacing Input Spectra');
ylabel('Power(dBm)');
xlabel('Wavelength(nm)');

%set to relevant input spectra
osa=osa1;
lambda=lambda1;

%find peaks and corresponding lasing wavelengths,
the distances between peaks will then give the %time
delay
%for each peak depending on beta of dispersive
media (ps/nm)
%each peak power has to be changed in terms of
electrical power

%osa treatement: find peaks and delta-lambda-------
-------
%cutoff power: -25dBm
k=1;
for i=1:1:length(osa)
   if osa(i)<(-25)
      osa(i)=-25;
      gap(k)=i;  %all places set to -50
      k=k+1;
   end
end
%cut osa into segments with only one peak and
place in columns of V. note that number of
%columns must be changed
%with corresponding number of peaks in spectra
l=0;
for i=1:1:7
   for k=1:1:1001
      V(k,i)=-50;
   end
end

g=length(gap);
for i=1:1:(g-1)
   ini=gap(i);
   fin=gap(i+1);
   d=fin-ini;;
   if (d > 1)
```

```
    l=l+1;
    for k=ini:1:fin
    V(k,l)= osa(k);
    end
  end
end
[m,n]=size(V);

%find each peak with corresponding wavelength
for i=1:1:n
  p=max(V(1:m,i));
  wl(i)=find(p==V(1:m,i));
  peaks(i)=p;
end

%find distances between each wavelengths and each
mid wavelengths

nofpeaks = length(wl);
for i=1:1:nofpeaks-1
  wl1=wl(i);
  wl2=wl(i+1);
  delta(i) = lambda(wl2)-lambda(wl1);
end

for i=1:1:nofpeaks
    peak_wl(i)=lambda(wl(i));
end

%Dispersion----------------------------
%length of fiber:
L=30; %km
beta=18*L;

%Filter Response
R=1; %detector responsitivity

%change peak powers in V
for i=1:1:length(peaks)
  pps(i)=(10.^((peaks(i))./10)).*1e-3;

end

%time delays between pulses
for i=1:1:length(peak_wl)
  total_delta(i)=peak_wl(i)-peak_wl(1);
  delay(i)=total_delta(i).*beta; %in ps
end

%frequency range
f=2*3.1416*[0:0.000005e9:2e9];%Hz
%For AM Extinction Factor: peak_wl is changed in
mid-range depending on input spectra
beta2=((peak_wl(6)+100)^2)*beta/(2*3.1416*3e8*1e
9/1e12);%ps2

%Response: Note that this was adjusted if the
response needed was either with equal powers or
%not, and with desired number
%of peaks.

%aH=R.*abs(pps(1) + pps(2).*exp(-j*f*(1e-
12).*delay(2)) + pps(3).*exp(-j*f.*(1e-
%12).*delay(3))+ pps(4).*exp(-j*f.*(1e-
12).*delay(4))+ pps(5).*exp(-j*f.*(1e-
12).*delay(5))+ %pps(6).*exp(-j*f.*(1e-
12).*delay(6))+ pps(7).*exp(-j*f.*(1e-
12).*delay(7)));%+ pps(8).*exp(-%j*f.*(1e-
12).*delay(8))+ pps(9).*exp(-j*f.*(1e-
12).*delay(9))+ pps(10).*exp(-j*f.*(1e-
%12).*delay(10))+ pps(11).*exp(-j*f.*(1e-
12).*delay(11))+ pps(12).*exp(-j*f.*(1e-
%12).*delay(12))+ pps(13).*exp(-j*f.*(1e-
12).*delay(13)));

%equal powers:
 aH=R.*abs(pps(5) + pps(5).*exp(-j*f*(1e-
12).*delay(2)) + pps(5).*exp(-j*f.*(1e-
12).*delay(3))+ pps(5).*exp(-j*f.*(1e-
12).*delay(4))+ pps(5).*exp(-j*f.*(1e-
12).*delay(5))+ pps(5).*exp(-j*f.*(1e-
12).*delay(6))+ pps(5).*exp(-j*f.*(1e-
12).*delay(7))+ pps(5).*exp(-j*f.*(1e-
12).*(delay(7)+delay(1)))+ pps(5).*exp(-j*f.*(1e-
12).*(delay(7)+delay(2)))+ pps(5).*exp(-j*f.*(1e-
12).*(delay(7)+delay(3)))+ pps(5).*exp(-j*f.*(1e-
12).*(delay(7)+delay(4)))+ pps(5).*exp(-j*f.*(1e-
12).*(delay(7)+delay(5)))+ pps(5).*exp(-j*f.*(1e-
12).*(delay(7)+delay(6))));

%changed for 13 peak input example with equal
powers
 %+ pps(5).*exp(-j*f.*(1e-12).*(delay(8)))+
pps(5).*exp(-j*f.*(1e-12).*(delay(9)))+
%pps(5).*exp(-j*f.*(1e-12).*(delay(10)))+
pps(5).*exp(-j*f.*(1e-12).*(delay(11)))+
pps(5).*exp(-%j*f.*(1e-12).*(delay(12)))+
pps(5).*exp(-j*f.*(1e-12).*(delay(13))));

%In log mag:
Hff=20.*log10(aH);

%Normalization:
maxHff=max(Hff);
Hfn=Hff-maxHff;

%AM extinction curve in log mag:
ch=20*log10(cos(beta2*((1e-12).^2)*(f.^2)/2));
%Plot results:
figure(2)
plot(f/(2*3.1416),Hfn,f/(2*3.1416),ch); grid on;
xlabel('Frequency (Hz)', 'FontSize',12);
```

```
ylabel('Normalized filter response (dB)',
'FontSize',12);
title('Simulated Frequency Response (3.2nm source
at 180mA, 30km SMF delay,equal powers,13 peaks)',
'FontSize',12);
h=legend( 'SSB Simulated Frequency Response',
'AM Extinction Factor',3);
clear all;
```

B.2.2 Simulations employing whole input spectra and dispersion profile

This code performs simulations from whole input spectra for sample D and B with dispersion profiles from Phase-shift (PS) measurements done in section IV.

```
%3.2nm 7 peaks:
osa=[...];
lambda=[1529.128:0.052803:1581.931];
% 1.6nm 13 peaks:
% osa=[....];
% lambda=[1525.548:0.036778:1562.326];

% Plot input spectra
% figure(1)
% plot(lambda,osa);grid on;
%-------------------------
%dispersion-from dl info with 33.7km smf: sample D
% from ps data
s=1.8907;
os=-2.338e3;

%data ps 10km: sample B
% s=0.5866;
% os=-736.7838;


R=1; %detector responsitivity

%change osa powers in V
for i=1:1:length(osa)
        osae(i)=(10.^((osa(i))./10)).*1e-3;
end
%set midlambda for AM extinction Factor
midlambda= 1552; %3.2nm example
%Beta2 term:

beta2=((midlambda+90)^2)*(midlambda*s+os)/(2*pi
*3e8*1e9/1e12);

%Filter Response:
r=1;
 for f=0:0.005e9:10e9 %Hz
        H=0;
        for i=1:1:length(osa)
         deltawl=lambda(i)-lambda(1);
         H=H+osae(i).*exp(-j*2*pi*f*(1e-
12).*(lambda(i)*s+os).*deltawl);
          end
         Hf(r)=H;
        r=r+1;
end

f=[0:0.005e9:10e9];%Hz
%AM Factor:
ch=20*log10((cos(beta2*((1e-
12).^2)*((2*pi*f).^2)/2)));
%Filter Response in log mag
aH=R.*abs(Hf);
Hff=20.*log10(aH);
% Normalization
maxHff=max(Hff);
Hfn=Hff-maxHff;

%plot everything
figure(2)
plot(f,Hfn,f,ch); grid on;
xlabel('Frequency (Hz)', 'FontSize',12);
ylabel('Normalized Filter Response (dB)',
'FontSize',12);
title('Simulated Frequency Response (3.2nm
spacing source at 180mA and Sample D
dispersion profile)', 'FontSize',12);
h=legend( 'SSB Simulated Frequency Response',
'AM Extinction Factor',3);
 clear all;
```

Appendix C: Published Articles

1) Article to be published in *SPIE Proceedings, vol.5970, 79501X, 2005.*

Chromatic dispersion measurements of optical fiber based on time-of-flight using a tunable multi-wavelength semiconductor fiber laser

Véronique Pagé, Lawrence R. Chen

Photonics Systems Group, Department of Electrical and Computer Engineering, McGill University, 3480 University Street, Montreal (Québec), H3A 2A7, Canada

ABSTRACT

We have developed a tunable multi-wavelength semiconductor fiber laser (SFL) for chromatic dispersion measurements of optical fiber based on the time-of flight method. The SFL incorporates a programmable high-birefringence fiber loop mirror to select the separation of the lasing wavelengths between 3.2 nm and 1.6 nm. The SFL emits 5 wavelengths with an average power of 11.96 dBm per wavelength and 11 wavelengths with an average power of 18.35 dBm per wavelength, for separations of 3.2 nm and 1.6 nm respectively, all within the C-band. The linewidth of each oscillating wavelength resides in the 0.16 nm - 0.28 nm range, the signal-to-noise ratio varies between 33.5 dB and 39.2 dB, and the uniformity of the output power is within 3.2 dB. Stability measurements for each lasing peak show a wavelength deviation of +/-0.09nm/hour and a power variation of +/-0.90 dB/hour. Results from time-of-flight measurements are compared with standard phase-shift techniques and the differences analyzed. The percent error between the two methods is better than -0.73 to 1.13% for measurements on various standard optical fiber lengths. The time-of-flight method is easier and faster to use for the characterization of sufficiently dispersive media such as deployed fiber spools. Our tunable laser provides a simple low cost solution for such measurement applications. The tunable nature of our SFL source also provides the following advantages for chromatic dispersion measurements: (1) greater precision can be obtained since two independent measurements (one at each wavelength separation) can be performed using a single optical source and (2) there is increased flexibility since the wavelength spacing can be tailored for a specific situation; shorter lengths benefiting from larger wavelength separations.

Keywords: Optical fiber dispersion, semiconductor fiber lasers, optical fiber measurement applications, Time-of-Flight, HiBi Fiber Loop mirror.

I. INTRODUCTION

The recent development of wavelength division multiplexed (WDM) optical systems was a major step in meeting the ever-growing bandwidth demand. Further increasing network capacity can be accomplished either by adding more wavelengths or by modulating the channels at higher rates. As the data or channel rates increase, however, nonlinear effects and chromatic dispersion issues become increasingly important. These may cause severe signal degradation if not compensated for or properly controlled. Accurate measurement of chromatic dispersion is thus an important step towards managing such phenomena. Many measurement methods have been proposed, but the ultimate solution should ideally be simple, fast, low cost, and permit the measurement of long, already-deployed fiber links.[1]

There are three principal methods recognized by the International Telecommunications Union (ITU) for measuring chromatic dispersion: interferomteric, phase-shift, and time-of-flight. In the first approach, an interferometer is employed, where one arm is the fiber under test, and the other arm is the

reference fiber with a well-known group delay profile. The measured cross-correlation will vary according to the time delay between both arms of the interferometer. This technique is very accurate but limited to short lengths of fibers.[1] The phase-shift technique has been predominantly used in the industry by several commercially available chromatic dispersion measurement instruments. In this case, the input signal is amplitude modulated. The phase of the transmitted signal envelope is compared with a reference input signal in order to obtain the group delay. This measurement is performed over a range of different wavelengths, and thus requires a certain amount of time to scan the desired wavelength range. The differential phase-shift technique modulates the input signal both in amplitude and frequency, while scanning over the wavelength range, making the measurement more immediate. It permits the precise measurements of both long as well as short fiber lengths, and passive fiber components such as fiber Bragg gratings. However, this technique relies on a reference signal.[1,3,]

In the time-of-flight (TOF) or pulse-delay method, the chromatic dispersion is derived from the relative temporal group delay experienced by various wavelengths during their propagation through a fiber length. The delay is measured by detecting, recording and processing the differences in propagation time experienced by pulses at various wavelengths. Dispersion can then be obtained for a fixed wavelength or over a desired range. . The optical source must be stable in lasing wavelength and intensity over enough time to complete the measurements. The modulation frequency must also be set such that there is enough time resolution to make the measurements. In this way, a reference channel is not necessary.[1,3] The technique requires that short temporal pulses at multiple known wavelengths be simultaneously launched into the test fiber. A sampling oscilloscope such as a communications signal analyzer (CSA) captures the output signal and the time delay between the consecutive pulses is recorded for each wavelength pulse. The group delay as a function of wavelength can then be obtained by using a least mean square fitting technique, and the dispersion can be calculated by differentiating this curve with respect to wavelength. However, the TOF approach is limited to relatively long lengths of test fibers (several km's) because the delays between the consecutive pulses must be distinguishable on the CSA, requiring a certain amount of cumulative chromatic dispersion.[4] Previous experiments have found that the measurements are possible for lengths of ten's of kilometers of single-mode fiber (SMF), when the temporal separation between the pulses is at least twice their full width half maximum (FWHM).[1,3]

The TOF measurement method is faster than the phase-shift technique since there is no need for wavelength scanning. It is hence an interesting application for the measurement of dispersion in already-deployed fiber links and indeed, many implementations have been proposed in the recent past, including the use of Raman laser sources, superluminescent diodes, or Erbium doped fiber (EDF) lasers filtered with fiber Bragg gratings. The principle sources that degrade the accuracy of the measurements are related to the stability of the input signals (and hence to the optical source used). The above-mentioned approaches suffered from timing jitter and optical triggering instabilities, low power efficiencies, or cross-gain saturation effects and flatness issues. They all required additional expensive equipment as a method to compensate their respective problems.[1]

In this paper, we demonstrate a new and improved tunable multi-wavelength semiconductor fiber laser (SFL) for chromatic dispersion measurements of optical fiber based on the TOF method. We also compare our measurements to those obtained using the conventional phase-shift technique, and the errors are analyzed. The (SFL) proves to offer many advantages over its predecessors since it is fast, simple, relatively low-cost, and yet reliable for such measurements.

II. MULTIWAVELENGTH LASER DESIGN

Figure 1 shows a schematic of the tunable multi-wavelength SFL source, which is similar to the one proposed in Ref. [4]. The semiconductor optical amplifier (SOA) (Alcatel 1901, with a peak small-signal gain of 20.14dB at 1550nm for an input signal power of –25.80dBm, and a polarization sensitivity of 0.4dB) provides the gain; the lasing wavelengths are selected using a comb filter based on a high-birefringence (HiBi) fiber loop mirror (FLM) directly connected to the laser cavity. The filter is employed

in transmission mode in order to eliminate the loss that would have been induced by a circulator, had the filter been used in reflection mode. An isolator is used to ensure unidirectional propagation inside the cavity. The output is extracted using a 3dB coupler.

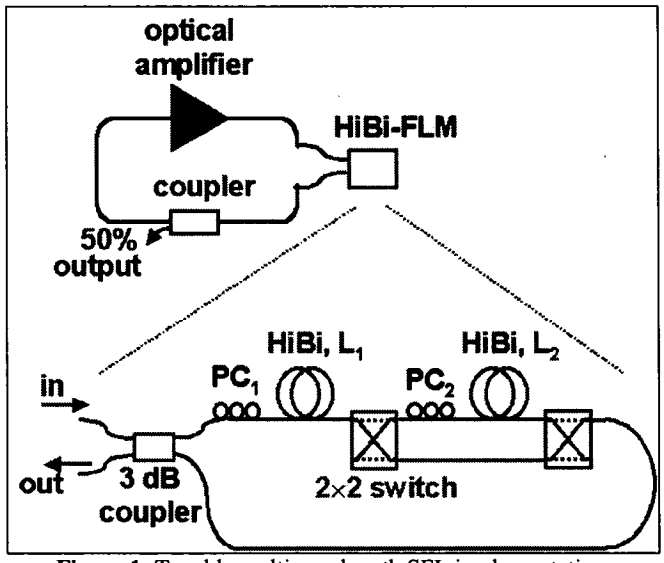

Figure 1: Tunable multiwavelength SFL implementation.

2.1 HiBi-FLM filter design

The principle of the HiBi-FLM is well understood.[4,6,7,8] Briefly, the 3dB coupler splits the input signal in two counter-propagating waves. These travel through the loop and are then recombined by the same coupler. The interference of the waves will either be constructive or destructive, depending on the birefringence of the loop. In this way, the reflection and transmission responses are wavelength-dependent. Since both waves travel through the same optical path, the filter is less sensitive to environmental changes.[4]

Theoretically, assuming no insertion loss in the coupler and identical attenuation constants α for the HiBi fiber and SMF fiber, the transmitted intensity is:

$$T(\lambda) = 1 - \exp(-2\alpha\,(l + L))\cos^2(\delta\phi/2) \qquad (1)$$

where $\delta\phi = 2\pi\Delta nL/\lambda$ is the phase difference between fast and slow propagating waves in the HiBi fiber. λ is the wavelength, L is the length of HiBi fiber, Δn is the fiber birefringence, and l is the length of SMF fiber.

The wavelength spacing between transmitted peaks is given by:

$$\Delta\lambda = \lambda^2/\Delta nL \qquad (2)$$

Varying the length of HiBi fiber L will vary the wavelength spacing. In this way, cascading lengths of HiBi fiber segments interconnected by 2×2 switches provides for this variability without the need for physically altering the laser cavity (i.e. physically adding or removing fiber to change the wavelength spacing). The polarization controllers in the FLM are used to adjust the contrast in the responses. [4,6,7,8]

In our implementation, we use 2 segments of HiBi fiber interconnected by 2×2 switches to chose between two possible wavelength spacings. The HiBi has a measured birefringence of 3.8×10^{-4} at 1550nm and the HiBi segments are equal in length with L set roughly at 1.99m. If the first 2×2 switch is in the cross

state, the wavelength spacing will be approximately 3.2nm; if the switch is in the bar state, the HiBi fiber length doubles to 3.98m and the wavelength spacing is halved and becomes about 1.6nm.[4]

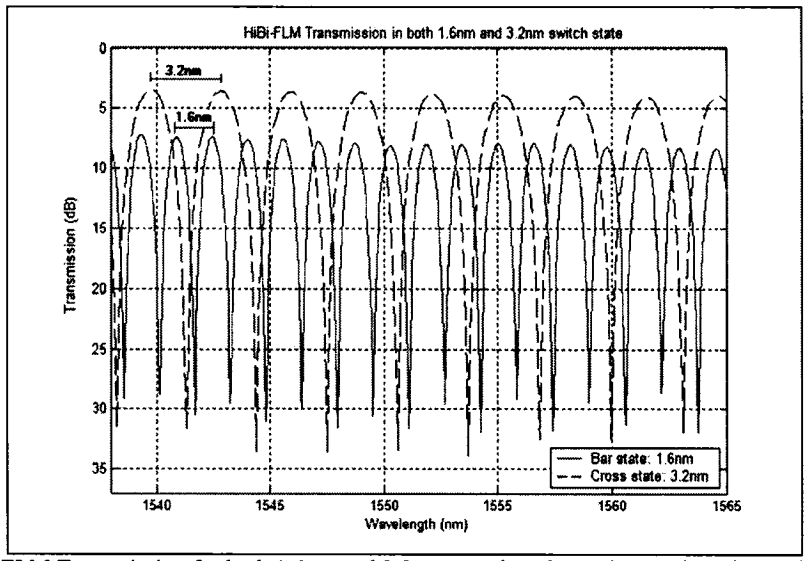

Figure 2: HiBi-FLM Transmission for both 1.6nm and 3.2nm wavelength spacing modes—bar and cross state. All measurements are done with an Optical Signal Analyzer (OSA) (Agilent 86142B) with a sensitivity of −70dBm, and a resolution of 0.06nm.

The insertion loss of the HiBi-FLM depends on the losses induced by each HiBi fiber segment(s), insertion loss from the switches, and from the splices between the HiBi and SMF fibers. Figure 2 shows the filter characteristics of the HiBi-FLM with both switch states. The cross state exhibits a wavelength spacing of approximately 3.2nm, an average contrast of 23.94dB, and an average of 4.01dB insertion loss. For the bar state, the wavelength spacing is 1.6nm with an average contrast of 22.58dB and an average insertion loss of 7.62dB. These characteristics were obtained using optimal polarization controller (PC) settings, independently adjusted for each switch state. A single PC setting giving acceptable transmission profiles for both switch states can also be obtained.

2.2 Source characteristics

Figure 3 presents examples of the laser output for each switch state. Polarization controllers can vary the number of peaks, the lasing wavelengths, as well as the power of each peak. The cross state offers lasing wavelengths in the upper C-band, that is between 1545-1565nm, while the bar state tends to have lasing peaks between 1540-1560nm. We also note that there exists a tradeoff between flatness of the lasing peaks and bandwidth: the best flatness is obtained for the least number of lasing peaks.

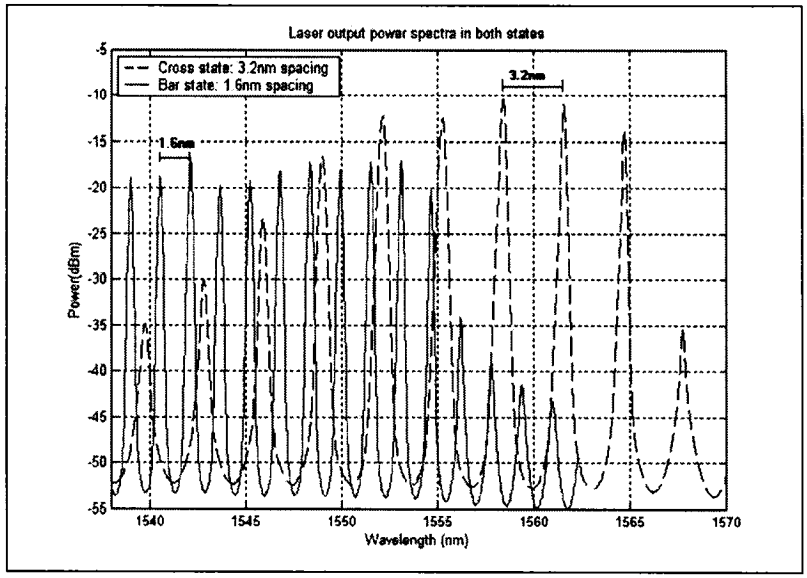

Figure 3: Cross and bar state output power spectra examples. All measurements are done with an Optical Signal Analyzer (OSA) (Agilent 86142B) with a sensitivity of –70dBm, and a resolution of 0.06nm.

The output examples are obtained at a driving current of 180mA. The multi-wavelength source set in the cross state offers 5 lasing peaks at an average power of -11.96dBm, for a total power of -4.83dBm. In this case, the maximum peak excursion is 3.11dB, taken across the 5 peaks offering highest powers, and the signal to noise ratio (SNR) is 39.20dB. Each peak has a linewidth between 0.17 and 0.28nm, all of which were measured using the best possible optical spectrum analyzer (OSA) resolution bandwidth of 0.06nm. Stability tests performed for one hour show a maximum lasing wavelength deviation of +/-0.05 nm and a maximum peak power deviation of +/- 0.59dB. In the bar state, up to 11 lasing lines are obtained with an average power of -18.35dBm, for a total power of -8.06dBm. The maximum peak excursion is 3.19dB, the SNR is 33.55dB, and the linewidths are within 0.17nm and 0.2nm. The maximum lasing wavelength deviation is +/-0.09 nm and the maximum peak power deviation is +/- 0.90dB when measured over one hour.

III. TIME-OF-FLIGHT CHROMATIC DISPERSION MEASUREMENTS

Figure 4 shows the experimental setup used to obtain the TOF measurements using the SFL described in Section 2.2. The laser output is modulated using a Mach-Zehnder electro-optic modulator (JDS Uniphase 10024291) driven by a pulse pattern generator (Anritsu MP1763B) and biased with a DC voltage set between 3.5V and 4.5V. The output pulses had a FWHM of 110ps at a repetition rate of 90.91MHz. The corresponding period is appropriate for measuring dispersion-length products (DL) smaller than 687.5ps/nm in the 3.2nm wavelength spacing mode (with a maximum of 6 peaks and 2.2ns time delay between each peak), or 572.92ps/nm in the 1.6nm wavelength spacing mode (with a maximum of 13 peaks and 0.197ns time delay between each peak)—or 38km and 32km of SMF respectively. Larger DL products may also be measured by simply further decreasing the repetition rate. The polarization controller optimizes the modulator throughput and extinction ratio. A 1% tap is also used in order to monitor the lasing wavelengths with an OSA. Finally, the pulses are launched into the fiber under test and the transmitted signal is measured with an optical sampling module (Tektronix 80C01) and CSA. For test fibers longer than 7km, the transmitted signals are first amplified using an EDFA (INO).

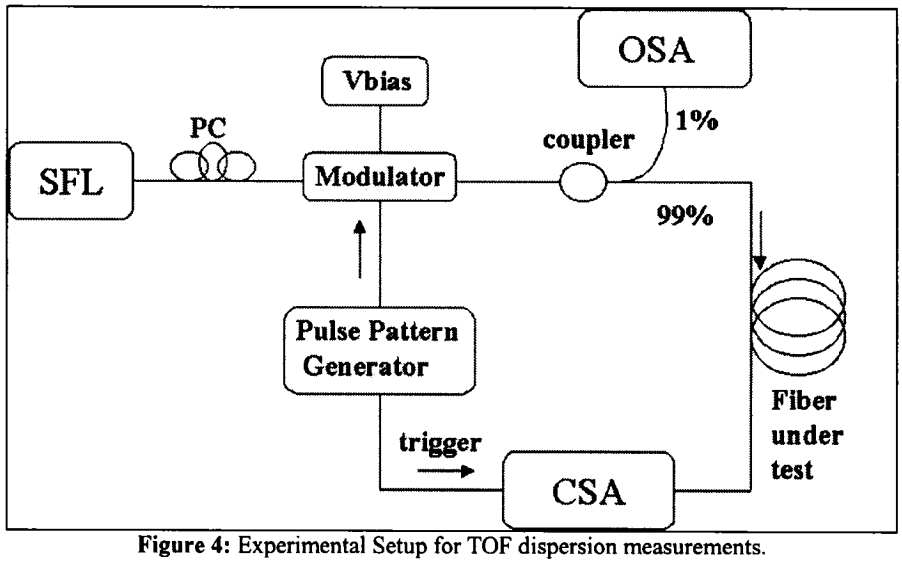

Figure 4: Experimental Setup for TOF dispersion measurements.

Various lengths of SMF were tested (samples A, B, C and D) along with a dispersion compensating module comprising about 6.9km of dispersion compensating fiber (DCF) (sample E). Figure 5 presents the temporal traces obtained for samples B and E. These measurements were obtained by averaging the signal 500 times.

After propagating though a length of fiber, the pulses at the different wavelengths are separated in time and it is thus possible to measure the time delay between neighboring peaks. For the DCF module, the order in which the pulses arrive in time is reversed, and the corresponding delays are thus paired accordingly with the reversed lasing wavelengths. The measured group delay occurring from the first pulse to each of the subsequent ones is plotted against its corresponding lasing wavelength. The ITU has made a series of recommendations for the use of different formulas to calculate the chromatic dispersion from any experimental data, and for specific types of fibers operating in different wavelength regions. These recommendations where thus employed for the measurements here presented. For non-dispersion-shifted single-mode fibers operating in the 1500-1600nm range (Recommendation G.653), the standards recommend fitting the measured group delay per unit length to a quadratic expression.[3] The chromatic dispersion is then obtained by differentiating the group delay with respect to wavelength. If the length tested is not accurately known, the dispersion-length (DL) product as a function of wavelength is thus obtained and represents a more accurate measure, appropriate for the comparisons presented in the next section. The DL product profiles are lines characterized by a certain slope (S) given in ps/nm^2 and a certain offset (OS) in ps/nm. The DL product as a function of wavelength thus fits the corresponding linear equation:

$$DL(\lambda) = S\lambda + OS \qquad (3)$$

Each data set (one for each 1.6nm and 3.2nm wavelength spacing sources) was analyzed individually, and the obtained slopes and offsets were averaged to get the final "Average" DL curve (refer to Table 1 and Figure 6 below).

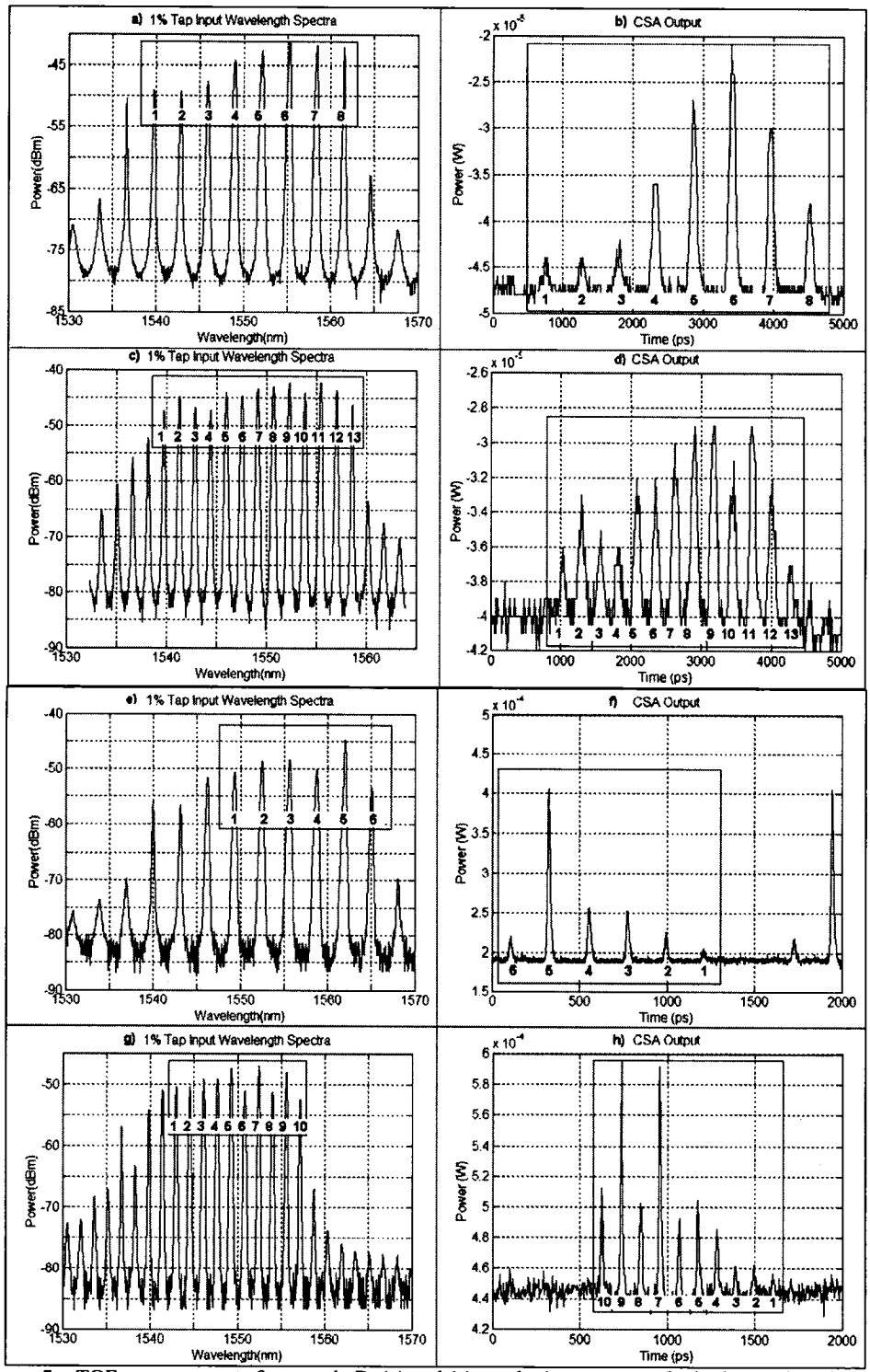

Figure 5: TOF measurements for sample B: (a) and (c) are the input spectra for both wavelength spacing, (b) and (d) are the corresponding CSA output after circulating through sample B test fiber. TOF measurements for sample E: (e) and (g) are the input spectra for both wavelength spacings, (f) and (h) are the corresponding CSA output after circulating through the DCF test fiber. The boxes within each graph identify the relevant lasing modes and time delayed pulses, all numbered to their corresponding peak.

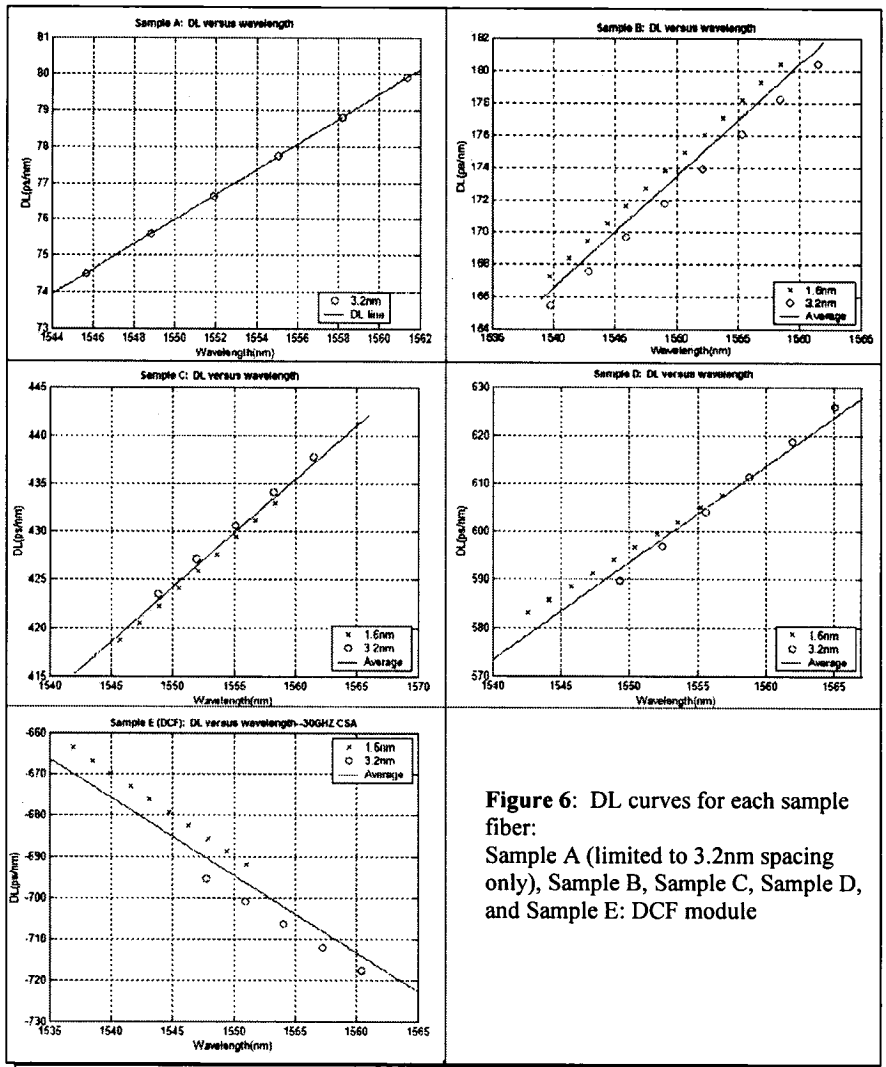

Figure 6: DL curves for each sample fiber:
Sample A (limited to 3.2nm spacing only), Sample B, Sample C, Sample D, and Sample E: DCF module

DL curves for each test fibers	Slopes (ps/nm^2)	Offsets (ps/nm)
Sample A: 3.2nm wavelength spacing	0.3454	-459.3920
Sample B: Average	0.6940	-902.3123
3.2nm spacing	0.7020	-913.5763
1.6nm spacing	0.6861	-891.0483
Sample C: Average	1.1243	-1.3185e3
3.2nm spacing	1.1300	-1.3268e3
1.6nm spacing	1.1186	-1.3103e3
Sample D: Average	2.0141	-2.5283e3
3.2nm spacing	2.3088	-2.9875e3
1.6nm spacing	1.7193	-2.0692e3
Sample E--DCF: Average	-1.8827	2.2237e3
3.2nm spacing	-1.9945	2.4016e3
1.6nm spacing	-1.7709	2.0457e3

Table 1: Slopes and offsets of the corresponding DL curves shown in Figure 6. Samples A to D were measured using a 20GHz CSA, sample E was done with a 30GHz CSA.

IV. COMPARISON BETWEEN TIME-OF-FLIGHT AND PHASE-SHIFTRESULTS

In order to verify the validity of our measurements and evaluate the proposed TOF method, we compare the percent difference in our TOF measurements to those obtained using the phase-shift technique. For this purpose, we use a lightwave component analyzer (Agilent 8703B 4114A00105) where the scanning is performed over a wavelength range similar to the lasing wavelengths of the SFL (i.e. from 1540nm to 1570nm in 0.2nm increments).

Figure 7 presents the DL curves obtained using both the phase-shift and the TOF techniques, together with the percent differences (dotted lines). Table 2 summarizes the slopes and offsets of the DL curves obtained using the phase-shift technique, which can be compared to the TOF values given in Table 1.

The percent differences between the measurements are within -0.73% and 1.13% for samples A through D, except for sample E, the DCF module. This may be explained by the fact that the phase-shift technique only considers the dispersion at modulation frequency of 500MHz. Since the DCF is more frequency sensitive, it is possible that the dispersion slope measured with this method is less accurate. The TOF errors encountered were mainly due to the limited bandwidth of the CSA. As the time delay between the pulses increases, the errors decrease. Averaging the results from 4 different measurements, each averaged in turn using measurements from both wavelength spacings, improves on the precision greatly. This was done using sample B, for which the averaged DL slope obtained via averaging shows a reduction of 10.04% in percent difference of DL slopes (with respect to the DL slope measured with the phase-shift technique) compared to that of the non-averaged measurements. In this case, the percent difference in DL curves calculated at each wavelength is within 0.55%. The maximum slope deviation occurring within these repeated measurements was calculated to be +/-0.09ps/nm^2 with an average repetition error (from the average value) of +/- 14.73%.

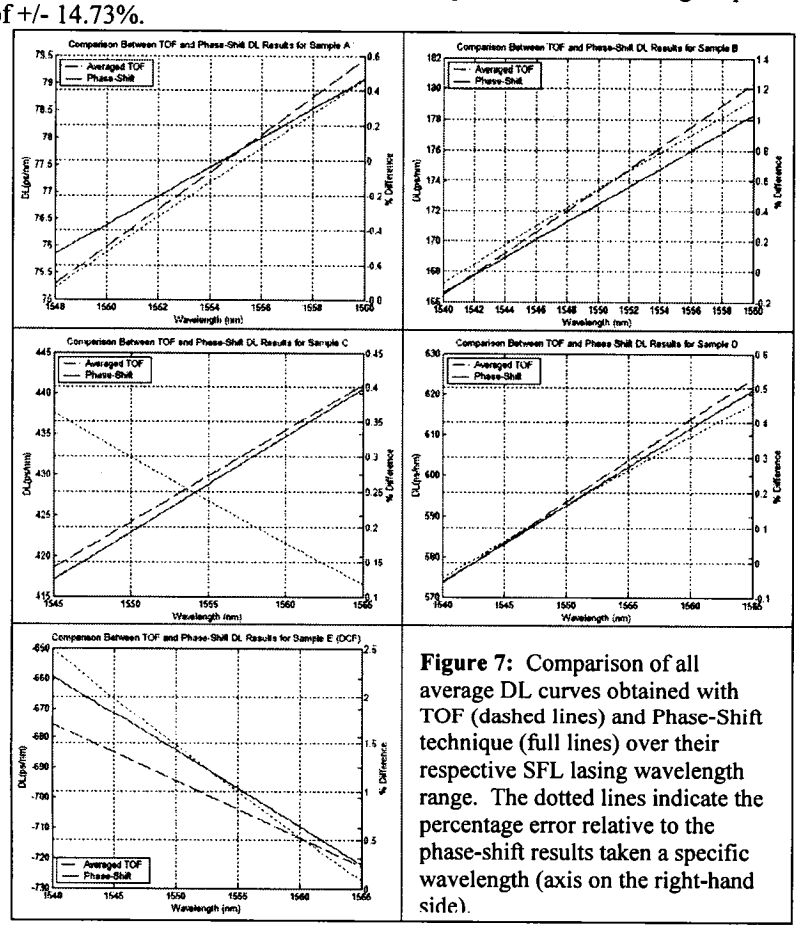

Figure 7: Comparison of all average DL curves obtained with TOF (dashed lines) and Phase-Shift technique (full lines) over their respective SFL lasing wavelength range. The dotted lines indicate the percentage error relative to the phase-shift results taken a specific wavelength (axis on the right-hand side).

Phase-Shift Measurements	Slopes (ps/nm^2)	Offsets (ps/nm)
Sample A	0.2688	-340.2600
Sample B	0.5866	-736.7838
Sample C	1.1740	-1.3968e3
Sample D	1.8907	-2.3380e3
Sample E: DCF	-2.5174	3.2176e3

Table 2: Phase-Shift measurement DL results: slopes and offsets.

It is also important to note that the possibility of making the measurements with both the 1.6nm and the 3.2nm wavelength spacings of the input source increases the flexibility of the process but also provides for generally better precision of the results, as the wavelength bandwidth is increased. Table 3 gives an idea of this advantage by listing the percent difference (again relative to phase-shift measures) between the resulting DL slopes from each independent and averaged TOF readings, in both the 1.6nm and the 3.2nm spacing modes.

	Percent difference between the TOF DL slopes relative to those from the phase-shift method
Sample A: 3.2nm wavelength spacing	28.50%
Sample B: Average	18.31%
3.2nm spacing	19.67%
1.6nm spacing	16.96%
Times 4 averages (both spacing) for sample B	8.27% (a 10.04% decrease)
Sample C: Average	4.23%
3.2nm spacing	3.75%
1.6nm spacing	4.72%
Sample D: Average	6.53%
3.2nm spacing	22.11%
1.6nm spacing	9.07%
Sample E--DCF: Average	25.21%
3.2nm spacing	20.77%
1.6nm spacing	29.65%

Table 3: Percent differences between DL slopes obtained from TOF measures relative to those obtained from phase-shift measures.

Finally, since the results for samples A to D were obtained with an optical sampling module of 20GHz, we also considered using a module with larger bandwidth (30 GHz) to improve on the temporal measurements. As anticipated, we measured lower percent differences relative to the phase-shift measurements. Sample B shows a decrease from 18.31% to 2.78% difference between averaged TOF slopes (both input wavelength spacing) and phase-shift slopes. A 0.36% difference in the slopes is obtained for the 1.6nm input spacing measurement alone, the lowest yet measured. Thus, the bandwidth of the optical sampling module and making multiple measurements are key factors in realizing more precise chromatic dispersion measurements based on TOF.

V. DISCUSSION

There exists certain limitations to the TOF technique, and these must be fully understood. First, there is a minimum length of fiber, or DL product, which can be accurately tested. As cited in many sources and articles on TOF measurements,[1,3,9] experiments show that a time delay equal to twice the

FWHM of the input pulse is necessary in order to be able to distinguish the individual delayed pulses. For SMF with a dispersion of 17ps/(nm·km), this corresponds to a minimum test length of 4.04km for a wavelength spacing of 3.2nm. In the case where the multi-wavelength source has a wavelength spacing of 1.6nm, the lower limit increases to 8.09km. This explains why sample A was only measured using the 3.2nm setting; its length was later determined to be around 4.3km. The flexibility of our SFL thus permits not only more precision for DL products greater than 138ps/nm, but also the possibility to increase the wavelength spacing to be able to measure smaller DL products not possible with the 1.6nm spacing mode. Note that the TOF method cannot be used to measure dispersion in fiber components, nor in C-band dispersion shifted fiber (DSF) as the order in which the pulses are delayed cannot be predicted. The method is, however, a fast, simple, low-cost solution for measuring dispersion in long fiber networks.

VII. CONCLUSION

We have successfully demonstrated the measurement of chromatic dispersion in fiber lengths using the TOF method with our newly developed tunable multi-wavelength SFL. Measurements were compared to the phase-shift technique and show good agreement. The limitations and errors encountered can be improved upon in the near future through little minor improvements such as using optical sampling modules with larger bandwidths, shorter optical pulses, increasing the number of measurements before averaging (ten or more), and using computer-controlled data acquisition. Nevertheless, this new measurement system offers the advantage of being much quicker and less cumbersome, as no reference signal or wavelength scanning is needed. As for the multi-wavelength source's induced limitations, it is understood that an improvement on stability, output power, as well as smaller linewidths and flatness would reduce the errors of the TOF results here presented. The idea here, however, was to offer a reliable yet simple and low-cost application. This was indeed achieved as we proposed a rapid and convenient commercially applicable solution.

ACKNOWLEDGMENTS

This work was supported by an NSERC-eMPOWR scholarship and Anrtisu Electronics, Ltd.

REFERENCES

1. J.-N. Maran, Radan Slavik, Sophie LaRochelle, and Miroslav Karasek, "Chromatic Dispersion Measurement Using a Multiwavelength Frequency-Shifted Feedback Fiber Laser", *IEEE Transactions on Instrumentation and Measurement*, vol. 53, no. 1, February 2004.
2. L.G. Cohen, "Comparison of single mode fiber dispersion measurement techniques", *J. Lightwave Technology.*, vol. 5, pp. 958-966, 1985.
3. ITU: International Telecommunications Union, Recommendation G.650.
4. L. R. Chen. "Tunable Multiwavelength Fiber Ring Lasers Using a Programmable High-Birefringence Fiber Loop Mirror", *IEEE Photonics Technology Letters*, Vol. 16, No.2, February 2004.
5. N. Pleros, C. Bintjas, M. Kalyvas, G. Theophilopoulos, K. Yiannopoulos, S. Sygletos, and H. Avramopoulos. "Multiwavelength and Power Equalized SOA Laser Sources" *IEEE Photonics Technology Letters*, vol. 14, no.5, May 2002.
6. D. B. Mortimore, "Fiber Loop Reflectors", *J. Lightwave Technology*, vol. 6, no. 7, July 1988.
7. Y. Shiquan, L. Zhaohui, D. Xiaoyi, Y. Shuzhong, K. Guiyun, and Z. Qida. "Generation of Wavelength-Switched Optical Pulse from a fiber ring laser with F-P Semiconductor Modulator and a HiBi Fiber Loop Mirror" *IEEE Photonics Technology Letters*, vol. 14, no.6, June 2002.
8. K. Morishita, K. Shimamoto. "Wavelength-Selective Fiber Loop Mirrors and Their Wavelength Tunability by Twisting" *J. of Lightwave Technology*, vol. 13, no.11, November 1995.
9. M. J. Heckert, "Development of Chromatic Dispersion Measurement on Multimode Fiber Using Relative Time of Flight Measurement Technique", *IEEE Photonics Technology Letters,* vol. 4, no. 2, February 1992.
10. L. G. Cohen, "Dispersion and Bandwidth Spectra in Single-Mode Fibers", *IEEE J. of Quantum Electronics*, vol. QE-18, no. 1, January 1982.

2) Article to be published in *Electronics Letters*, vol. 41, no. 21, October 2005.

Tunable photonic microwave filter using semiconductor fibre laser

L.R. Chen and V. Pagé

A tunable photonic microwave filter using a simple and tunable multi-wavelength semiconductor fibre laser incorporating a high-birefringence Sagnac loop is demonstrated. The wavelength spacing of the laser can be easily varied using optical switches, which in turn allows the free-spectral-range of the photonic microwave filter to be digitally tuned.

Introduction: In recent years there has been considerable interest in photonic microwave filters since they can exploit the advantages of photonic components—such as low loss, compactness, and immunity to electromagnetic interference—for the processing of RF, microwave, and millimetre-wave signals [1–4]. In particular, the design and implementation of simple, low-cost, and tunable structures has been the subject of intense research [4–8].

Fig. 1 shows one basic implementation of a photonic microwave filter. The output from a multi-wavelength optical source is externally modulated using an electro-optic modulator driven by an RF signal. The modulated optical signal is then transmitted through a wideband dispersive medium, such as singlemode fibre (SMF). The photodetected signal corresponds to the electrical output of the filter.

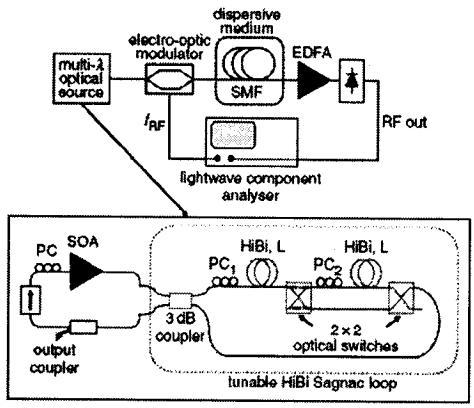

Fig. 1 *Schematic of tunable photonic microwave filter and tunable SFL incorporating HiBi Sagnac loop*

The magnitude of the filter transfer function $|H(f_{RF})|$ is given by

$$|H(f_{RF})| \propto \cos\left(\frac{\pi\lambda_0^2 D f_{RF}^2}{c\ 2}\right)\left|\sum_{m=1}^{N} P_m \exp[-j\pi(m-1)f_{RF}D\Delta\lambda]\right| \quad (1)$$

where N is the number of lasing wavelengths (optical carriers), P_m is the output power of the mth lasing wavelength, $\Delta\lambda$ is the wavelength spacing between carriers, λ_0 is the central wavelength, and D is the dispersion [ps/nm] of the dispersive medium. The free-spectral-range (FSR) of the filter is given by

$$\mathrm{FSR} = \frac{1}{D\Delta\lambda} \quad (2)$$

which can be tuned by varying the product $D\Delta\lambda$. For a fixed length of fibre (i.e. fixed D), tuning the filter FSR requires the wavelength spacing of the multi-wavelength source to be varied. Existing techniques involve the use of arrays of tunable laser diodes [4] or programmable spectrally-sliced broadband optical sources [4, 8], which are expensive or may involve complex implementations. In this Letter, we demonstrate tuning the FSR of a photonic microwave filter using a multi-wavelength semiconductor fibre ring laser (SFL) with tunable wavelength spacing.

Results: The tunable SFL is shown in Fig. 1 and is similar to that reported in [9]. The use of a semiconductor optical amplifier (SOA) as the gain medium ensures stable, room-temperature operation at multiple wavelengths and for operation over a wide bandwidth. The lasing wavelengths are defined using a high-birefringence (HiBi) Sagnac loop operated in transmission (note that the reflection response of the loop can also be used in conjunction with an optical circulator).

The transmission response of the HiBi Sagnac loop has a comb-like profile and is approximately a periodic function of wavelength with the peaks separated by $\Delta\lambda = \lambda^2/\Delta nL$, where L and Δn are the length and birefringence, respectively, of the HiBi fibre. The transmissivity is independent of the polarisation state of the input beam; adjusting the polarisation controllers (PCs) in the loop affects the contrast or isolation of the transmission bands, but not $\Delta\lambda$. On the other hand, changing the length L of HiBi fibre will vary $\Delta\lambda$. This can be accomplished by cascading segments of HiBi fibre interconnected by 2×2 switches [9].

In our SFL implementation, we use two segments of HiBi fibre, thereby allowing us to choose between two possible wavelength spacings. The HiBi fibre has a measured birefringence of 3.8×10^{-4} at 1550 nm and the segments are equal in length with $L \simeq 1.99$ m. If the first 2×2 switch is in the cross state, then $\Delta \simeq 3.2$ nm; if the switch is in the bar state, the length of HiBi fibre in the loop doubles and the wavelength spacing is halved ($\Delta\lambda \simeq 1.6$ nm). Other than the HiBi fibre, all other components in the loop are SMF. The insertion loss of the loop is $\simeq 4$ dB for $\Delta\lambda = 3.2$ nm and is approximately 3.5 dB higher for $\Delta\lambda = 1.6$ nm owing to the additional splicing losses between the HiBi fibre and SMF.

Fig. 2 shows the transfer function of the photonic microwave filter using 9.5 and 33 km of SMF, respectively, for SFL wavelength spacings of 3.2 and 1.6 nm. Fig. 3 shows typical corresponding output spectra of the laser. Clearly, when the wavelength spacing of the SFL is doubled, the filter FSR is approximately halved, as expected from (2). The simulated and measured filter responses are in very good agreement and, in particular, the measured FSRs correspond to those calculated using (2). Since pure amplitude modulation is used, the carrier suppression effect [i.e. the first term of (1)] creates an overall lowpass response (which is included in the simulations); however, this effect can be overcome easily by using single sideband modulation.

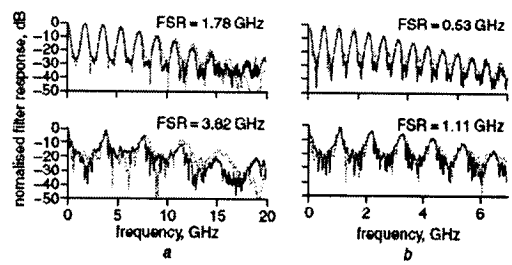

Fig. 2 *Microwave filter response using 9.5 km SMF and 33 km SMF for $\Delta\lambda = 3.2$ nm (top curves) and $\Delta\lambda = 1.6$ nm (bottom curves) measured responses (solid lines) and FSRs; simulated responses (dashed lines)*

a 9.5 km SMF
b 33 km SMF

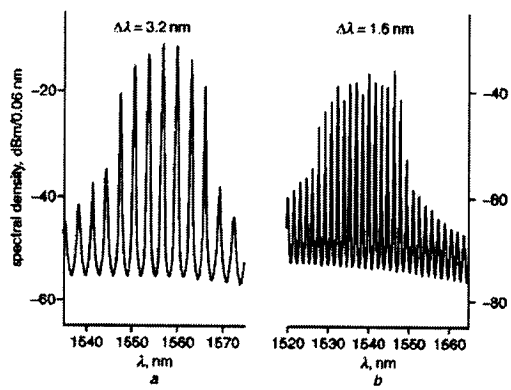

Fig. 3 *Typical output spectra of SFL for $\Delta\lambda = 3.2$ nm and $\Delta\lambda = 1.6$ nm*

a $\Delta\lambda = 3.2$ nm
b $\Delta\lambda = 1.6$ nm

We emphasise that only the state of the switches is set to vary the wavelength spacing of the SFL and hence the filter response; no other components are adjusted. Thus, the tunable SFL allows for a very simple setup and mechanism for tuning the filter FSR. Note that the lasing band for $\Delta\lambda = 1.6$ nm is shifted towards shorter wavelengths owing to the increased cavity loss (for both wavelength spacings, the lasing bands span $\simeq 25$ nm). Nevertheless, this has no impact on the operation nor performance of the microwave filter.

Discussion: The shape of the filter transfer function is set by the values of P_m. For $\Delta\lambda = 3.2$ nm, the envelope of the output power for the main lasing wavelengths has a smooth shape which helps to apodise the filter response. For $\Delta\lambda = 1.6$ nm, the envelope is slightly more irregular, causing some non-uniformity in the filter response. The output power of the lasing wavelengths can be controlled to some extent by optimising the PCs for the different switch states (i.e. wavelength spacings). This then allows for better control over the shape of the filter transfer function. It is also possible to interconnect additional segments of HiBi fibre using more switches, thereby allowing for an even greater number of SFL wavelength spacings, and hence values of the filter FSR. Finally, we can combine our SFL with a dispersion matrix [7] to provide even further flexibility for tuning the filter FSR.

Conclusion: We have demonstrated tuning the FSR of a photonic microwave filter using a tunable multi-wavelength SFL incorporating a HiBi Sagnac loop. The approach is simple to implement and low cost, especially when compared to the use of arrays of tunable laser diodes.

Acknowledgments: This research was supported by an NSERC-eMPOWR scholarship and Anritsu Electronics Ltd.

14 August 2005
Electronics Letters online no: 20052952
doi: 10.1049/el:20052952

L.R. Chen and V. Pagé (*Photonic Systems Group, Department of Electrical and Computer Engineering, McGill University, Montreal, QC, Canada H3A 2A7*)

E-mail: chen@photonics.ece.mcgill.ca

References

1 Hunter, D.B., and Minasian, R.A.: 'Microwave optical filters using in-fibre Bragg grating arrays', *IEEE Microw. Guid. Wave Lett.*, 1996, 6, pp. 103–105
2 Marti, J., Ramos, F., and Laming, R.I.: 'Photonic microwave filter employing multimode optical sources and wideband chirped gratings', *Electron. Lett.*, 1998, 34, pp. 1760–1761
3 Gwandu, B.A.L., Zhang, W., Williams, J.A.R., Zhang, L., and Bennion, I.: 'Microwave photonic filtering using Gaussian-profiled superstructured fibre Bragg grating and dispersive fibre', *Electron. Lett.*, 2002, 38, pp. 1328–1330
4 Capmany, J., Ortega, B., Pastor, D., and Sales, S.: 'Discrete-time optical processing if microwave signals', *IEEE/OSA J. Lightwave Technol.*, 2005, 23, pp. 702–723
5 Marti, J., Polo, V., Ramos, F., and Moodie, D.: 'Photonic tunable microwave filters employing electroabsorption modulators and wideband chirped fibre gratings', *Electron. Lett.*, 1999, 35, pp. 305–306
6 Polo, V., Vidal, B., Corral, J.L., and Marti, J.: 'Novel tunable photonic microwave filter based on laser arrays and $N \times N$ AWG-based delay lines', *IEEE Photonics. Technol. Lett.*, 2003, 15, pp. 584–586
7 Vidal, B., Polo, V., Corral, J.L., and Marti, J.: 'Photonic microwave filter with tuning and reconfiguration capabilities using optical switches and dispersive media', *Electron. Lett.*, 2003, 39, pp. 547–549
8 Capmany, J., Mora, J., Ortega, B., and Pastor, D.: 'Microwave photonic filters using lowcost sources featuring tunability, reconfigurability, and negative coefficients', *Opt. Express*, 2005, 13, pp. 1412–1417
9 Chen, L.R.: 'Tunable multiwavelength fibre ring lasers using a programmable high-birefringence fibre loop mirror', *IEEE Photonics. Technol. Lett.*, 2004, 16, pp. 410–412

Appendix D: Laboratory Pictures

The author next to her experimental setup in the fiber communications laboratory:

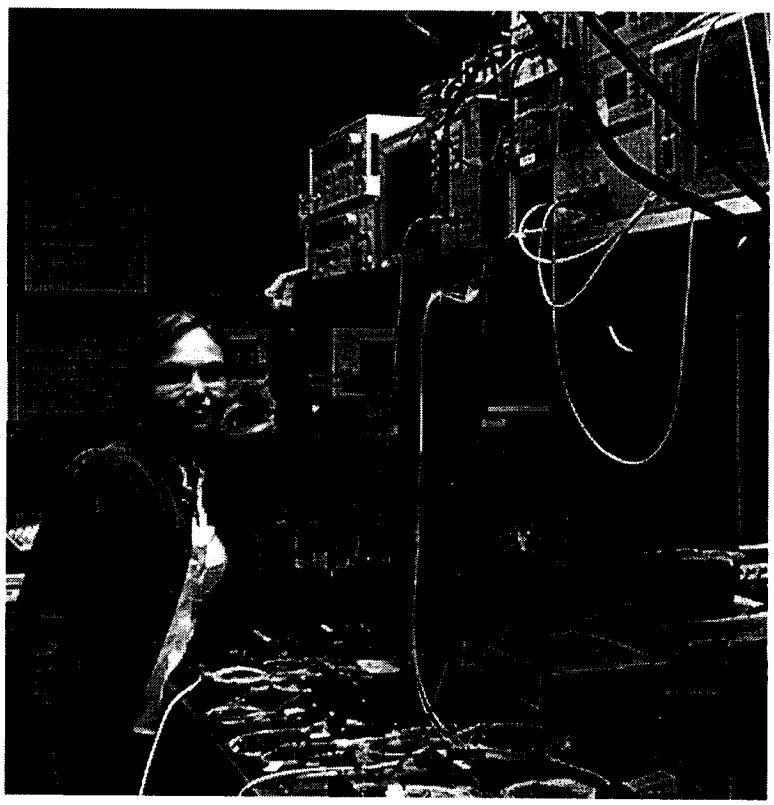

Picture of the setup with the sampling oscilloscope: